MECHANICAL PROPERTIES OF NEAR-FRICTIONLESS HYDROGENATED

AMORPHOUS CARBON FREESTANDING THIN FILMS

FOR MEMS DEVICES

Except where reference is made to the work of others, the work described in this thesis is my own or was done in collaboration with my advisory committee. This thesis does not include proprietary or classified information.

Bo Zhou

Certificate of Approval:

Jeffrey Fergus
Associate Professor
Materials Engineering

Barton C. Prorok, Chair
Assistant Professor
Materials Engineering

Zhongyang Cheng
Assistant Professor
Materials Engineering

Stephen L. McFarland
Acting Dean
Graduate School

MECHANICAL PROPERTIES OF NEAR-FRICTIONLESS HYDROGENATED AMORPHOUS CARBON FREESTANDING THIN FILMS FOR MEMS DEVICES

Bo Zhou

A Thesis

Submitted to

the Graduate Faculty of

Auburn University

in Partial Fulfillment of the

Requirements for the

Degree of

Master of Science

Auburn, Alabama

December 16, 2005

MECHANICAL PROPERTIES OF NEAR-FRICTIONLESS HYDROGENATED

AMORPHOUS CARBON FREESTANDING THIN FILMS

FOR MEMS DEVICES

Bo Zhou

Permission is granted to Auburn University to make copies of this thesis at its discretion, upon request of individual or institutions and at their expense. The author reserves all publication rights.

____

Signature of Author

____

Date of Graduation

THESIS ABSTRACT

MECHANICAL PROPERTIES OF NEAR-FRICTIONLESS HYDROGENATED AMORPHOUS CARBON FREESTANDING THIN FILMS FOR MEMS DEVICES

Bo Zhou

Master of Science, December 16, 2005
(B.S., Fudan University, 2002)

135 Typed Pages
Directed by Dr. Barton C. Prorok

Diamond-Like carbon (DLC) films with a mixture of sp^2 and sp^3 hybridizations have exhibited excellent properties such as chemical stability, wear resistance, optical transparency and are now widely used as protective overcoatings in various fields. In this paper, the membrane deflection experiment (MDE) was used for measuring the Young's modulus, fracture strength, and residual stress of the so-called Near-frictionless carbon (NFC) films developed at Argonne National Laboratory. In this method, free standing NFC membranes were fabricated and stretched by a nanoindenter while deflection was monitored with an interferometer. By combining these two independent measurements, the mechanical properties of NFC films were characterized. The specific a-C:H films were grown at Argonne National Lab and are those films that exhibited excellent

tribological properties with super low friction coefficients of 0.002. The Young's modulus of NFC films measured from 45 membranes ranged from 32 GPa to 38 GPa. The average (arithmetic mean) value was 35.13 GPa. The standard deviation was 2.292 GPa. The fracture strength varied from 0.12 GPa to 0.90 GPa and the residual stress ranged from 79 MPa to 310 MPa. Width and thickness effects of the membranes were also studied in this work. It was found the fracture strength increased with decreasing membrane width and thickness. The residual stress increased with decreasing membrane thickness.

ACKNOWLEGMENTS

I would like to thank Dr. Bart Prorok for all his support and suggestions during this thesis work. I would like to thank Liwei Wang, Shakib Morshed, and Nikhil Mehta for their help during fabrication and MDE procedures. I also want to thank Dr. Erdemir and Dr. Eryilmaze from Argonne for their assistance with NFC film deposition.

Style manual or journal used Guide to Preparation and Submission of Theses and Dissertations

Computer software used Microsoft Word 2003

TABLE OF CONTENTS

LIST OF FIGURES xi

LIST OF TABLES xv

CHAPTER 1 INTRODUCTION 1

1.1 Synopsis 1

1.2 Overview 2

1.3 Thesis structure 4

CHAPTER 2 LITERATURE REVIEW 10

2.1 Diamond like carbon 10

2.1.1 Diamond like carbon materials . . . 10

2.1.2 Deposition methods of DLC 11

2.1.3 Deposition mechanisms 13

2.1.4 Hydrogenated amorphous carbon . . . 16

2.2 MEMS devices 20

2.2.1 Overview 20

2.2.2 Microfabrication process of MEMS devices . . 20

2.2.3 DLC role in MEMS devices . . . 22

2.2.4 MEMS fabrication problems . . . 23

2.3 Thin films 24

2.4 Nanoindentation 25

2.5 Membrane deflection experiment 27

2.6 DLC Raman Spectra 29

CHAPTER 3 EXPERIMENTAL SETUP 57

3.1 Specimen design 57

3.2 Wafer/Substrate preparation 57

3.3 NFC deposition 58

3.4 Micromachining process 59

3.4.1 Wafer cleaning 59

3.4.2 Bottom side PR patterning 60

3.4.3 Bottom side Si_3N_4 etching 60

3.4.4 Top side PR patterning 61

3.4.5 Cr sputtering 61

3.4.6 Lift-off 61

3.4.7 O_2 RIE etching 62

3.4.8 KOH etching 63

3.4.9 Cr etching 64

3.4.10 Top side Si_3N_4 etching 64

3.5 MDE setup 64

CHAPTER 4 RESULTS AND DICUSSIONS 79

4.1 Key issues in micromachining NFC films . . . 79

4.1.1 Robust mask for NFC etching . . . 79

4.1.2 O_2 RIE etching of NFC films . . . 79

4.1.3 KOH bulk micromachining of Si substrate . . 80

4.1.4 Top side Si_3N_4 etching 81

4.2 Profilometer and Raman characterization . . . 82

4.3 AFM characterization 82

4.4 SEM characterization and MDE results . . . 83

4.5 Data reduction 84

4.6 Young's modulus of the NFC6 film 85

4.7 Width effect on fracture strength 86

4.8 Thickness effect on fracture strength and residual stress . 87

CHAPTER 5 OVERALL CONCLUSIONS 114

BIBLIOGRAPHY 118

LIST OF FIGURES

Fig. 1.1 3D Schematic view of MDE tests [8] 6

Fig. 1.2 Ternary phase diagram of bonding in amorphous carbon-hydrogen alloys [11] 7

Fig. 1.3 SEM image of NFC freestanding membranes, 460nm NFC6, group E 8

Fig. 1.4 NFC6 freestanding membrane fabrication flow . . . 9

Fig. 2.1 sp^3 hybridization and diamond FCC structure . . . 32

Fig. 2.2 sp^2 hybridization and graphite sheet structure . . . 33

Fig. 2.3 Various deposition systems for DLC [11] . . . 34

Fig. 2.4 Magnetron sputtering system 35

Fig. 2.5 Schematic of RF PECVD and plasma sheath . . . 36

Fig. 2.6 Subplantation model for DLC deposition mechanisms [11] . . 37

Fig. 2.7 Deposition mechanisms for a-C:H [11] 38

Fig. 2.8 H erosion effect during a-C:H deposition [34] . . . 39

Fig. 2.9 The role of the bias in a-C:H deposition [36, 3] . . . 40

Fig. 2.10 Temperature effect on a-C:H deposition and H etching rate [34] . 41

Fig. 2.11 Different types of MEMS devices 42

Fig. 2.12 <100> and <110> KOH etching [40] 43

Fig. 2.13 Surface micromachining [42] 44

Fig. 2.14 Interfacial residual stress for cantilevers [39]. . . . 45

Fig. 2.15 Illustration of length-scale effects on the mechanical properties of materials [8] 46
Fig. 2.16 Schematic of the basic components of a nanoindenter [46] . . 47
Fig. 2.17 Schematic of nanoindentation [46] 48
Fig. 2.18 Pile up and sink in [8] 49
Fig. 2.19 Nanoindenter and interferometer for MDE tests . . . 50
Fig. 2.20 Interferometer images of the bottom side of the membranes . . 51
Fig. 2.21 Misalignment between tip and membrane [7] . . . 52
Fig. 2.22 Schematic of MDE [50, 7] 53
Fig. 2.23 Raman spectra of DLC materials [11] 54
Fig. 2.24 sp^3 ratio vs. G peak position and I_D/I_G [55] 55
Fig. 3.1 Die schematic for NFC freestanding membranes . . . 66
Fig 3.2 Schematic of the RF PECVD system at Argonne National Lab . 67
Fig. 3.3 NFC membrane fabrication process flow 68
Fig. 3.4 Image of the bottom window mask 71
Fig. 3.5 Image of the top membrane mask 72
Fig. 3.6 Image of the sputtering system 73
Fig. 3.7 Subtractive and lift-off processes [40] 74
Fig. 3.8 Image of the AOE system 75
Fig. 3.9 Image of the KOH system 76
Fig. 4.1 NFC membrane feature after Cu or Cr was etched . . . 88
Fig. 4.2 Wafer surface after Cr etching 89

Fig. 4.3 SEM image and the schematic of the notching underneath the NFC film 90
Fig. 4.4 Schematic of final window size after KOH etching . . . 91
Fig. 4.5 Backside views of two dies after KOH etching with different parameters 92
Fig. 4.6 Images of the NFC film bottom surface after H_3PO_4 etching . 93
Fig. 4.7 Images of the NFC film bottom surface after plasma etching . 94
Fig. 4.8 Raman spectra of NFC films 95
Fig. 4.9 AFM images of 150nm NFC surface 96
Fig. 4.10 AFM images of 460nm NFC surface 97
Fig. 4.11 AFM images of 900nm NFC surface 98
Fig. 4.12 SEM image of the group G membranes from the 460nm NFC film . 99
Fig. 4.13 NFC membrane bending down/up situation. 100
Fig. 4.14 Original fringes and profile of the group J membrane (900nm NFC) 101
Fig. 4.15 Raw and real L-d plots of the group J membrane . . . 102
Fig. 4.16 Stress-strain curves of 150nm NFC 103
Fig. 4.17 Stress-strain curves of 460nm NFC 104
Fig. 4.18 Stress-strain curves of 900nm NFC 106
Fig. 4.19 Nanoindentation Load-Displacement plot 108
Fig. 4.20 CSM tests results run on the 150nm NFC 109
Fig. 4.21 NFC film pile-up after nanoindentation tests 110
Fig. 4.22 Width effect on fracture strength (900nm NFC) . . . 111

Fig. 4.23 Thickness effect on fracture strength (group E) . . . 112

Fig. 4.24 Thickness effect on residual stress (group E) . . . 113

LIST OF TABLES

Table 2.1 Comparison of major properties of amorphous carbons with those of reference materials diamond, graphite, C_{60} and polyethylene. [11] 56

Table 2.2 Different indenter tips [46] 56

Table 3.1 Membrane specimens 77

Table 3.2 Argonne NFC labels 78

Table 3.3 Sputtering Parameters 78

CHAPTER 1

INTRODUCTION

1.1 Synopsis

Diamond-like carbon with a mixture of sp^2 and sp^3 hybridizations has excellent properties like diamond, such as high hardness and Young's modulus, chemical stability, wear resistance, and optical transparency. DLC thin films are now widely used as protective overcoatings in various fields like magnetic storage disks, biosensing, car parts sensors and Micro-Electro-Mechanical Devices (MEMS). The DLC thin film mechanical properties are the key parameters to develop those cutting edge technologies. However, our knowledge in this area is limited by inaccurate testing methods. The mechanical properties of DLC thin films are often measured by a nanoindentor [1-4]. The "substrate effect" largely affects the mechanical properties of DLC films. Although limiting the indentation depth to the order of 10% of the film thickness will increase the accuracy [2], reported values of Young's modulus of DLC films vary from author to author [3-6].

In this work, a methodology (developed by Prorok and Espinosa [7]) to precisely measure the mechanical properties of freestanding thin films was applied on Near-Frictionless Hydrogenated Amorphous Carbon (NFC) films developed at Argonne National Lab. In this method, free standing NFC membranes were fabricated and stretched by a nanoindenter while deflection was monitored with an

interferometer (Figure 1.1 [8]). By combining these two independent measurements, the NFC thin film mechanical properties, such as Young's modulus, fracture strength, and residual stress were characterized. The membrane size and thickness effects on thin film mechanical properties were also discussed in this thesis.

1.2 Overview

The thesis work started with the idea of accurately measuring the mechanical properties of DLC thin film for our MEMS devices. This project was cooperated with Argonne National Laboratory. The first part needed to decide was what kind of DLC we should choose for our experiments and devices. It is well known that the DLC family has not only amorphous (a-C) carbon but also hydrogenated alloys (a-C:H). A ternary phase diagram shown in figure 1.2 displays the compositions of the various forms of amorphous C-H alloy first used by Jacob and Moller [9]. The hydrogenated amorphous carbon is generally deposited using various source gases (methane, ethane, ethylene, acetylene) as well as hydrogen gas by RF PECVD. Films grown in source gases with higher hydrogen-to-carbon ratios has much lower friction coefficients and wear rate than films derived from source gases with lower hydrogen to carbon ratios [10]. As a protective coating for MEMS devices, hydrogenated amorphous carbon with high mechanical strength and exceptional tribological properties is no doubt a good choice. Among those near-frictionless hydrogenated DLC grown by Argonne lab, a film (named as NFC6) derived from 25% CH_4+75% H_2 gives the lowest friction coefficient. This was the reason why we selected NFC6 as our sample DLC films.

The second part of the project was the specimen design. The specimen geometry was a double dog bone freestanding membrane fixed at both ends (Figure 1.3). The structure was developed by Prorok and Espinosa for their gold membrane deflection experiments (MDE) [7]. In order to get freestanding membranes, NFC6 film was deposited on a 4 inch silicon wafer with double side silicon nitride. The bottom and top Si_3N_4 worked as a mask layer and an etching stop layer for KOH Si-etching, respectively. After bulk machining and wet/dry etching of silicon nitride, the NFC membranes were released and overhanged the window.

The third part was electronic fabrication of the sample wafers. <100> direction silicon wafers with double side polishing were used as substrates. Silicon nitride layers were grown on both sides of the wafer using LPCVD method. The NFC6 films were then deposited on one side of the wafer at Argonne National Lab. A Perkin Elmer 2400 PECVD system was used for the experiments. 6~9 hours deposition time was needed based on different thickness requirement. The NFC films followed the bulk micromachining procedure to obtain the freestanding structure. The bottom side Si_3N_4 was first patterned and etched to obtain open windows. The top side was then patterned and chromium was sputtered on the surface as a mask layer for DLC etching. A lift-off process was involved to give the shape of the membranes followed by DLC plasma etching. After silicon and top Si_3N_4 etching, the freestanding structure was obtained. A fabrication flow is shown in figure 1.4.

The fourth part was to characterize the samples before MDE tests. Raman spectroscopy, profilometer, scanning electron microscopy (SEM) and atomic force

microscopy (AFM) were used to obtain the basic information of NFC bonding structure, sp^2/sp^3 ration, profile and topography. Due to the different coefficient of thermal expansion (CTE) between Si_3N_4 and NFC, the NFC membranes would bend down in some content during the topside Si_3N_4 etching. It was necessary to characterize each membrane's shape with SEM before MDE tests. Missing that would cause the final data inaccurate. Detailed explanations will be discussed in the Results and Discussion section.

The MDE tests were the main part of the experiments. It worked by stretching a freestanding fixed-fixed membrane at its center with a nanoindenter wedge tip. Simultaneously, deflection was recorded by the nanoindenter displacement sensor and by an interferometer focused on the bottom side of membrane through-view window in the wafer (Figure 1.1). A data reduction process was needed for MDE tests due to the bending of the membrane mentioned above. After that, NFC mechanical properties such as Young's modulus, residual stress and fracture strength were determined. Moreover, by comparing the mechanical properties of the membranes with different widths and thicknesses, the size and thickness effects on the mechanical properties could be determined.

1.3 Thesis Structure

Chapter 2 gives literature review to all subjects that are related to this thesis work. It includes DLC materials, MEMS devices, thin films, microelectronic fabrication, nanoindentation, and MDE tests. In the DLC part, an overview of DLC structure,

bonding, properties and variations will be briefly introduced. Deposition techniques and deposition mechanisms are discussed based on the well known “subplantation” model [11]. Hydrogenated amorphous carbon (a-C:H) is introduced separately for this project. The roles of deposition parameters like the substrate bias voltage and temperature are discussed. An introduction of MEMS is given, which focuses on materials selection and fabrication issues. The application of DLC materials in MEMS devices is briefly introduced. Thin film properties are discussed with bulk properties of the same material and the difference is illustrated. Important hints and notifications are expressed in the fabrication part. Nanoindention and MDE theories are briefly introduced and explained in details in later chapters.

Chapter 3 introduces the whole fabrication procedure of the NFC freestanding membrane. It includes: Wafer/substrate preparation, NFC deposition, and micromachining processes.

Chapter 4 deals with the final results and discussion. Specimen design and fabrication results are illustrated first. Raman spectroscopy data helps determine the sp2/sp3 ratio of the film. The profilometer is used to measure the thickness of the NFC6 films. AFM shows the topography of the DLC membranes. SEM would help profile the membranes for MDE data reduction. The raw MDE data was collected and treated with reduction. The deviation caused by air effect and membrane bending are corrected to obtain the mechanical properties of NFC films. The membrane size and thickness effects are also discussed in this section.

Chapter 5 provides conclusions and future work.

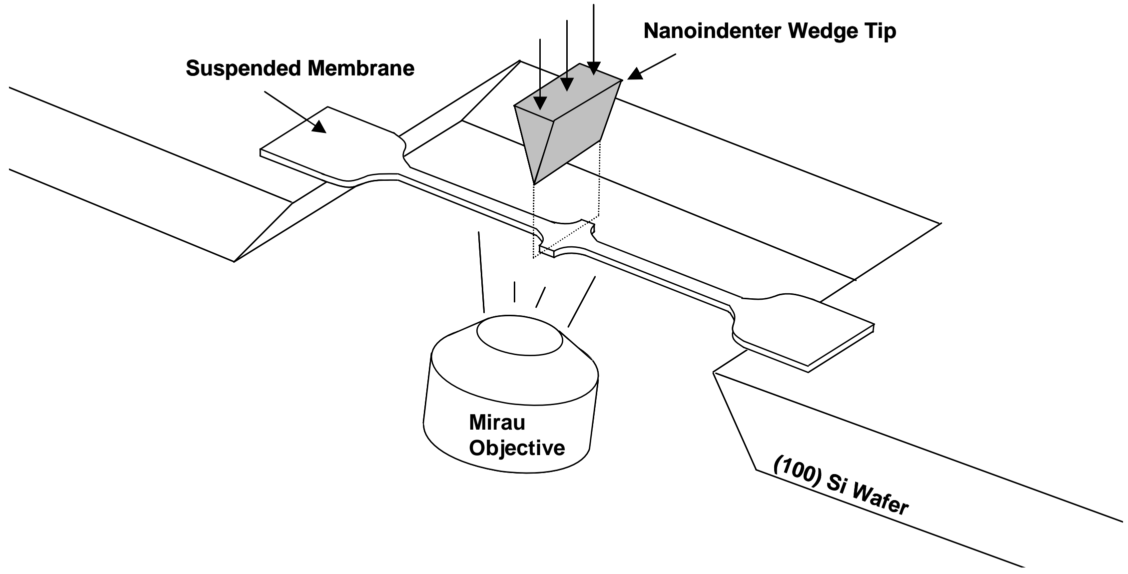

Figure 1.1 3D Schematic view of MDE tests [8]

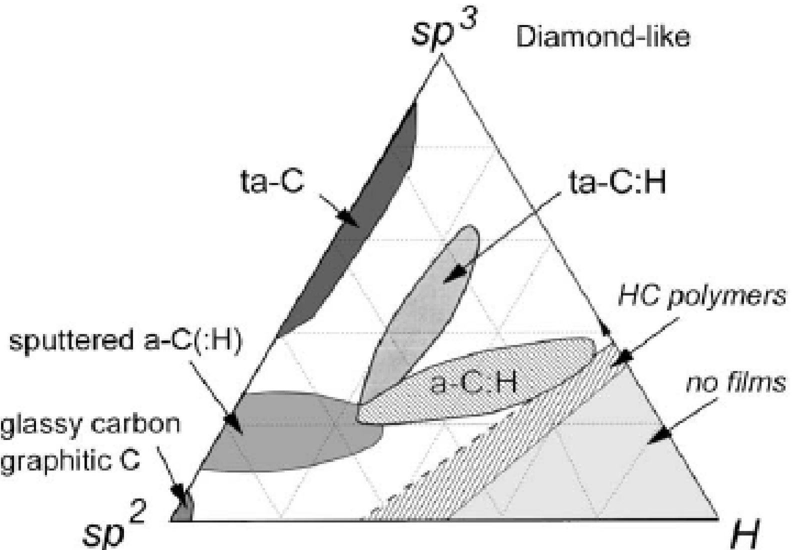

Figure 1.2 Ternary phase diagram of bonding in amorphous carbon-hydrogen alloys.

[11]

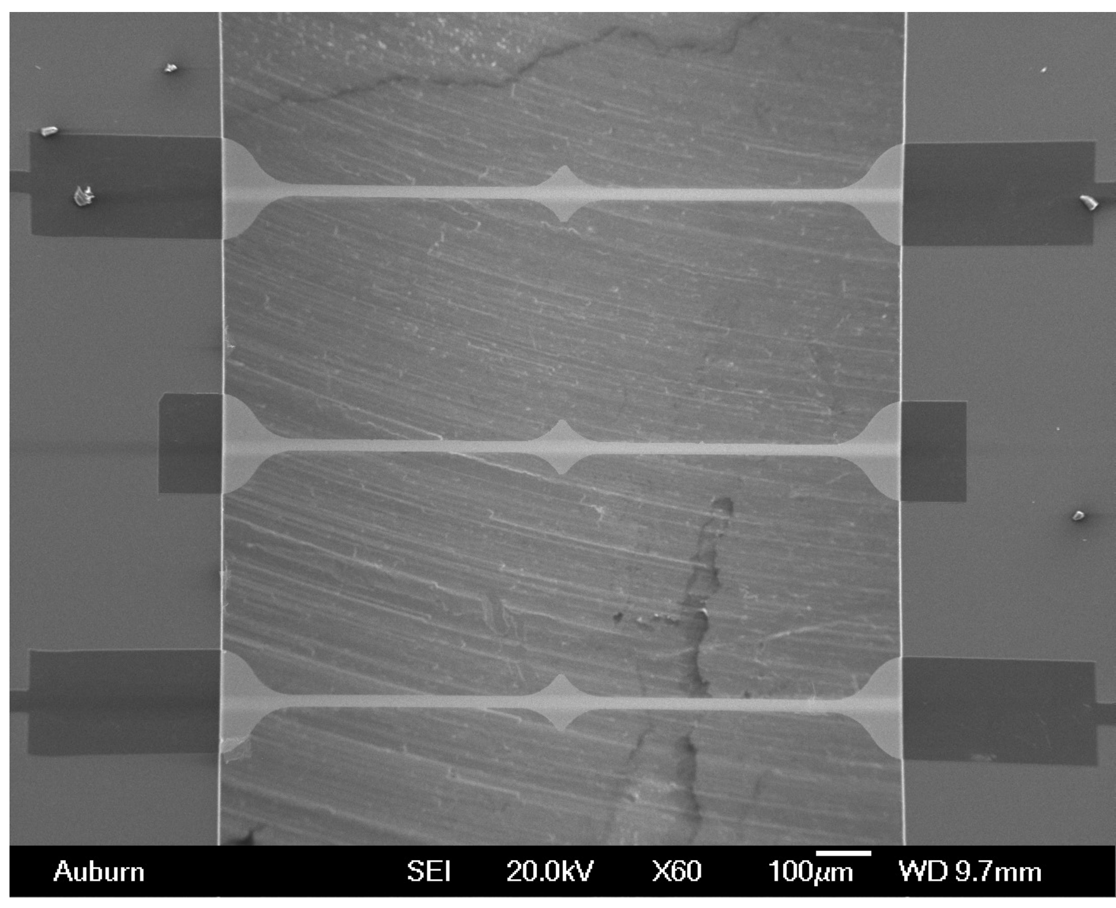

Figure 1.3 SEM image of NFC freestanding membranes

(460nm NFC6, group E)

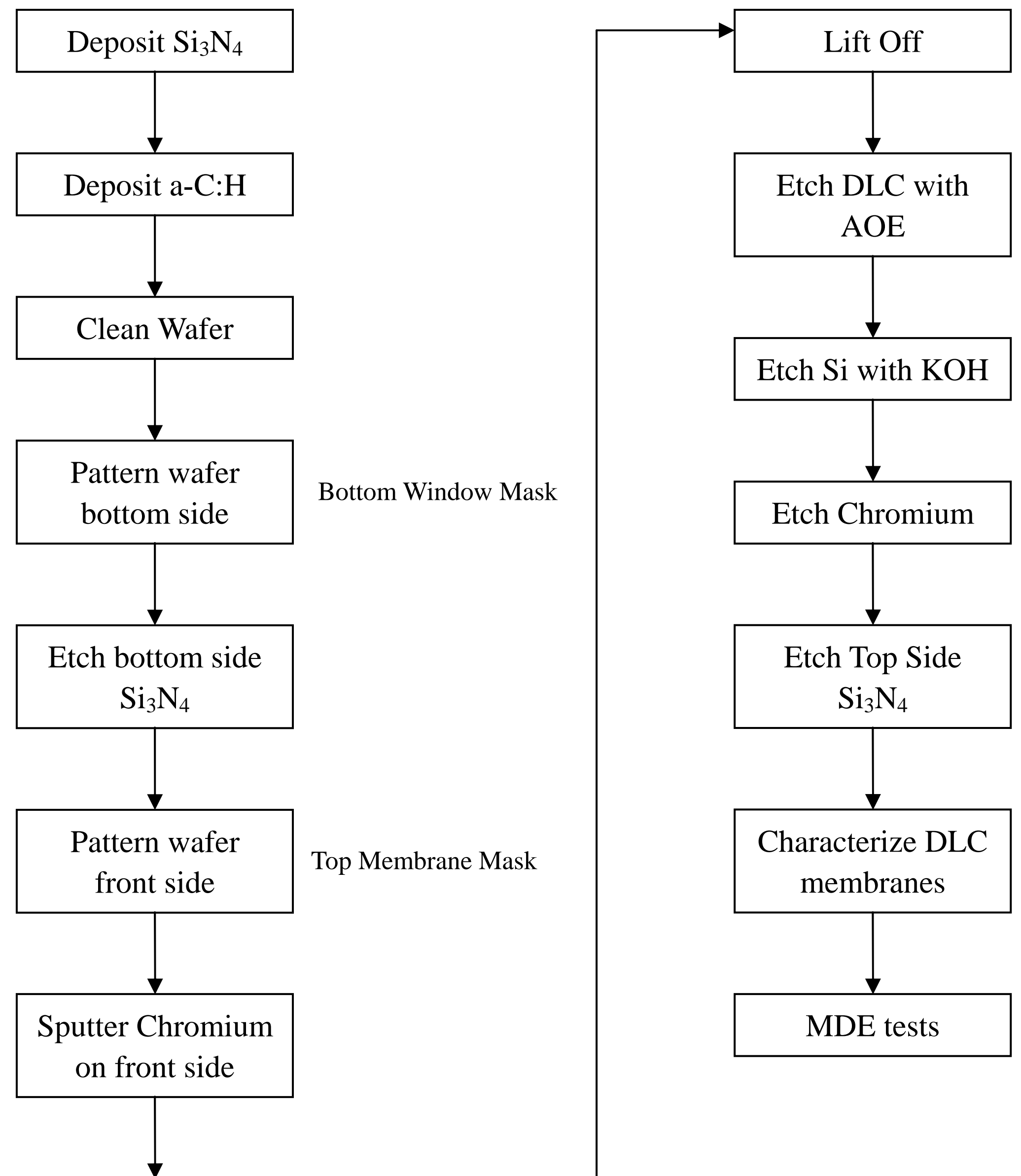

Figure 1.4 NFC6 freestanding membrane fabrication flow

CHAPTER 2

LITERATURE REVIEW

2.1 Diamond like carbon

2.1.1 Diamond like carbon materials

Diamond-like carbon is a metastable form of amorphous carbon containing both sp^2 and sp^3 bonds. The excellent mechanical properties similar to diamond and relative inexpensive price of DLC thin films are the main motivations for DLC applications. As mentioned above, DLC has a variety of structures due to the existence of three hybridizations, sp^3, sp^2 and sp^1. It is helpful to review these three hybridizations for understanding DLC bonding structures.

Carbon is an element in the first row of periodic table. The energies of s-orbital and p-orbitals of carbon's second electronic shell are so close that hybridized atomic orbitals can be formed. In diamond, sp^3 bondings are dominant. One s-orbital and three p-orbitals hybridize to form a tetrahedrally directed sp3 orbital. Four valence electrons of carbon atoms are each assigned to a sp^3 orbital, which makes a strong covalent σ bond to an adjacent atom [11]. Figure 2.1a and 2.1b shows the sp^3 hybridization and a typical diamond crystal structure, respectively. In graphite, sp^2 bondings dominate. One s-orbital hybridizes with 2p-X and 2p-Y obitals, which makes a three-fold sp^2 configuration in X-Y plane. Three of four valence electrons are in this trigonal sp^2 hybridization, which form σ bonds in-plane (figure 2.2a). One of

the p-orbitals (p-Z) is left unaffected. This last p-orbital overlaps with those from neighboring carbon atoms, in a sideways manner, to form a weaker π bond. This is the reason why ultrathin graphite sheet has excellent mechanical properties (figure 2.2b). In the sp^1 hybridization, one s-orbital hybridize with one p-orbital to form σ bonds in one direction (for example ±X). The other two electrons form π bonds with adjacent atoms in another two directions (Y and Z). The excellent mechanical properties of diamond, graphite sheet and DLC come from the strong, directional σ bonds [12].

Various forms of DLC and their main properties are listed in table 2.1. As mentioned earlier, DLC has not only amorphous carbon (a-C) but also hydrogenated amorphous carbon (a-C:H). Usually, both a-C and a-C:H represent a DLC with high sp^2 ratio and low sp^3 ratio. However, using high plasma density sputtering and PECVD deposition systems can make the sp^3 fraction to a high degree. In order to distinguish them from sp2 DLC, Tetrahedral amorphous carbon (ta-C) is suggested by McKenzie [13] for high sp^3 amorphous carbon and ta-C:H is referred to sp^3 hydrogenated tetrahedral amorphous carbon by Weiler [14]. Figure 1.2 shows the position of those DLC materials in Jacob and Moller's ternary phase diagram.

2.1.2 Deposition methods of DLC

DLC can be deposited through various systems [11, 15]. It includes: Ion beam, mass selected ion beam (MSIB), sputtering, cathodic arc, pulsed laser deposition (PLD), and plasma enhanced chemical vapor deposition (PECVD). Figure 2.3 shows the schematics of various deposition systems for DLC [11]. Among those methods, sputtering and PECVD are most frequently used for industrial process and laboratory

studies, respectively [16-19]. Sputtering is a physical process (except reactive sputtering), where ion bombardment is the key mechanism for inducing sp3 bonding of DLC. Either DC or RF power could be used to generate argon plasma sputtering the graphite electrode. Magnetic fields are often applied in the sputtering chamber to increase the deposition rate. Figure 2.4 shows a magnetron sputtering system with four magnets along the chamber wall. The magnetic fields make the electrons spiral and increase their mean free path. In other words, it increases the ionization degree of the plasma. A bias voltage is often applied to the substrate to increase the ion bombardment. Sputtering has several advantages, such as versatility of sputtering methods and deposition conditions can be easily controlled by the plasma power and gas pressure. However, the low ratio of energetic ions to neutral species limits the hardness of DLC films [11].

Compared to sputtering, PECVD involves not only the physical process of bombardment but also the chemical reactions on and inside the films. RF PECVD is often used to deposit DLC. Figure 2.5 shows the schematic for RF PECVD. The shorter electrode is connected with RF power, while the longer one is earthed. As the source gases are induced into the main chamber, the plasma is created between electrodes by the RF power. One important feature, the "plasma sheath" [20] is formed near the electrode surface due to the different mobility between ions and electrons. Since electrons have much higher thermal velocities than ions, they are lost faster at the electrodes and leave the plasma slightly positive charged. Thus an electric field is generated pointed from plasma to the solid surface and accelerates the ions in

the plasma to the wall. This confines the ions near the surface and creates a sheath with a net positive charge. The sheath has an order of Debye length in thickness and usually is darker due to the low electron density in that region. In low pressure, the ion sheaths formed are collisionless and have low conductivity thus serving as diodes between plasma and electrodes. The electrodes then obtain DC self-bias voltages equal to their peak RF voltage [11]. Thus, the inverse capacitances of these two diodes determine the DC bias direction. The shorter electrode has a smaller capacitance, which brings a larger (negative) bias voltage. Thus the DC bias is point from the larger electrode to the shorter one. The field accelerates the positive ions to the shorter electrode. This is the reason that substrate is mounted to the shorter electrode. PECVD always use a low gas pressure.

2.1.3 Deposition mechanisms

Many researches have been dedicated to the DLC deposition mechanisms. There is one thing in common that the sp^3 bonding is dominated by the ion bombardment process. In 1970s, Spencer and co-workers proposed one theory that the carbon ions had preferential sputtering on sp^2 sites, which turned sp^2 to sp^3 bonding from the sp^2/sp^3 mixture [21]. However, Lifshitz et al. noticed that atom's cohesive energy was the main factor that affected the sputtering yield, so that the yield has little difference between sp^2 and sp^3 sites [22]. They supposed that the sp^3 growth was on sub-surface from the incidence of higher ion energies and higher ion masses [22]. Based on their theories, a low energy subsurface implantation model "subplantation" was built. "subplantation" model was improved later by Moller [23], McKenzie [24], and

Robertson [25-27]. With the proof from numerical and analytical simulations [28, 29], "subplantation" become the basic platform for understanding DLC deposition mechanism.

Figure 2.6a shows the schematic of subplantation suggested by Robertson [11]. The first thing need to be concerned with this process is the relationship between atomic scale and energy of carbon ions. As the ion energy goes higher, the carbon atomic radius decrease [30-31], which makes it possible for a carbon ion to enter an interstice and penetrate the surface layer. The smallest ion energy for penetration is called E_P. As the ion reaches the surface, it has to overcome the surface attractive potential barrier E_B. Moreover, the ion should knock out an atom on the surface to create a vacancy-interstitial pair. The minimum displacement energy is E_B. Thus, we obtain the relationship between these three energies as:

$$E_P \approx E_d + |E_B| \quad (1)$$

Typically, E_B is around 7.4eV and E_d is 25eV, which give E_P around 32eV.

Now we can imagine as a low energy ion reaches the surface of amorphous carbon, it does not have enough energy to penetrate the surface. More possibly, it will join the surface and remain in its lowest sp2 energy state. As the ion energy is greater than E_P, it has a chance to penetrate the surface and remain in a subsurface interstitial site [11]. As the density is increased in this local area, the bonding starts to reform between incident and target carbon atom. Here is an assumption suggested by Robertson that with the high energetic ion bombardment, orbital hybridizations will adjust easily to changes in the local density, and become more sp^2 if the density is low

and more sp^3 if the density is high [11]. As an ion has a much higher energy than E_P, it penetrates deeper into the surface. Compared to the ion energy, E_B is rather small. Although a certain fraction of the energy will be consumed during atomic displacements, there is still some ion energy left. It will be finally dispersed in the heat form of phonons. This process will cause thermalization and relaxation in local area and reduce the density. In other words, the sp3 bonding may be reduced at higher ion energies.

A mathematical characterization can be made according to the schematic shown in figure 2.6a. Assume there is an incident beam striking on the surface, in which energetic ions has a fraction of 'φ'. Also assume that a fraction 'f' of the ions has energy higher than E_P. So a fraction $f\varphi$ of the beam will penetrate into the surface. The rest including neutral atoms, radicals and low energy ions will remain on the surface. During the relaxation process, a fraction of the penetrating ions will go back to the surface (Figure 2.6b), which is proportional to the fraction of interstitials below the surface 'n'. Now we can express the fraction of the remaining ions as:

$$n = f\varphi - \beta n \tag{2}$$

Here 'βn' is the fraction of relaxing ions, where 'β' is a constant. Equation (2) gives:

$$n = \frac{f\varphi}{1+\beta} \tag{3}$$

The remaining fraction of the incident flux "1-n" on the surface does not cause densification as sp^2 sites. Assume the sp^2 density near surface is ρ, so the density increment along the film will be:

$$\frac{\Delta\rho}{\rho} = \frac{n}{1-n} = \frac{f\varphi}{1-f\varphi+\beta} \tag{4}$$

The amorphous nature of DLC films gives rise to range of activation energies leading to a stretched exponential relaxation behavior after thermalization process [32, 33]. The equation shows as below:

$$f = 1 - \exp\left(-\frac{E-E_P}{E_S}\right) \tag{5}$$

Where E_S is a constant. DLC film deposition is a metastable non-equilibrium process in which after deposition the film can not globally change its sp^3 hybridization to sp^2. This leads to local stress developments in the films with sp^3 sites under compression and sp^2 sites under tension. Deposition parameters should be modified to obtain a near stress-free film.

2.1.4 Hydrogenated amorphous carbon (a-C:H)

2.1.4.1 Deposition mechanisms of a-C:H

Compared to a-C, a-C:H has more deposition processes occurring either on the surface or at the subsurface (Figure 2.7). The presence of hydrogen and radicals plays an important role during the deposition. As mentioned earlier, the deposition method for a-C:H is usually RF PECVD. There are various source gases that can be used, such as CH_4, C_2H_2, C_2H_4 and C_6H_6. The bias voltage and temperature also largely affect the growth of a-C:H, which will be discussed in detail in next section. In order to fully understand the deposition mechanism, the chemical reactions between neutral species and the film, the dehydrogenation process, and the physical subplantation

should be all investigated.

Not like ta-C, the ion fraction of the flux is much less than 100%. The incident beam consists of a large fraction of neutral species. They could be neutral hydrocarbons, such as undissociated precursor gas (CH_4), diradicals (C_2H_4), mono radicals (CH_3), and unsaturated species (C_2H_2). Also atomic hydrogen possesses a large fraction of the neutral species.

The contribution of each neutral hydrocarbon to the growth rate depends on their sticking coefficient [11]. CH_4 has very low sticking coefficient due to the full out shell, so it will not affect much on the growth rate. On the contrary, C_2H_2 and C_2H_4 have a sticking coefficient close to 1, which means they can directly react with the surface C-H bonds. CH_3 lives between these two species. It can not directly react with a C-H bond, but it can form a “C-C” bond with a dangling bond on the surface. As we know, the a-C:H surface is fully covered with chemically passive C-H (H-C≡C-H) bonds. The carbon dangling bond is created when an ion or H atom or a CH_3 radical extract the H from the C-H bond. Then the CH3 radical will reacted with the dangling bond to form:

$$\equiv C\text{-}CH_3 \rightarrow \equiv C\text{-}CH_3$$

So it is actually not a typical C-C sp^3, but a ≡C-CH3 sp^3 bonding. Above all, the neutral hydrocarbons can only affect the surface.

The action of hydrogen atoms is much more complicated than the neutral radicals. As an atomic H impinges on a sp^3 site on the surface, it takes one H to form H_2 (dehydrogenation) and leaves a hydrocarbon radical which has a dangling bond.

The dangling bond may be saturated by another incoming hydrogen atom, or more likely, when the temperature is higher than 400K, relax by the thermally-activated split-off a CH_3 radical from a neighboring carbon atom (lower right in Figure 2.8, [34]). These two dangling bonds will rehybridize and form sp^2 graphite like surface shown in the bottom of figure 2.8. Further impinging H atom will saturate the sp^2 sites and transform them in a consecutive number of steps back to the starting sp^3 sites, as long as the radical is thermally stable and the temperature is high enough (above 600K) [34]. Compared to the hydrocarbons, hydrogen atoms are so small that they can easily penetrate the film and create a dangling bond in the subsurface [35]. Some of those subsurface dangling bonds will again be saturated by other impinging H atoms.

The carbon and hydrocarbon ions will penetrate the surface and follow the process illustrated in the subplantation model. As the bias voltage increases, the ion energy increases which causes more H being displaced from C-H bonds. This is the main reason that causes the H content in a-C:H depletes with increasing bias voltage, which will be discussed in next section. The H^+ ions have such a low mass that they can penetrate deepest into the surface with little interaction with C atoms. They react the same as H atoms but in a deeper depth. (Three depth theory suggested by Von Keudell, [35]).

2.1.4.2 Bias voltage and temperature effect

The bias voltage of RF PECVD has great effect on the a-C:H bonding structures and thus mechanical properties. As mentioned above, the content of H decreases with

increasing bias voltage (here all the bias voltages are negative, the absolute value is increasing). In PECVD, the sp^3 content correlates with the H content. The H saturate the C=C bonds and change sp^2 C bondings to $sp^3{=}CH_2$ or $sp^3{\equiv}CH$ sites, rather than increase the C-C bonds. So at a low bias, the film has a large H and sp^3 content and low density. Large sp^3 content does not bring high hard, because the C-C sp^3 bonds are the key to mechanical properties, not the H saturated sp^3 bonds. The pure carbon sp^3 fraction is low due to the less ion bombardment. At intermediate bias (100V), the H content becomes less as bias increase. Although the total sp^3 content is decreased, the C-C sp^3 bond is increasing due to the greater ion bombardment and reaches maximum. The density is also highest as well as the Young's modulus. As the bias keeping increasing, the H content keeps decreasing and the bonding become sp^2 like. It is believed by Jiang that the mechanical properties of a-C:H is affected by the sp^2 (graphite) clusters in the matrix of H saturated C-C sp^3 matrix [3]. As bias becomes high, the cluster size increases, which softens the a-C:H film. As the sp^2 cluster becomes larger and larger, it finally dominates the mechanical properties. Figure 2.9a shows how the total sp^3 fraction and H content decrease continuously with increasing V_b [36] and Figure 2.9b illustrates how the Young's modulus changes with V_b suggested by Jiang [3].

The temperature dependence of a-C:H growth is also important. The atomic hydrogen will not only help the deposition process but also etch the film in a certain rate [37]. The increasing temperature has little effect on the growth rate from ions and neutral radicals. However, the etching rate of H atom rises dramatically, which causes

the total growth rate decreasing [37-38]. Figure 2.10a and 2.10b show the change of a-C:H deposition rate and etching rate with increasing V_b, respectively.

2.2 MEMS devices

2.2.1 Overview

Micro-electro-Mechanical Systems (MEMS), the integration of mechanical microstructures with microelectronics, are now widely used in various fields, such as automobile sensors, ink-jet nozzles, magnetic hard drives, microphones and biomedical detecting and sensing. Generally, MEMS devices can be divided to two families: sensors and actuators. The core element in MEMS always consists of two principal components: a sensing/actuating element and a signal transduction unit [39]. A MEMS sensor is used to sense the mechanical motions of the microstructures. In other words, it transfers the mechanical energy to electrical signals with can be measured by certain devices. On the contrary, in actuators the electrical (or other forms like electrothermal and piezoelectric) energy is converted into mechanical movement of the microstructures. Figure 2.11 shows the various kinds of MEMS devices in a tree table.

2.2.2 Microfabrication process of MEMS devices

The continuously decreasing size of integrated circuit (IC) devices leads to the development of microfabrication process as an independent discipline. Many efforts have been dedicated to this field in recent decades. A typical Microelectronic fabrication always involves the processes of thermal oxidation, lithography, diffusion and ion implantation, film deposition, wet/dry etching, interconnections and contacts,

and final packaging. The fabrication procedures relevant to this project will be discussed in detail in experimental part.

MEMS micromachining can be classified into three categories: (i) bulk micromachining, (ii) surface micromachining, and (iii) high-aspect-ration electroplated structures (LIGA process) (Jaeger [40]).

Bulk Micromachining involves the selective removal of materials from the substrates to obtain a desired structure. The substrate can be etched with either wet (chemical) or dry (plasma) etching. For silicon substrate, a solution of KOH (hydroxide potassium), water and propanol is always used to perform an anisotropic wet etching. As we know, silicon is not isotropic in its diamond cubic crystal structure, which means some orientations (planes) are much stronger to resist etching. Usually, the <111> planes etches at much lower rates than <110> and <100> planes. An experimental etch ratio of these three plane is 1:30:40, respectively. The etch rate selectivity can be used to create various cavity and groove structures [40]. Figure 2.12a shows a <100> silicon wafer etched by KOH. The (111) plane has an angle of 54.74° with (100) plane. In our project, such kind of cavity is used to give freestanding DLC membranes. <110> silicon wafers are also frequently used in IC industry due to the clean etching in this direction. As <111> planes become the side wall during etching, a vertical cavity can be obtained [41] (figure 2.12b).

In contrast to bulk micromachining in which substrate material is removed by physical or chemical means, the surface technique builds the microstructure by adding materials layer by layer on top of the substrate [39]. Structural and sacrificial layers

are both involved in the process. A typical surface micromachining flow is shown in figure 2.13.

Both bulk and surface micromachining have two disadvantages: low geometric aspect ratio and use of silicon based materials [39]. LIGA [lithography (Lithographie), eletroforming (Galvanoformung), and molding (Abformung)] process is a now technique that can overcome these shortcomings. It uses deep X-ray lithography technique to develop x-ray resist [polymethyl methacrylate (PMMA)]. Then the metal is deposited on the PMMA side wall using electrodeposition technique. Metal structure is then released from removing the X-ray resist.

2.2.3 DLC role in MEMS devices

Ta-C and a-C:H are the prospective protective-coating materials for MEMS [42-44] due to the superior wear-resistant qualities, resistance to stiction and potential as a biocompatible material for MEMS cantilever-based sensors that could be used inside the human body for medical purposes without generating an allergic reaction. As mentioned earlier, NFC films with acceptable mechanical strength and extreme tribological properties are good candidates for the MEMS protective coating. Also, previous work in our research group has explored NFC film as passivation layer for piezoresistive microcantilevers. Passivation step is important in microfabrication process as it is the final step and must meet stringent requirements. Any material for passivation layer should have low residual stress, high etch resistance, and low pin-hole density [45]. NFC film turns out to meet those requirements and work better than the present passivation materials such as SiO_2 and Si_3N_4.

2.2.4 MEMS fabrication problems

a. Adhesion of layers

When two layers of different or same materials are put together, there is always a chance for delamination at the interface either by peeling of one layer from the other or by shear that causes the wavering of the interfaces locally along the interface [39]. Excessive thermal and mechanical stress and surface conditions are the three main reasons that cause delaminations.

b. Interfacial residual stresses

Due to the different coefficients of thermal expansion (CTE) between film and substrate materials, interfacial residual stress (compressive or tensile) may be generated during thin film deposition at a high temperature. As the temperature cools down, the whole structure will be bent due to the stress gradient along film thickness. Figure 2.14 shows the schematic of interfacial residual stress [39].

c. Stiction

During the surface micromachining process, the sacrificial layer will be removed from the middle of the surface structure and the substrate. The surface structure once supported by the sacrificial layer may collapse on to the substrate. Stiction is the most serious problem in surface micromachining process. Eternal forces are always needed to separate two layers when stiction occurs.

2.3 Thin films

As thin films dimensions begin to approach that of the film microstructural features, the materials mechanical properties begin to exhibit a dependence on the specimen size [8]. In other word, as film thickness reduces to micro size, those data obtained from bulk materials are no longer suitable for thin film mechanical properties. Usually, the plastic behavior, fracture strength and fatigue resistance will have the size effects when film thickness reduces to micron scale or smaller, while the elastic properties, which depend on the material bonding structure, will not exhibit the size effects until in the nanoscale. Figure 2.15 shows the schematic of length-scale effects on the mechanical properties. The membrane size effects on DLC mechanical properties (except Young's modulus and other elastic properties) begins when one or two of the membrane dimensions (length, width and thickness) start to approach the micron scale. The geometric constraints, surface effects and competition of deformation mechanisms which control the plastic deformation are all affected by the size effects [8]. Moreover, as the film sizes reduce, the microstructures like grain size will change, which has an effect on the plastic behavior. Detailed size effects will be applied in Results and Discussion section.

2.4 Nanoindentation

2.4.1 Overview

Nanoindentation, also known as depth-sensing indentation and instrumented indentation testing (IIT) is a relatively new form of mechanical testing that significantly expands on the capabilities of traditional hardness testing [46]. Nanoindentation test can be either static (Oliver and Pharr [47]) or dynamic (continuous stiffness measurement [48]). Usually, a nanoindenter tip made of diamond is driven into and withdrawn from a sample material. During the process the loads and displacements of the tip are recorded by the monitoring system, from which mechanical properties can be derived. Figure 2.16 shows the schematic of an indentation system. Indenters with various shapes are used for different purposes. Pyramidal indenters also well known as Berkovich tips are probably the most frequently used shape. The three-sided pyramid can ground to a very small point, which will keep its geometry to the minimum scales. Besides the Berkovich tip, spherical, cube-corner, conical, and Vikers pyramid indenters are also applied. Table 2.2 shows their geometries and parameters. It is necessary to mention that displacements measured in a nanoindenter system include the information of the compliance of the tip itself. The accurate mechanical properties should be obtained from removing this component from the raw load-displacement data.

2.4.2 Measurement and principles

As the indenter tip is forced into the sample, both elastic and plastic deformations occur. As shown in Figure 2.17, h_c represents the contact length of a

berkovich tip in the sample. The contact area has a radius of a. When the tip is unloading from the sample, only the elastic recovery involves, which effectively allows one to separate the elastic properties of the materials from the plastic [46]. The residual depth of the indentation caused by plastic deformation is h_f. The slope of the unloading curve is given by S=dP/dh, where P is the load. The traditional equations of Young's modulus (E) and hardness (H) are given as:

$$E_r = \frac{\sqrt{\pi}}{2\beta}\frac{S}{\sqrt{A}} \tag{6}$$

Where E_r is the reduced elastic modulus, A is the projected contact area of contact under load, and β is a constant that depends on the geometry of the indenter tip [44].

$$H = P / A \tag{7}$$

As the indenter is loading/unloading in the sample, elastic deformations occurs in both the sample and the tip. The accurate Young's modulus of the sample material E should be:

$$\frac{1-\upsilon^2}{E} = \frac{1}{E_r} - \frac{1-\upsilon_i^2}{E_i} \tag{8}$$

Where υ is the poisson's ratio of the sample, and E_i and υ_i are the Young's modulus and poisson's ratio of the tip, respectively.

2.4.3 Problems of nanoindentation

a. Pile-up and sink-in

A berkovich tip, as mentioned earlier, is a three-sided pyramid indenter. Due to its sharpness, pile-up plastic deformation will occur when it is driven into the material (does not occur in hard metals). As shown in figure 2.18a [8], material buckles up

around the tip, which causes the contact area larger than the theoretical sink-in situation. So the mechanical properties of the pile-up material might be smaller than those obtained from equation 6-8. It is always wise to use SEM or light microscope to characterize the surface after indenting. The edges of pile-up indentations have a distinct appearance: the sides of the residual hardness impression are bowed outwards and shown in figure 2.18b [46].

b. Thin film substrate effect

The indentation measurement of thin films is much more difficult than bulk materials, because the data come from both the thin film and the substrate. The traditional way to avoid substrate effect is making the indenting depth a very small fraction of the film thickness. The properties of the film can be evaluated independently of the substrate as long as the indentation depth is less than 10% of the film thickness [49]. However, the experimental data is still not so accurate when the film thickness is less than 500nm. This is the main reason that we are using MDE test to determine the DLC mechanical properties, so that the substrate effect can be minimized.

2.5 Membrane deflection experiments (MDE) of NFC thin films

MDE test was first developed by Espinosa and Prorok [7]. The basic idea was to establish a way to measure stress and strain independently so that the interface-driven affect can be minimized. Also, MDE test could eliminate the effect of substrate, since the tests are based on freestanding membranes. As mentioned in the introduction part,

a dog-bone shape membrane is fixed at both ends. The center part of the membrane has a larger area to minimize the stress concentrations as the load is applied. The tapered region of the membrane is to eliminate boundary failure effects. As the membrane is bended by the nanoindenter tip at the center, an interferometer beneath the membrane is used to record the deflection information. A photograph of MDE experimental setup is shown in figure 2.19. As the die with membranes is put on the stage, the first thing need to do is locating the membranes position and characterize their shape. Then the interferometer and indenter tip should both be aligned with the membrane to avoid spurious effects such as torsioanl forces and errors in true deflection [7]. The interferometer should be rotated in X and Y directions to eliminate all the “unnecessary fringes” (especially fringes in X direction). Figure 2.20a shows the interferometer image of the bottom side of an unloaded membrane. Due to the curve surface of the membranes caused by the residual stress, there should be some Y direction fringes left on the picture. But it is necessary to adjust the interferometer in X direction to make even fringes on each side. The second step is to align the membrane with nanoindenter. If the alignment is perfect, the fringes will develop uniformly shown in figure 2.20b. If the membrane and interferometer is misaligned, the fringes will have an angle shown in figure 2.20c. In this situation, the membrane has been twisted by the indenter to make a full contact between the tip and the surface (figure 2.21). As all the alignments are finished, the membranes will be treated with MDE tests.

The raw data from the MDE test should be treated with data reduction so as to

obtain the accurate mechanical properties. As the membrane is bent down during the fabrication process, the starting point that the tip touches the membrane shall change. Thus, additional parameters are needed for data reduction, such as the bending degree (Δc) below the wafer plane and the whole length (L_M') of the membrane in its out-of-plane configuration [50]. The data reduction part will be described in greater details in the results and discussions.

Figure 2.22a illustrates the relation between nanoindenter vertical load P_V and membrane in-plane load P_M. The equations are:

$$\tan\theta = \frac{\Delta}{L_M} \tag{9}$$

$$P_M = \frac{P_V}{2\sin\theta} \tag{10}$$

The stress is calculated as:

$$\sigma(t) = \frac{P_M}{A} \tag{11}$$

where A is the cross-sectional area of the membrane in the gauge region [50]. Figure 2.22b shows the relationship between fringe distance (δ), vertical displacement, and the bending angle θ. The strain is obtained as [50]:

$$\varepsilon(t) = \frac{\sqrt{\delta^2 + (\lambda/2)^2}}{\delta} - 1 \tag{12}$$

2.6 Raman spectra of DLC materials

Raman spectroscopy is the measurement of the wavelength (frequency) and intensity of inelastically scattered light (photons) from molecules. When photons

interact with molecules, most of them are elastically scattered, which is called Rayleigh scattering. In Rayleigh scattering, the emitted photon has the same wavelength as the absorbing photon. Raman Spectroscopy is based on the Raman effect, which is the inelastic scattering of photons by molecules. The frequency shift between incident and scattering photons contains the unique material information of the molecules. The Raman shift is given by:

$$\nu = \frac{1}{\lambda_{incident}} - \frac{1}{\lambda_{scattered}} \tag{13}$$

Figure 2.23 gives the Raman spectra of diamond, graphite and DLCs [11]. For most of diamond like carbon, there are two peaks (modes) dominate the spectra. One is around 1360 cm^{-1}, which represents the disordered graphite labeled as ‘D’. Another is around 1590 cm^{-1}, which represents the crystal graphite labeled as ‘G’. Both of them involve the participation of sp^2 clusters. This is the reason that the sp^3/sp^2 ratio can be determined from Raman data.

Raman is light scattering by the change in polarizability χ due to a lattice vibration [51]. The Raman cross-section (C) can be expressed as

$$C = k\left(\frac{\partial \chi}{\partial \omega}\right)^2 \tag{14}$$

The Raman intensity is proportional to the product of Raman cross-section and the vibrational density of states (VDOS). In the bonding structures of amorphous carbon, the π states are lower energy than the σ states so that they get more chances to be polarized. This makes the intensity from sp^2 sites in DLC a 50-230 times larger than that from the sp3 sites [52-53]. This is the reason that sp^2 dominates the Raman

spectra even the sp^2 content is less than 10% in ta-C. In other words, the Raman intensity is controlled by the order of sp^2 sites, not by the sp^2 fraction [54]. The G peak represents all the sp^2 sites including C=C chain and aromatic rings, while D peak only counts for those sp^2 sites in rings. That makes the Intensity of G peak higher than that of the D peak. Many factors can cause these two peaks shifting and change their intensities, such as clustering, ratio of sp^2 chains and rings, and sp^3 fraction. In a-C:H, the sp^3 content increases with increasing H content. The hydrogen saturates the sp^2 sites and changes them to hydrogenated sp^3 sites. This is different from the mechanism in ta-C that sp^2 rings are broken into chains and then change to sp^3 sites. As a-C:H retains some aromatic ordering of sp^3 sites, the increase in sp^3 fraction has alloying effect, which causes the G peak to move down (left) [11]. The G position varying with sp^3 fraction is unique that can be used to derive the sp^3 fraction from the Raman spectra. For our NFC6 a-C:H, the bias voltage was intermediate, so that there are still some sp^2 sites in aromatic ring form. The D peak should exist. The ratio of I_D/I_G could also give the information of sp^3 fraction (figure 2.24, [55]). A He-Cd laser with a wavelength of 441.6nm or a He-Ne laser with a wavelength of 632.9nm is often used as the incident beam for Raman spectroscopy.

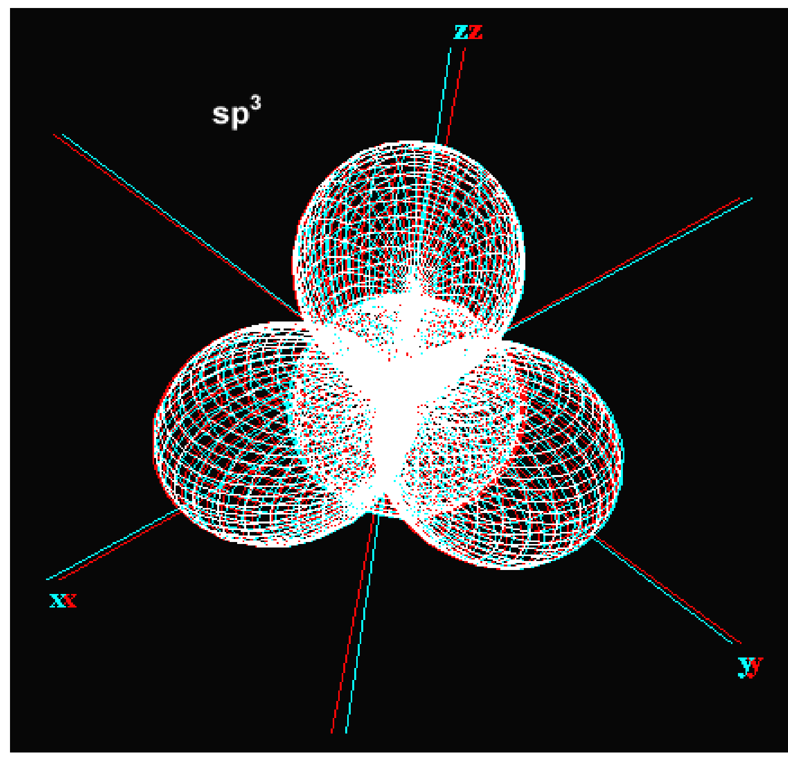

Figure 2.1a sp3 hybridization.

Courtesy of “IN-VSEE”: http://invsee.asu.edu/nmodules/Carbonmod/bonding.html

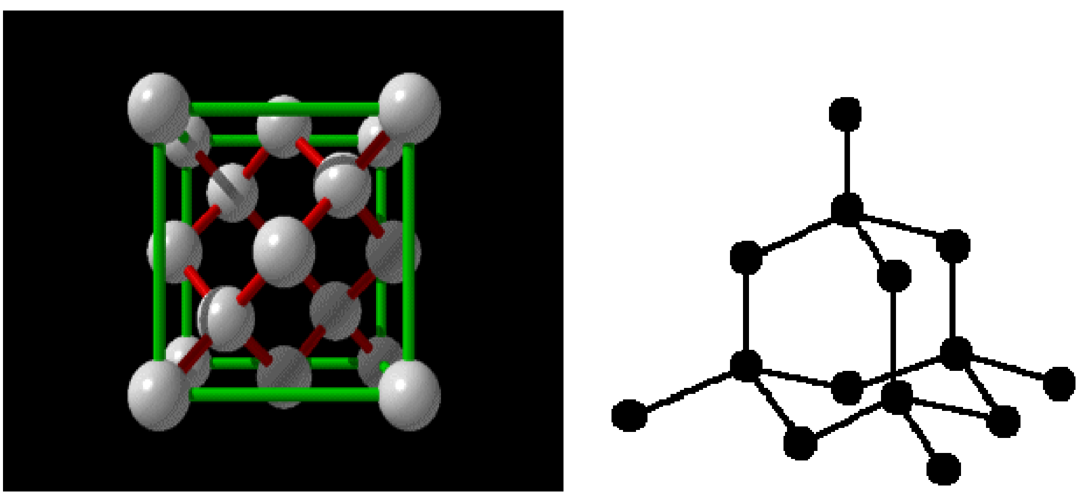

Figure 2.1b Diamond FCC structure

http://www.uncp.edu/home/mcclurem/lattice/diamond.htm

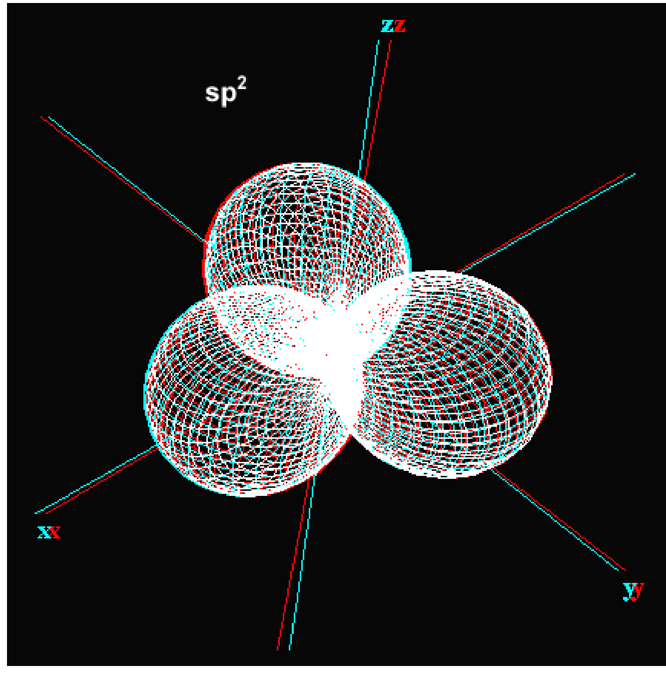

Figure 2.2a sp^2 Hybridization

Courtesy of “IN-VSEE”: http://invsee.asu.edu/nmodules/Carbonmod/bonding.html

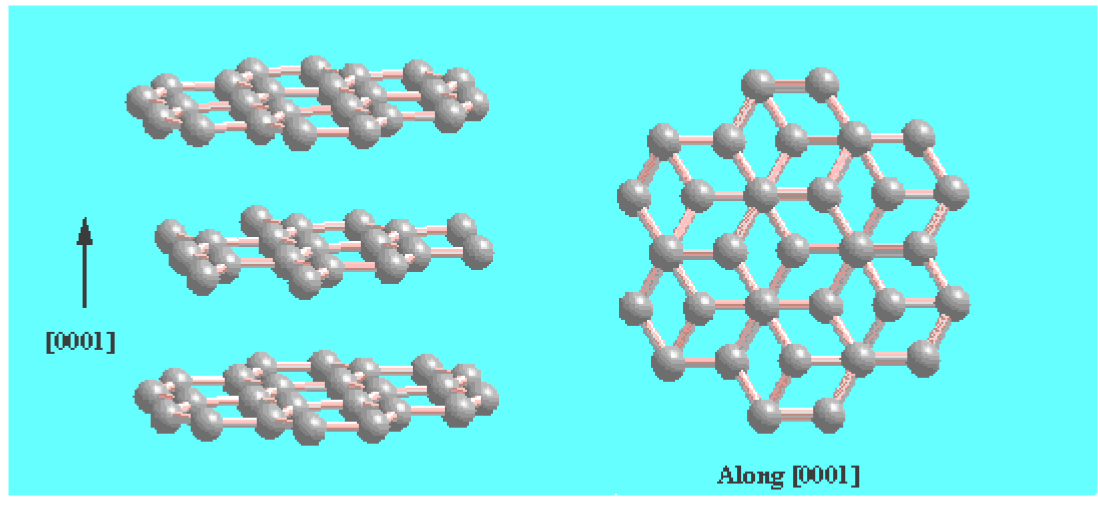

Figure 2.2b Graphite sheet structure

http://www.phy.mtu.edu/~jaszczak/structure.html

Figure 2.3 Various deposition systems for DLC [11]

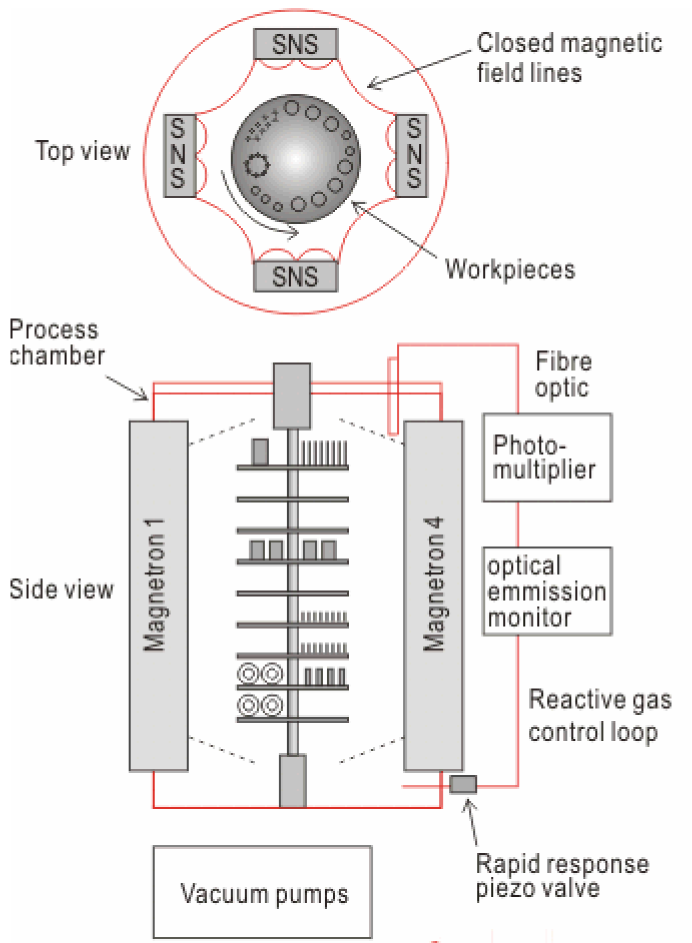

Figure 2.4 Magnetron sputtering system

http://www.azom.com/details.asp?ArticleID=623#_The_Closed_Field

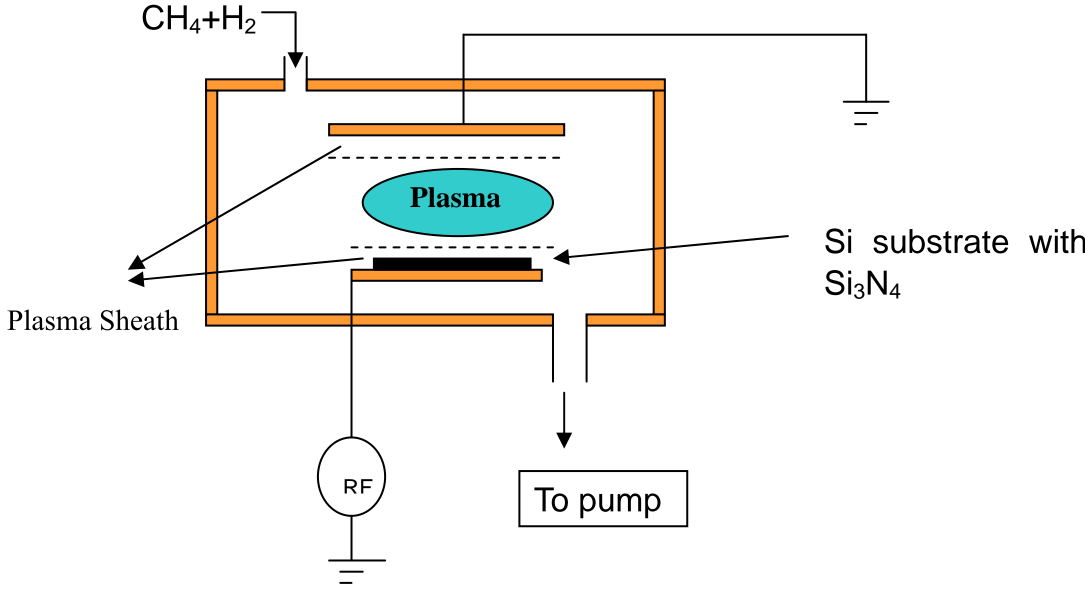

Figure 2.5 Schematic of RF PECVD and plasma sheath

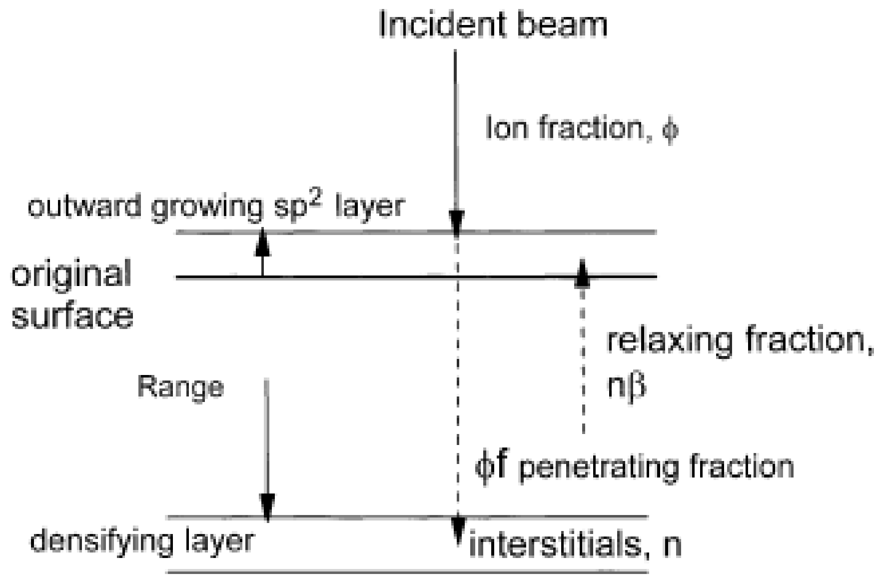

Figure 2.6a Subplantation model for DLC deposition mechanisms [11]

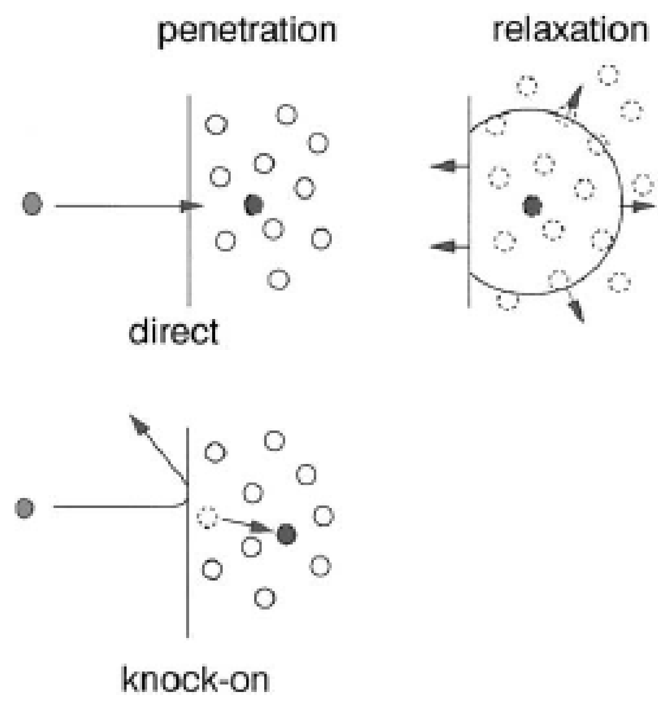

Figure 2.6b Penetration and relaxation process during DLC deposition [11]

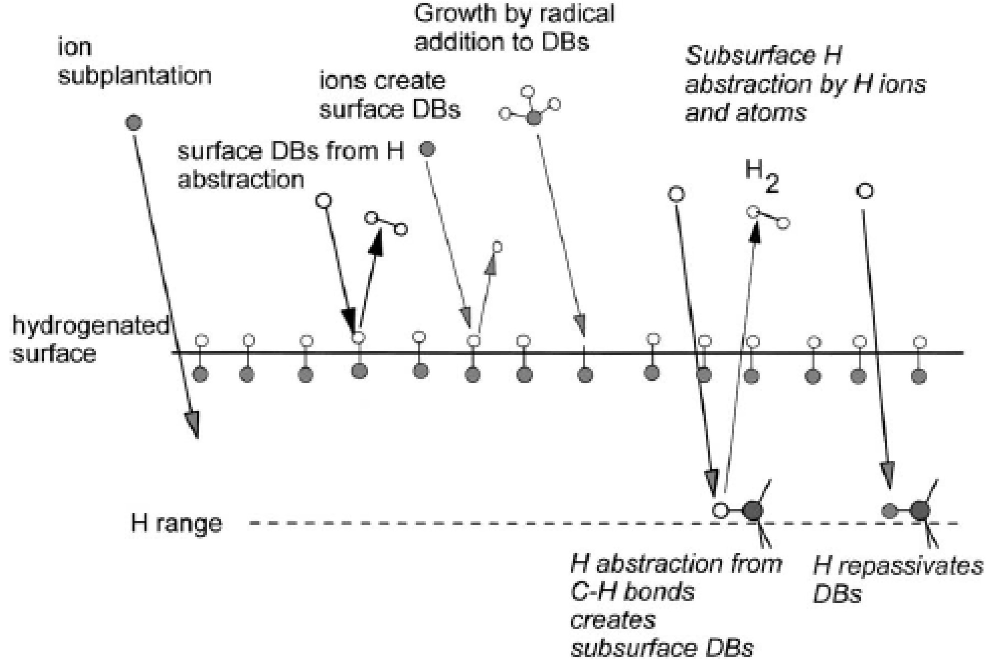

Figure 2.7 Deposition mechanisms for a-C:H [11]

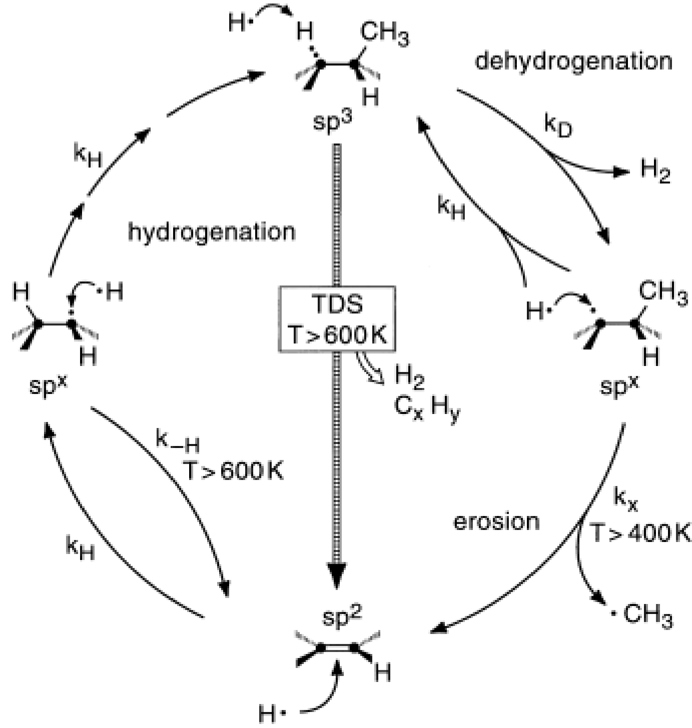

Figure 2.8 H erosion effect during a-C:H deposition [34]

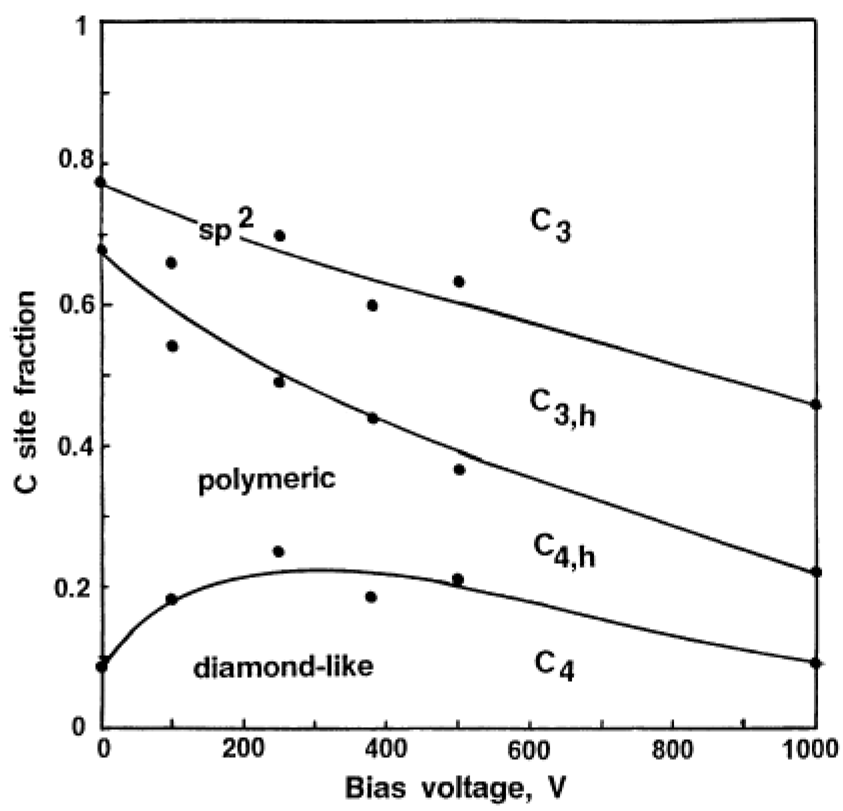

Figure 2.9a C sites change with bias in a-C:H deposition [36]

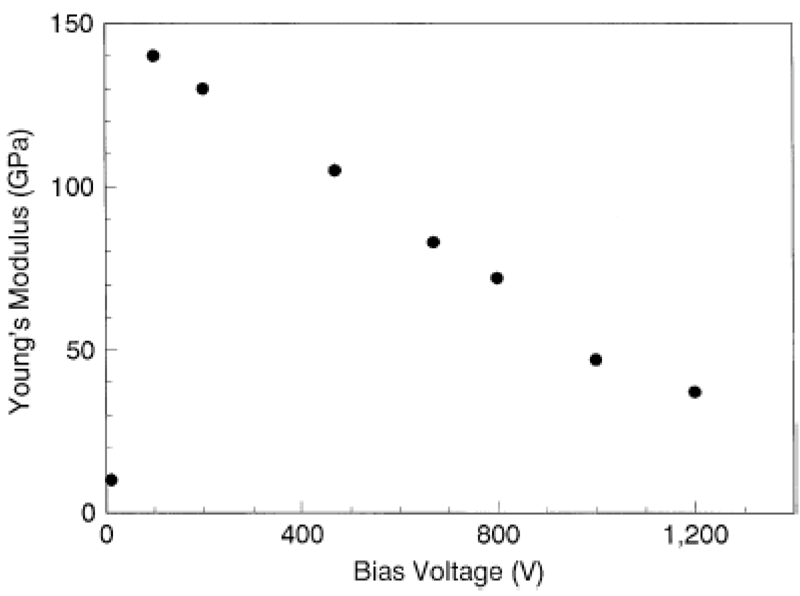

Figure 2.9b a-C:H Young's Modulus vs. Bias voltage [3]

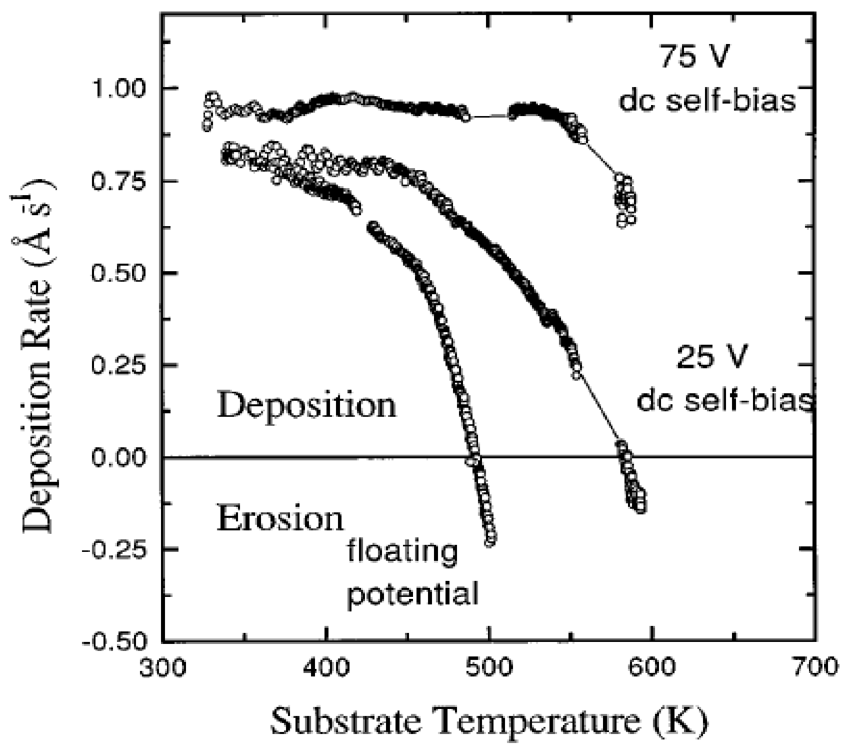

Figure 2.10a Temperature effect on a-C:H deposition rate [34]

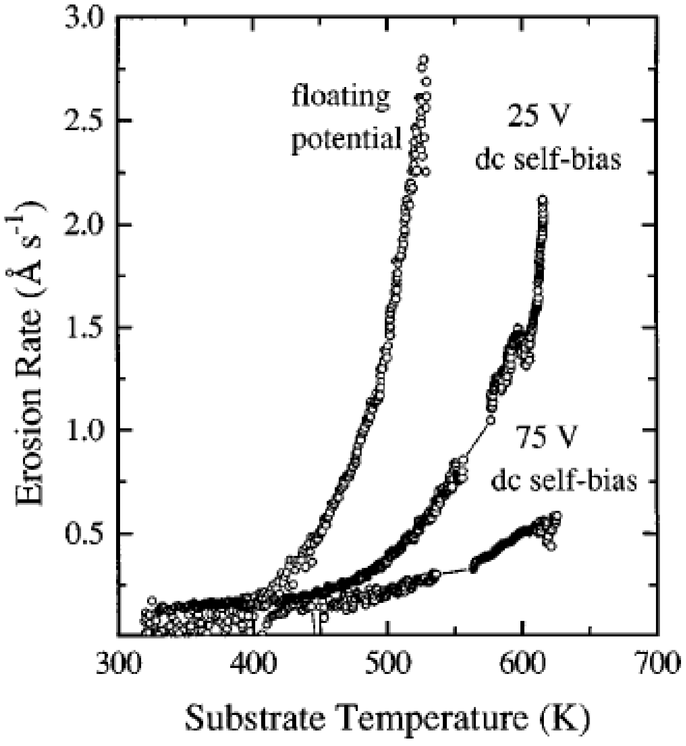

Figure 2.10b Temperature effect on H erosion rate [34]

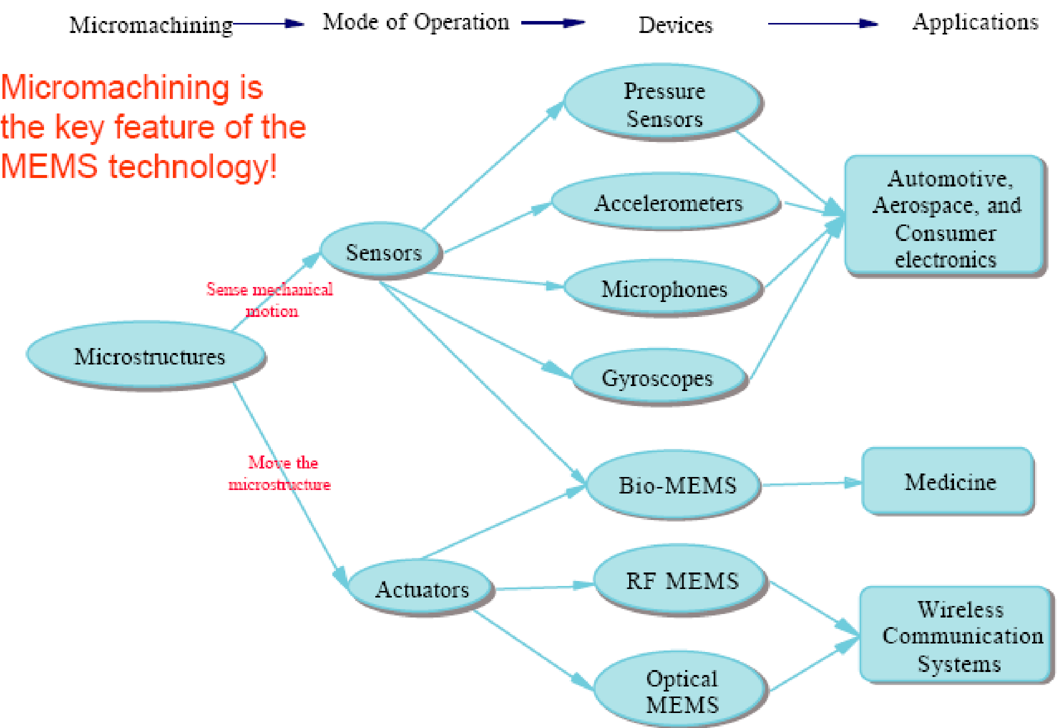

Figure 2.11 Different types of MEMS devices

Courtesy of Dr. Ramadas, Department of Electrical and Computer Engineering,

Auburn University

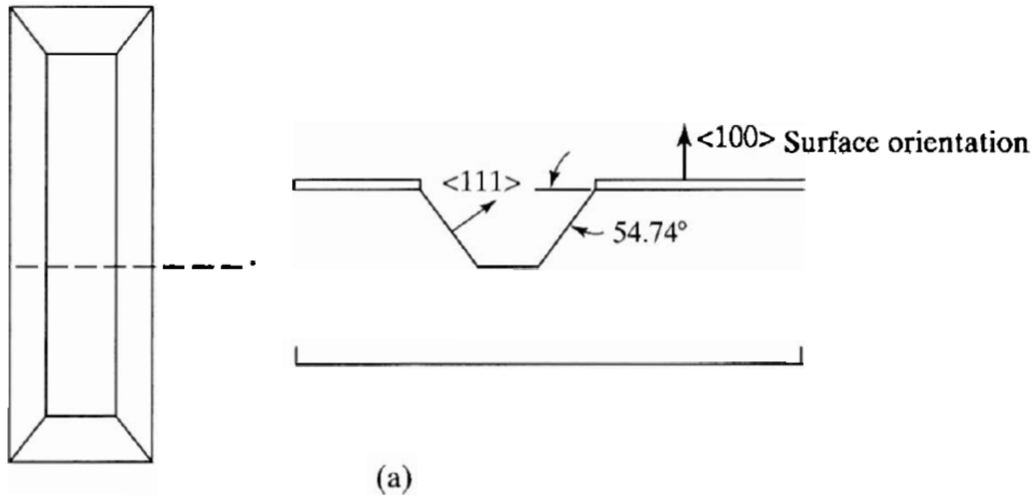

Figure 2.12a <100> KOH etching [40]

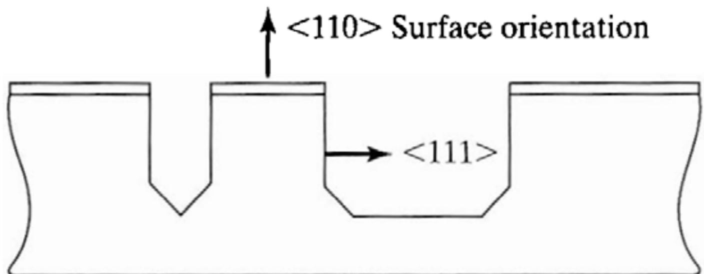

Figure 2.12b <110> KOH etching [40]

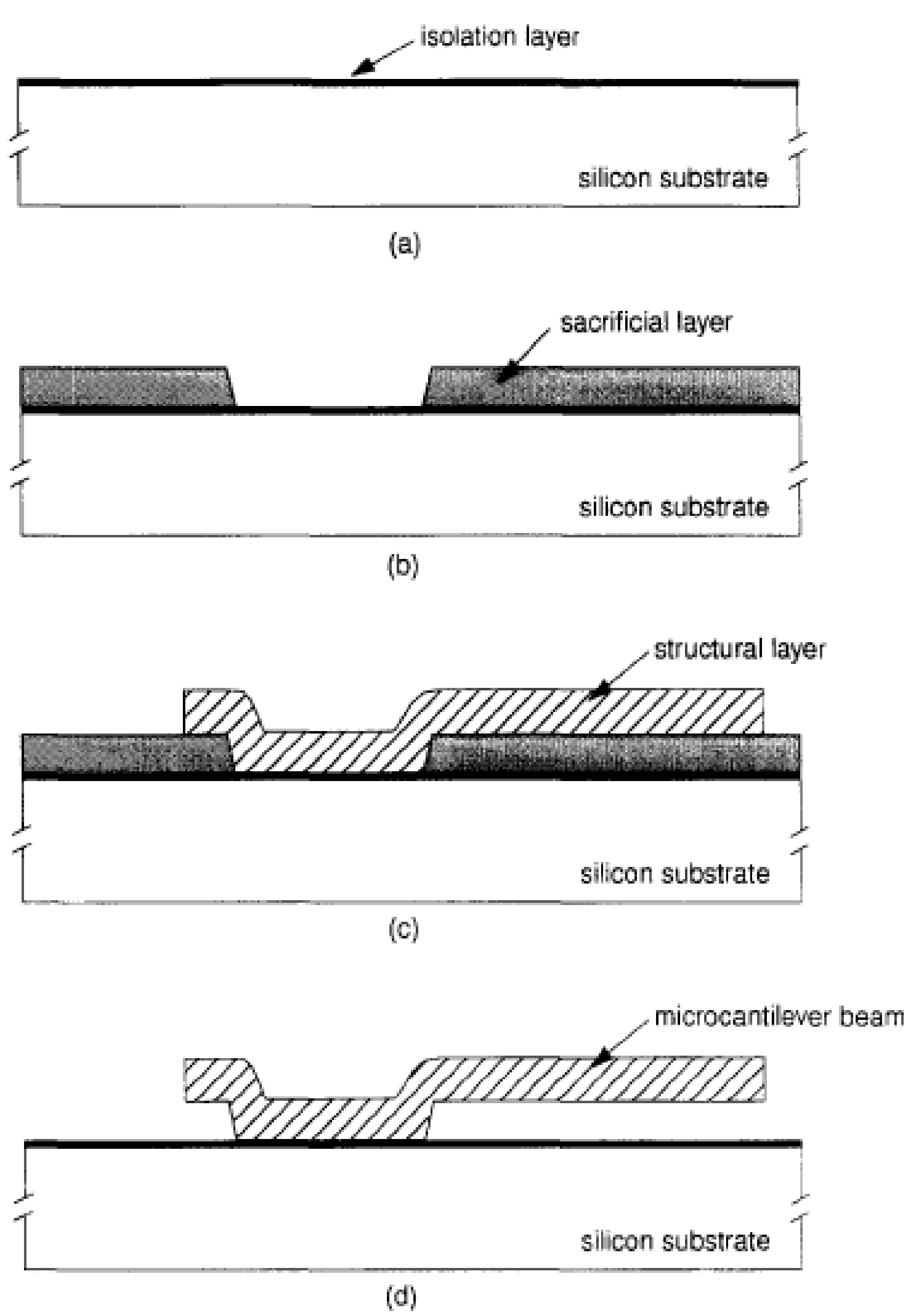

Figure 2.13 Surface micromachining [42]

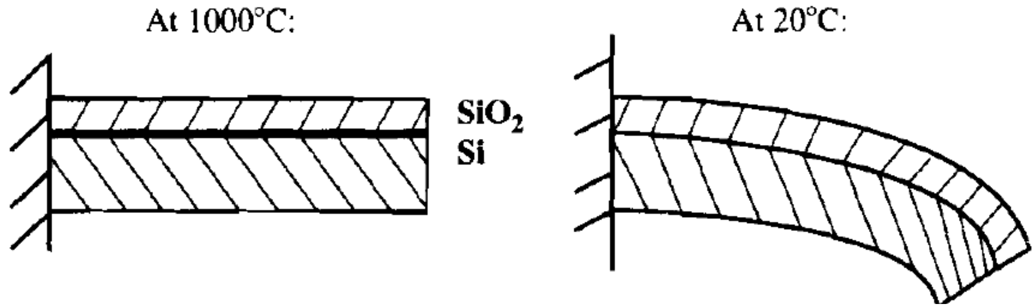

Figure 2.14 Interfacial residual stress for cantilevers [39]

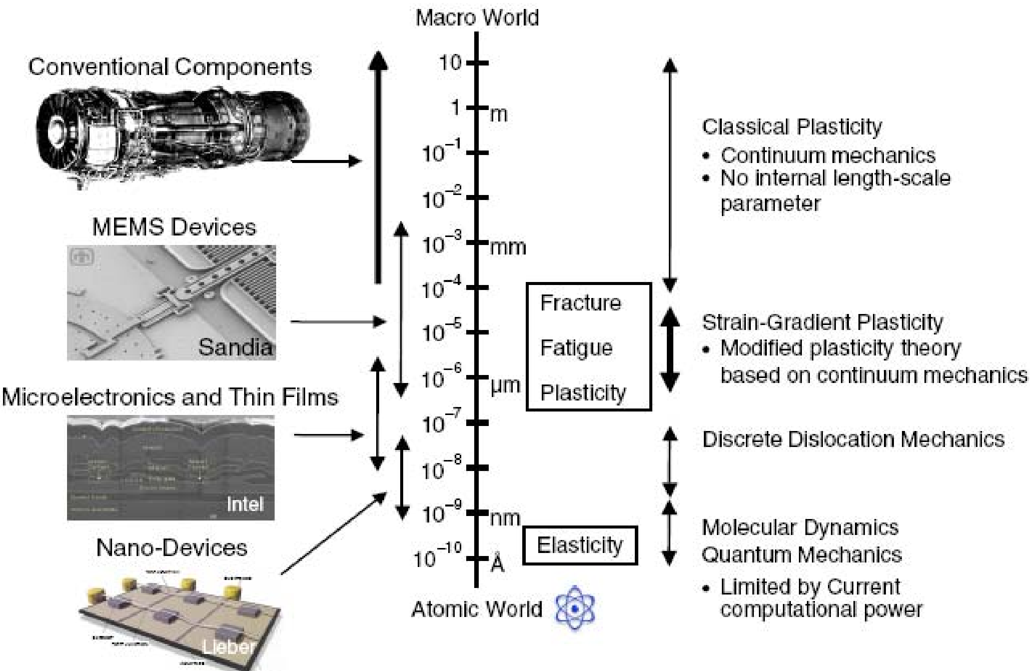

Figure 2.15 Illustration of length-scale effects on the mechanical properties of materials [8]

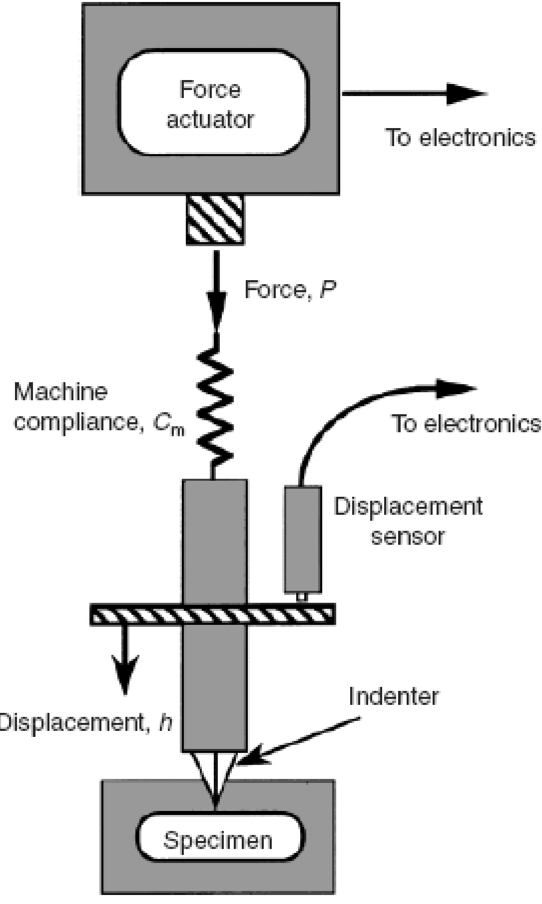

Figure 2.16 Schematic of the basic components of a nanoindenter [46]

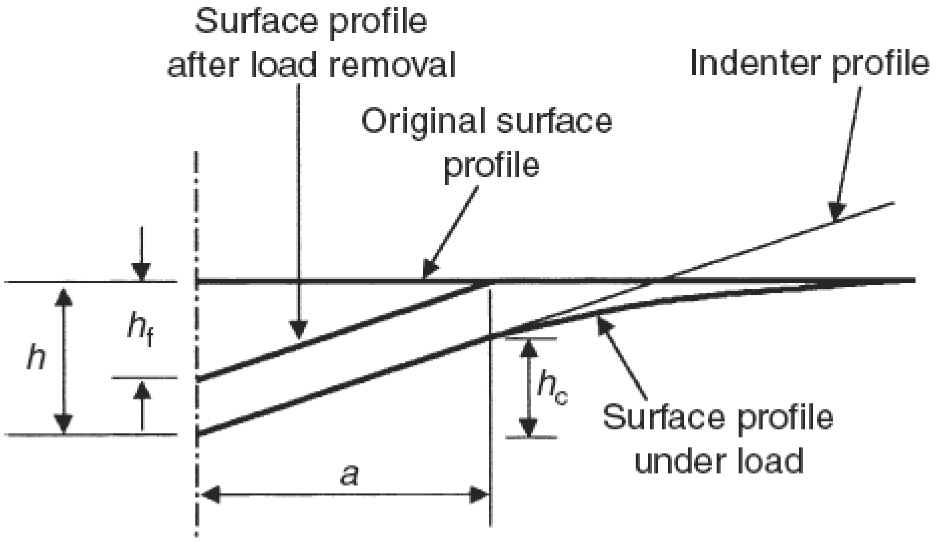

Figure 2.17 Schematic of nanoindentation [46]

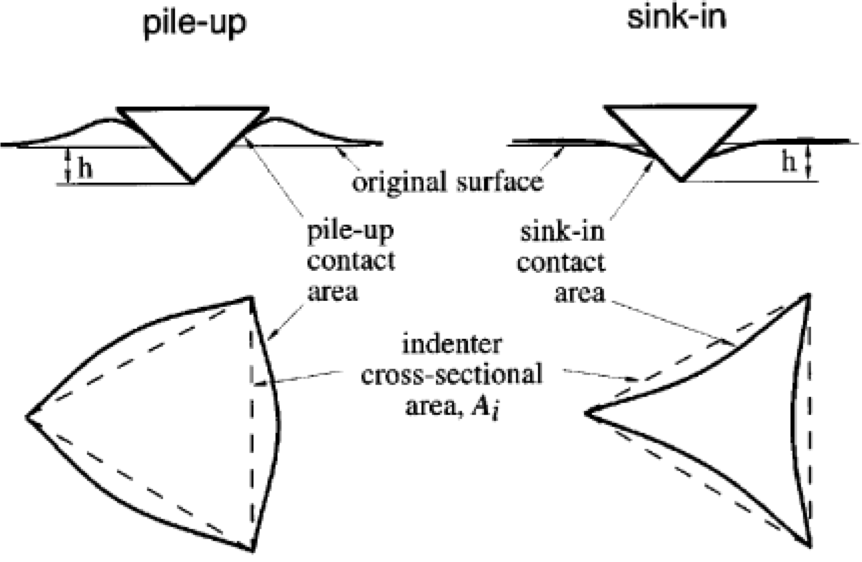

Figure 2.18a Pile up and sink in [8]

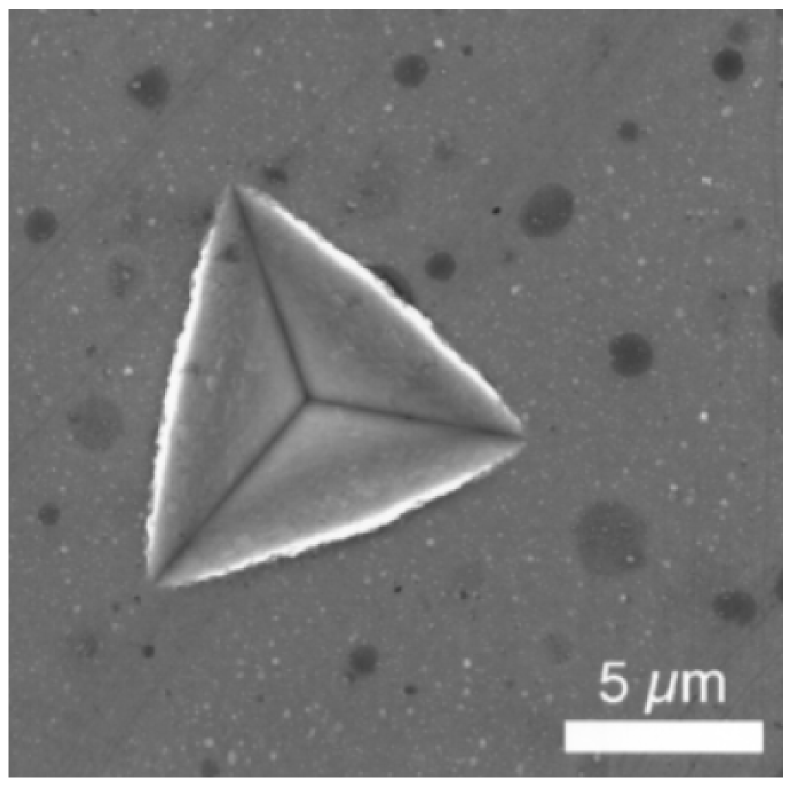

Figure 2.18b Berkovich indentation in aluminum. The distinctly bowed-out edges of the contact indicate pile-up. [46]

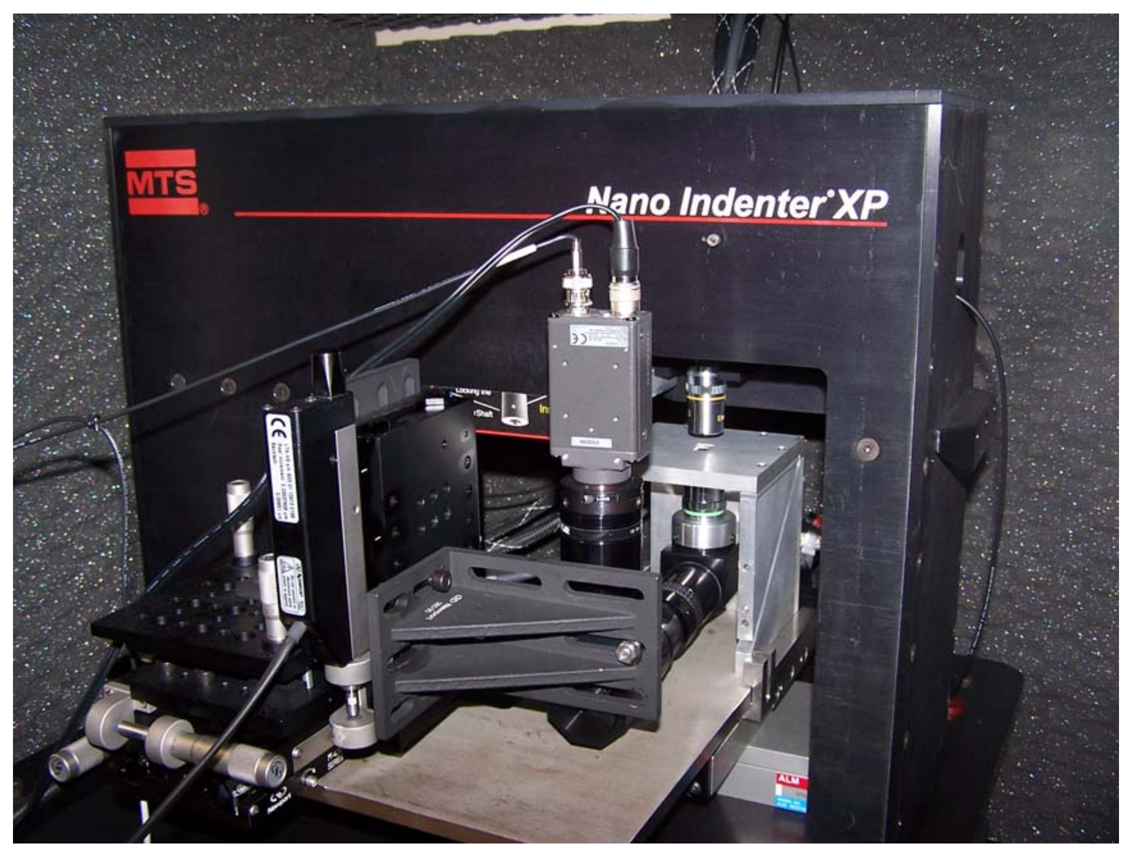

Figure 2.19 Nanoindenter and interferometer for MDE tests

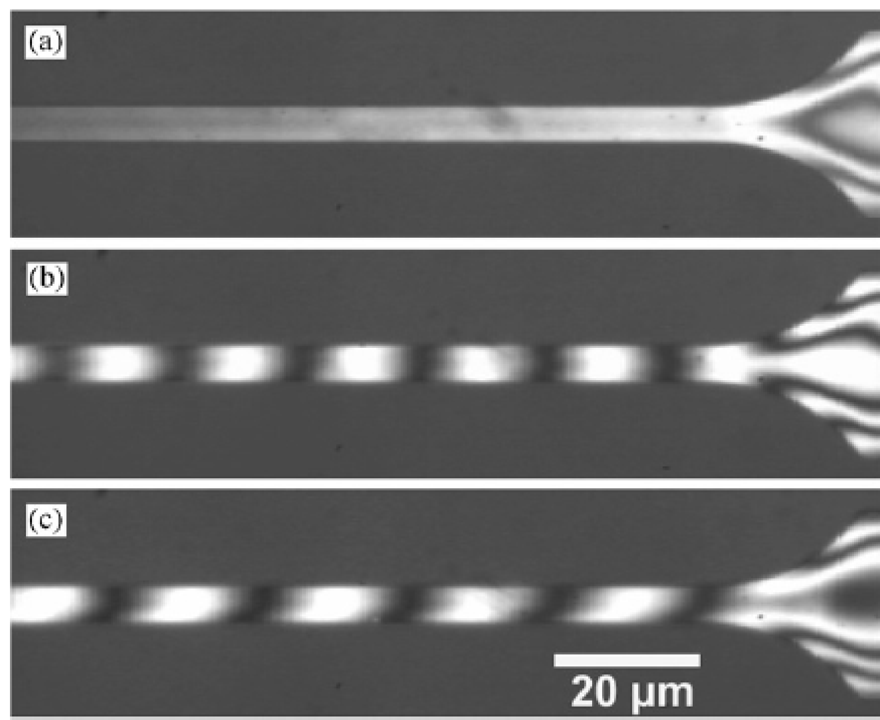

Figure 2.20 Interferometer images of the bottom side of the membranes showing: (a) an unloaded membrane; (b) a membrane under load in which the nanoindenter tip, membrane, and interferometer are well aligned; (c) a membrane under load in which the nanoindenter tip, membrane, and interferometer are out of alignment. [7]

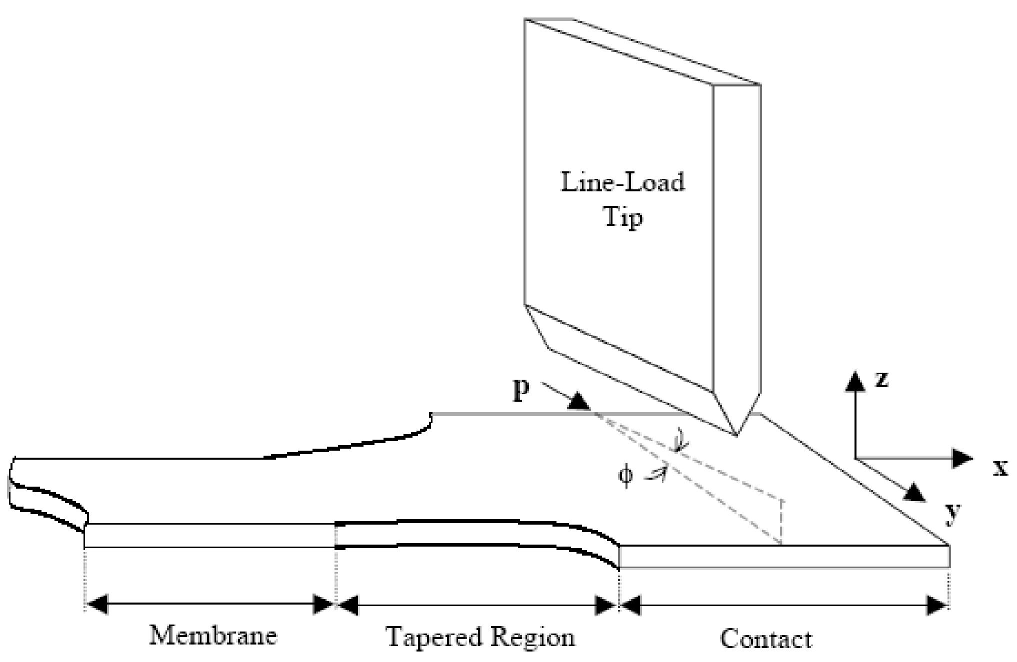

Figure 2.21 Misalignment between tip and membrane [7]

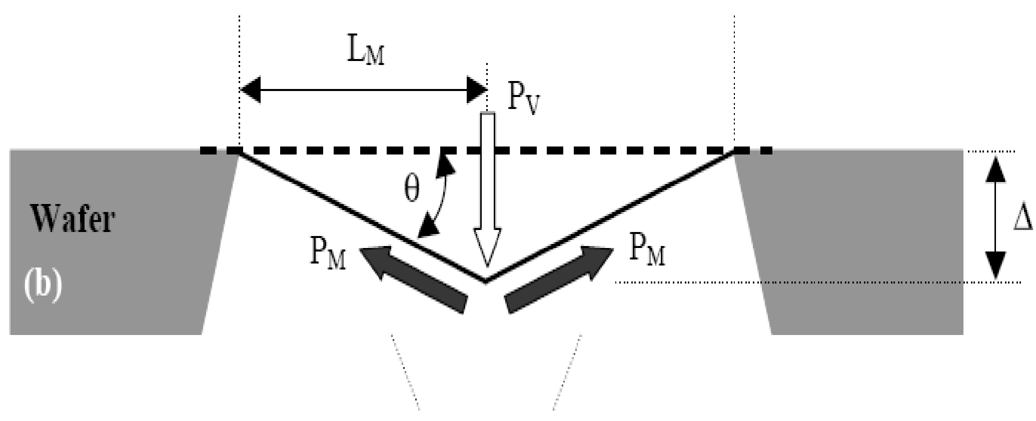

Figure 2.22a Schematic of MDE [50]

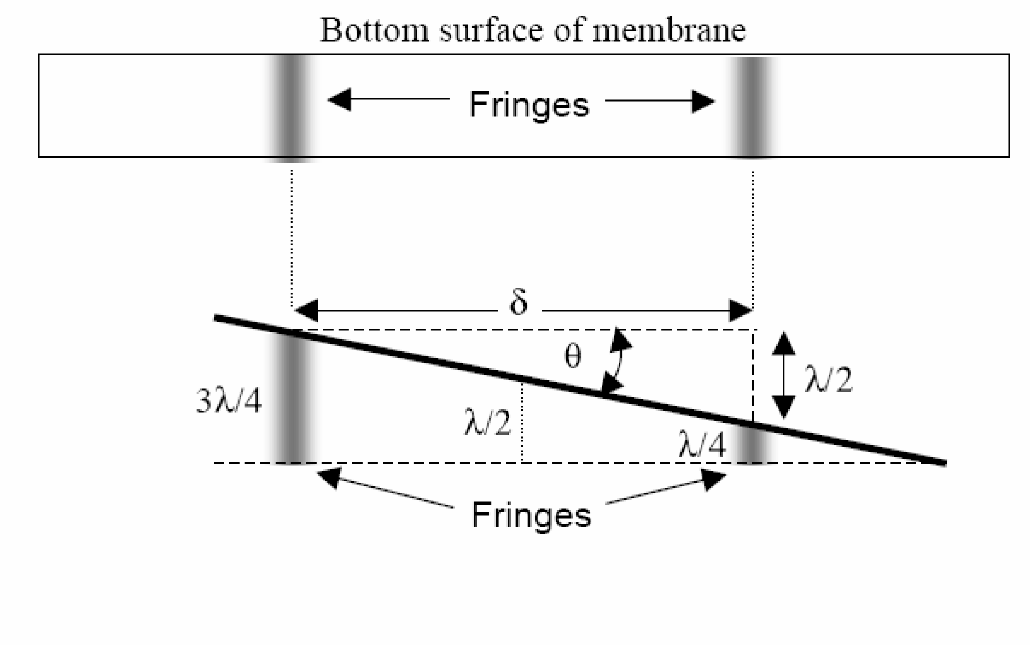

Figure 2.22b Schematic of MDE [7]

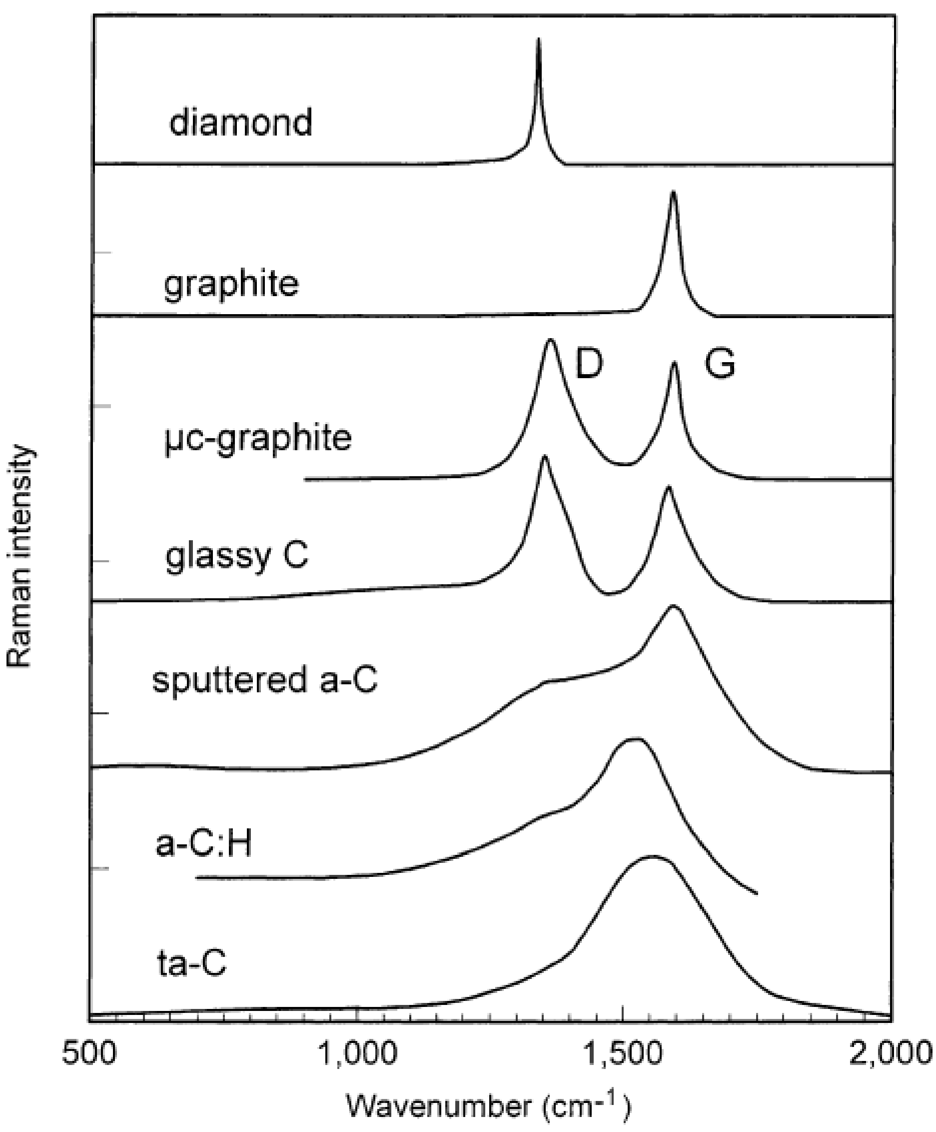

Figure 2.23 Raman spectra of DLC materials [11]

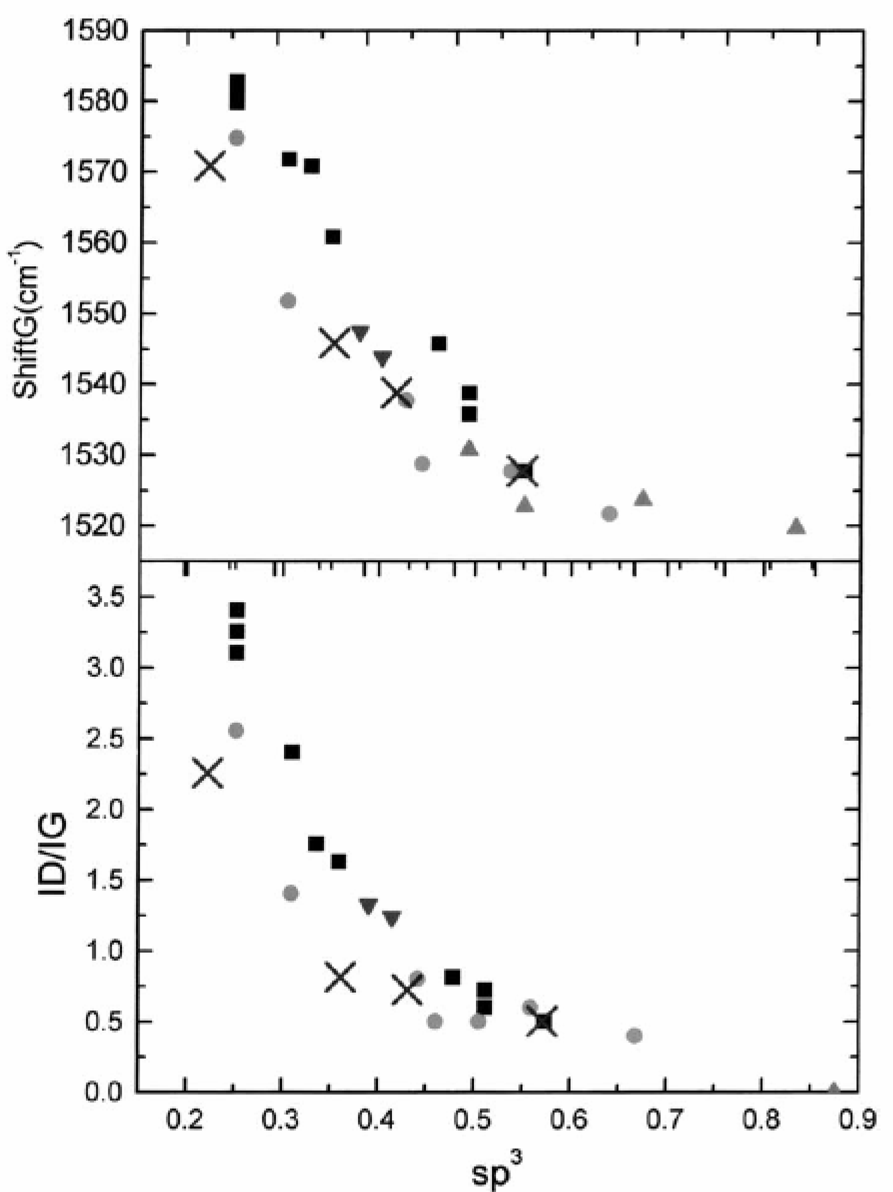

Figure 2.24 sp^3 ratio vs. G peak position and I_D/I_G [55]

	sp^3 (%)	H (%)	Density (g cm^{-3})	Gap (eV)	Hardness (GPa)
Diamond	100	0	3.515	55	100
Graphite	0	0	2.267	0	
C_{60}	0	0		1.6	
Glassy C	0	0	1.3–1.55	0.01	3
Evaporated C	0	0	1.9	0.4–0.7	3
Sputtered C	5	0	2.2	0.5	
ta-C	80–88	0	3.1	2.5	80
a-C:H hard	40	30–40	1.6–2.2	1.1–1.7	10–20
a-C:H soft	60	40–50	1.2–1.6	1.7–4	<10
ta-C:H	70	30	2.4	2.0–2.5	50
Polyethylene	100	67	0.92	6	0.01

Table 2.1 Comparison of major properties of amorphous carbons with those of reference materials diamond, graphite, C_{60} and polyethylene [11]

Parameter	Berkovich	Cube-corner	Cone	Spherical	Vickers
Shape					
C-f angle	65.35°	35.264°	—	—	68°
Projected Contact area	$24.5600d^2$	$2.5981d^2$	πa^2	πa^2	$24.5044d^2$

Table 2.2 Different indenter tips [8]

CHAPTER 3

EXPERIMENTAL SETUP

3.1 Specimen design

The dog bone shape membrane was designed to have a larger center area which could minimize the stress concentration. The tapered regions that attach to the wafer and the long gauge length were designed to minimize boundary-bending effects. Different sizes of membrane specimens were designed to study the size effects on mechanical properties. The different membranes (each type was labeled with a group name) were represented in individual windows of each die, 28 dies per 4 inch wafer. Figure 3.1 shows the die layout of the differently shaped membranes. The membrane dimensions of different group (different sizes) were listed in table 3.1. The window sizes were designed for KOH <100> silicon etching. After the KOH anisotropic etching, the final window edge should be closed to the start point of the tapered region. These two masks were designed by our research group and the mask parameters were improved from formal masks based on the experimental data.

3.2 Wafer/Substrate preparation

The silicon wafers used in this project were p-type <100> direction wafers. The thickness was 500μm ±15μm. Silicon nitride was deposited on both sides of the wafer using LPCVD method. The LPCVD system belongs to Auburn Electrical Engineering

Department. The source gases were dichloro-Silane (SiH_2Cl_2, 140sccm) and Ammonia (NH_3, 30sccm). The deposition temperature was 850 °C and the pressure was around 420 mtorr. It took 90 min to deposit 300nm silicon nitride on both sides of the wafer.

3.3 NFC deposition

All the NFC films were grown at Argonne National Laboratory using the modified Perkin-Elmer 2400 RF PECVD [45]. Figure 3.2a and 3.2b show a schematic of the system and the CVD chamber, respectively. The PECVD chamber allows eight 4 inch wafers to be processed at one single time. In PECVD mode, the flow rate of the precursor gases was limited to a maximum of 60 sccm. All substrates were pre-sputtered with Argon plasma using RF powers between 900-1100W for cleaning purpose. The pre-sputtering time ranged from 5 to 15 minutes depending on the process requirement. The base pressure prior to deposition was $3x10^{-7}$ torr, while the deposition pressure was 20-24 mtorr. The self bias voltage applied was -375V~-425V. This bias was higher than the voltage (-100V) mentioned in literature review that gives the highest Young's modulus and density. Actually, different experimental conditions like gas flow rates, sources gas ratio, RF field-plate (FP) power and the chamber volume will cause this bias voltage changing. For our Perkin-Elmer 2400 RF PECVD and the experimental parameters, the optional bias voltage ranges from -375V to -500V.

The source gases for deposition were methane (CH_4) and hydrogen (H_2). As mentioned before, the different ratio between these two gases brings different

properties (structure) of NFC films. Argonne laboratory uses the names in table 3 to label their DLC films with different ratio of source gases. For film NFC6, which were used for this project, has 75% hydrogen (42 sccm flow rate) and 25% methane (14 sccm flow rate) as source gases. The total flow rate should not be over 60 sccm during the whole deposition process. The process was running at Room Temperature. The estimated deposition rate was around 1.85nm/min, so it took about 9 hours to grow a 1μm NFC6 film. The NFC6 films with different thicknesses (150nm, 460nm, and 900nm) were deposited for the experiments. The sp^2 fraction of the NFC6 film was determined as 70% ± 2% from previous work by Mehta [56].

3.4 Micromachining process

As we are the first research group to fabricate freestanding NFC membranes, all the fabrication parameters and procedures were obtained from experiments. Totally, 16 wafers were fabricated, from which both the successful and unsuccessful results were analyzed to improve the experimental parameters and skills. The key issues and difficulties of fabricating NFC freestanding films were discussed in next section. The process flow is shown in figure 3.3.

3.4.1 Wafer cleaning

The wafer was first cleaned with acetone followed by alcohol (30 sec) and rinsed with DI water for 1 minute. Then the wafer was put in an oven to remove surface water vapor (dehydration, 120°C, and 90min). If acetone leftover was found on the surface, the wafer should be immersed in a (5:1:1) solution of H_2O-NH_4OH-H_2O_2 at

50 °C for 10 min.

3.4.2 Bottom side PR patterning

The wafer was put in HMDS chamber to increase the adhesion of photoresist on the surface (HMDS type: HP-primer, 5 min). The *AZ 5214-EIR* positive photoresist was then spincoated on top side of the wafer with a speed of 3000 RPM for 30 sec, which had a thickness of 1μm. The top side PR worked as a mask layer for NFC films during Si_3N_4 plasma etching. The PR was softbaked at 115 °C for 1 min.. After cooling down, the wafer was patterned with the bottom window mask (figure 3.4) and exposed for 6 sec. The exposed PR was developed with a solution (2:1) of DI wafer and AZ 400K developer for 18 sec. The wafer was then hardbaked at 140 °C for 1min. This process raised the PR strength to effectively resist the plasma ion bombardment.

3.4.3 Bottom-Side Si_3N_4 etching

The bottom side silicon nitride was etched in window shape using “matrix” plasma etching system. The mask for plasma etching was the photoresist. The source gases were 40% N_2, 40% NF_3, and 20% O_2. The pressure was 1 torr and the RF power was 130w. The etching temperature was 100 °C and the etching rate was 100nm/min. The whole etching process took 4-5 rounds. The first round took 2 min, which was experimentally determined to remove 300nm thick silicon nitride. The following 3-4 rounds took 10 seconds each to etch the residual Si_3N_4. The residual silicon nitride would largely increase the KOH etching time of silicon substrate. As most of the Si_3N_4 was gone, the window surface should be in grey color (the color of silicon substrate). However, a microscope was still needed to tell whether all the Si_3N_4 was

gone or not. The etching time should be strictly controlled to avoid ion-bombarding etching of silicon substrate.

3.4.4 Top side PR patterning

The residual PR on both sides of the wafer was removed using ultrasonic method (acetone, 3~5 min). The cleaning procedure mentioned above was re-did before patterning. Then the top side of the wafer was patterned with the membrane mask shown in figure 3.5. To align the top and bottom feature, two bottom microscopes of the mask aligner were used to take images of the alignment marker on the mask. Then the wafer with top side pattern was inserted into the machine to align with the marker images. The process should be achieved carefully. Failing to do that might cause the shift of the bottom windows. After exposing for 7 seconds, the wafer was immersed in the develop solution for 20 sec. Then the wafer was dried with nitrogen gas and hard baked for 1 min.

3.4.5 Cr sputtering

A thin chromium layer was deposited on top side of the wafer working as the mask for DLC etching. The sputtering system is located in the clean room of materials engineering (figure 3.6). The wafer is pre-sputtered with a DC power of 150 watts for 2 min. Then it was sputtered with chromium target at the same DC power for 10 min. The substrate holder was rotated at a speed of 50 RPM to perform a uniform deposition. The estimated deposition rate was 25nm/min, so the Cr film thickness was around 250nm. Detailed sputtering parameters are shown in table 3.3.

3.4.6 Lift-off process

Figure 3.7a shows a normal process for obtaining features from thin film on the substrate. The film is first deposited on the substrate, which is selectively patterned with photoresist as s mask material. The etching process removes the uncovered part of the film to obtain certain structures. On the contrary, in a lift-off process, photoresist is first patterned on the substrate, and then the target film is deposited on the surface to form a structure showing in figure 3.7b. Any material deposited on PR will be removed with the resist and leave the patterned material on the substrate. Using a lift-off could bring a better feature of the patterned thin film, but the mask dark/light fields design should be opposite to that for normal "subtractive" process or switching from positive photoresist to negative ones. In our project, the top mask was designed typically for lift-off process and the photoresist used was positive.

The sputtered wafer was immersed in a beaker with acetone. Then the beaker was put in an ultrasonic vibration bath for lift-off process. For this Cr lift-off, two rounds of ultrasonic vibration were applied, each of which lasted 3 minutes. After first round, the acetone solution with large amount of Cr should be replaced with fresh one, so that the adhesion of residual Cr particles on the wafer surface could be avoided.

3.4.7 O_2 reactive ion etching (RIE) of NFC films

The NFC etching was performed with Advanced Oxygen Etching (AOE) system, which can provide a strong directional (anisotropic) plasma etching. The 4-inch wafer was mounted on a 5-inch silicon substrate with wafer gripper to fit the 5 inch holder for AOE. The wafer gripper could provide a good thermal conduction between the

holding substrate and the target wafer, so that "burnt" phenomenon could be avoided. The etching method selected was typically for diamond and diamond like materials. The source gas was oxygen with a flow rate of 30 sccm. The RF power to Coil was set to 600 watts and the bias voltage was set at 100V. A 30 sec process followed by eight to eleven 5 sec processes could etch through the NFC film. The plasma also had an effect on silicon nitride and chromium due to the ion bombardment. It was wise to possibly shorten the whole etching time and check the thickness of the DLC film after each round. Experientially, the etching should stop when the etching rate was less than 1 nm/sec. Figure 3.8 shows the AOE system located in E&E clean room at Auburn University.

3.4.8 KOH etching

The etching of the silicon substrate was performed in a specific KOH etching system. The wafer was clamped in a Teflon holder, where only the back side of the wafer is exposed to the KOH. The solution is a mixture (9:25:1) of 45% (w.t. %) KOH, DI water, and propanol. Propanol or alcohol was used to prevent water from evaporation. The beaker with KOH and wafer holder was immersed in a water bath, where the temperature was heated to 60°C. A water-reflow system was placed above the beaker to condense the water vapor and kept the concentration of the KOH solution stable. The stir rate in the beaker was 100rpm and the etching rate was close to 25µm/hour. It took 20 hours to etch through the 500µm thick silicon substrate. Figure 3.9 shows the KOH system located in materials clean room.

3.4.9 Cr etching

The residual chromium on the wafer can prevent the NFC film touching the KOH wafer holder directly. It was the reason that the Cr was removed after KOH etching. The Cr etchant was CRE-473, which had an etching rate about 20-50nm/sec. It took less than 15 seconds to remove all the residual Cr and the etchant had minor effect on silicon nitride and NFC films. After etching, the wafer was rinsed with DI water for 1min and dried with nitrogen gas.

3.4.10 Top-side Si_3N_4 etching

The top side silicon nitride was etched with either dry (plasma) or wet (hot phosphoric acid) method. For plasma etching, the source gases were 75%N_2+20%NF_3 +5%O_2. The pressure was around 1.5 torr and the RF power was set to 90w. The etching temperature was 60 °C. It took 30-40 rounds (each round lasted 5 sec) to etch through the silicon nitride. For wet etching, the etching rate of hot Phosphoric acid was 4.5 nm/min at 155 °C. It took 66 minutes to etch through a 300nm thick top-side silicon nitride. Experientially, the 150nm, 460nm and 900nm thick NFC freestanding membranes were obtained from plasma etching. The etching process was also affected by the properties of the silicon nitride.

3.5 Membrane deflection experiment (MDE)

The DLC wafer was cut into small dies for MDE tests. The die was put on to the interferometer stage with a slot. The light was green light with a wavelength of 545nm. First, the x and y knobs of the interferometer were used to locate the window.

Then the z knob was used to focus on the back side of the membrane. Then the rotating knobs were used to align the membrane with interferometer until X-directional fringes were eliminated and even Y-directional fringes were obtained on both sides. Four air tests were done before the real MDE in order to obtain a stable and accurate air effect baseline. The displacement and load information were recorded by the nanoindenter. The fringes changes were recorded by interferometer, which were used for strain calculation.

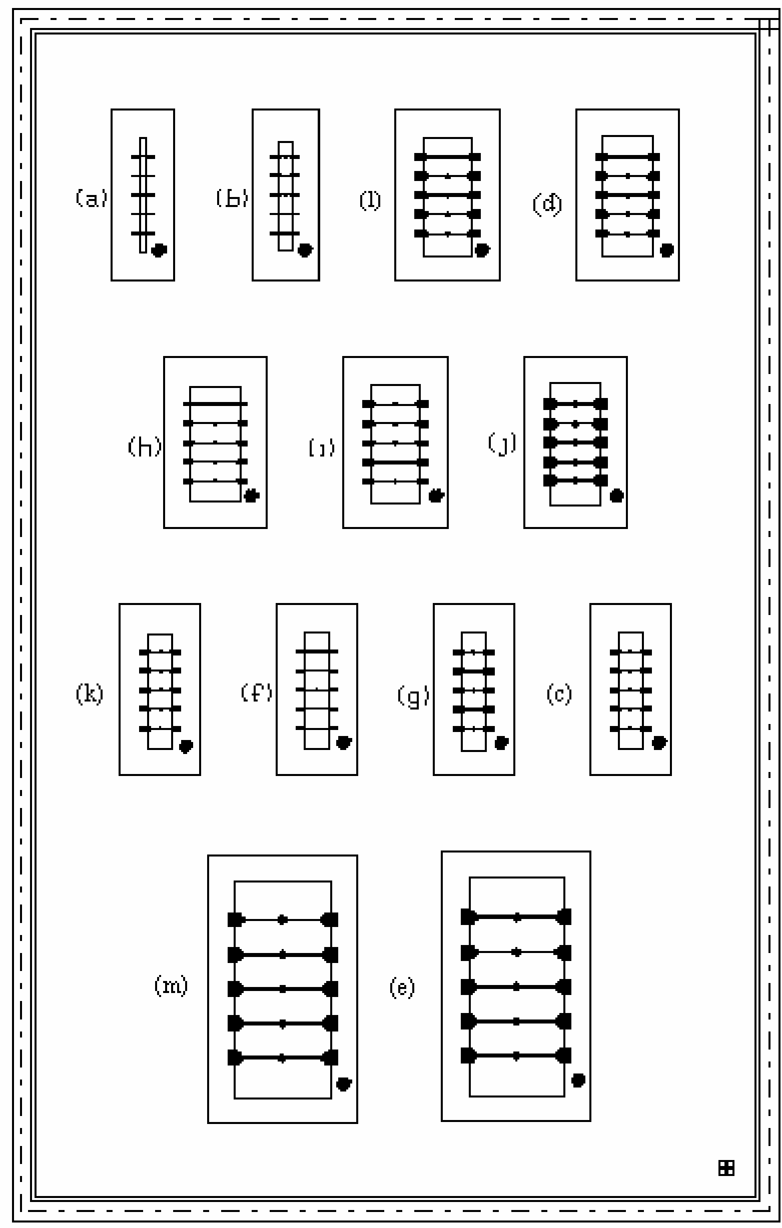

Figure 3.1 Die schematic for NFC freestanding membranes

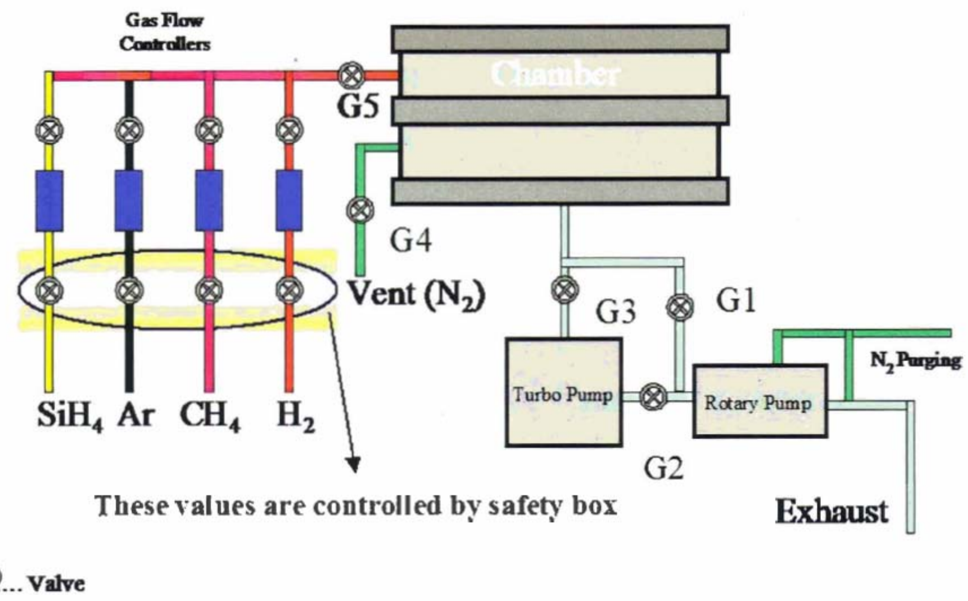

Figure 3.2a Schematic of the RF PECVD system at Argonne National Lab

Courtesy of Argonne National Lab

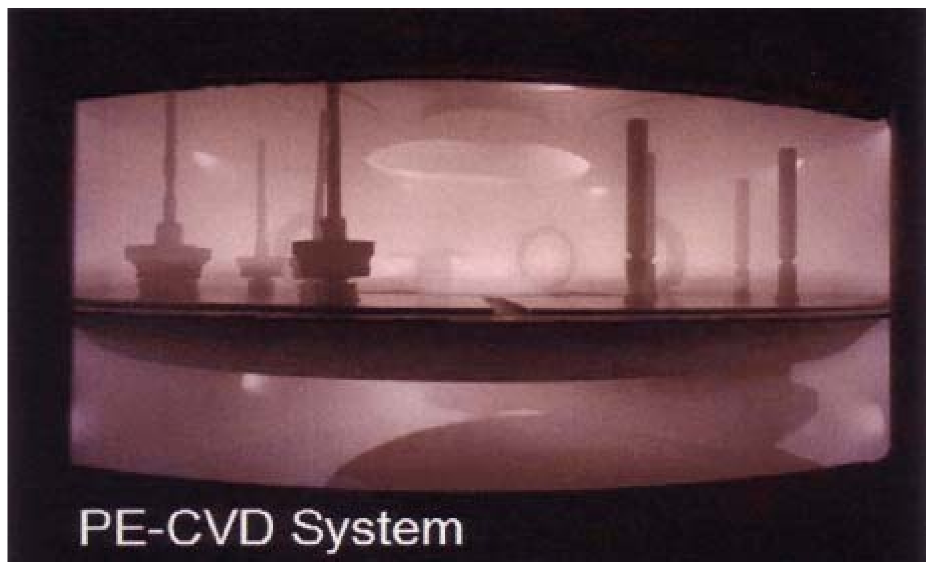

Figure 3.2b Image of the PECVD chamber at Argonne National Lab

Courtesy of Argonne National Lab

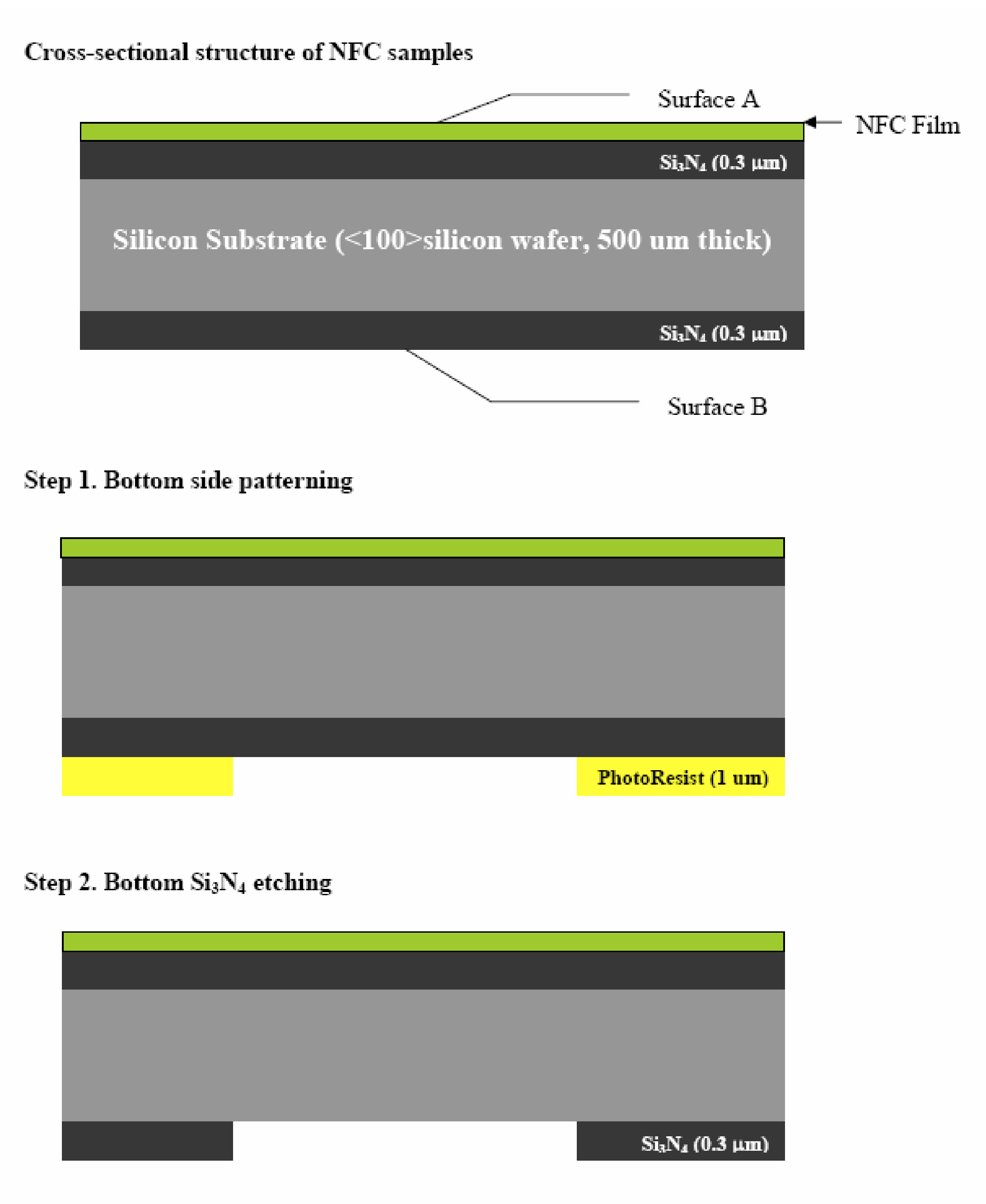

Figure 3.3 NFC membrane fabrication process flow

Step 3. Top side patterning

Step 4. Sputter Cr

Cr.

Step 5. Lift-off

Step 6. AOE etching

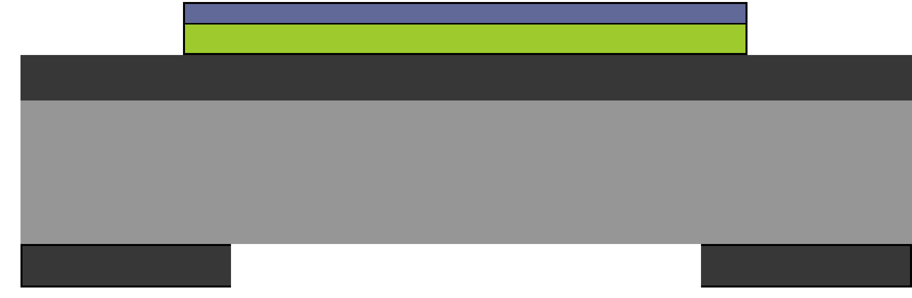

Figure 3.3 NFC membrane fabrication process flow (cont.)

Step 7. KOH etching and remove Cr

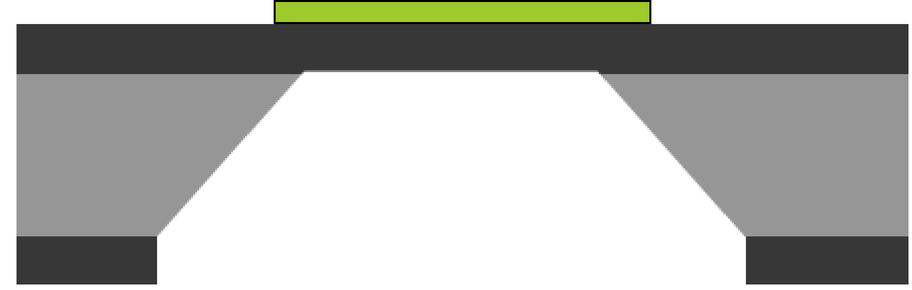

Step 8. Top side Si_3N_4 etching

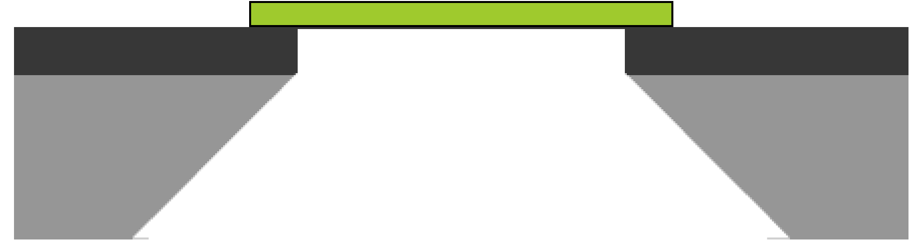

Figure 3.3 NFC membrane fabrication process flow (cont.)

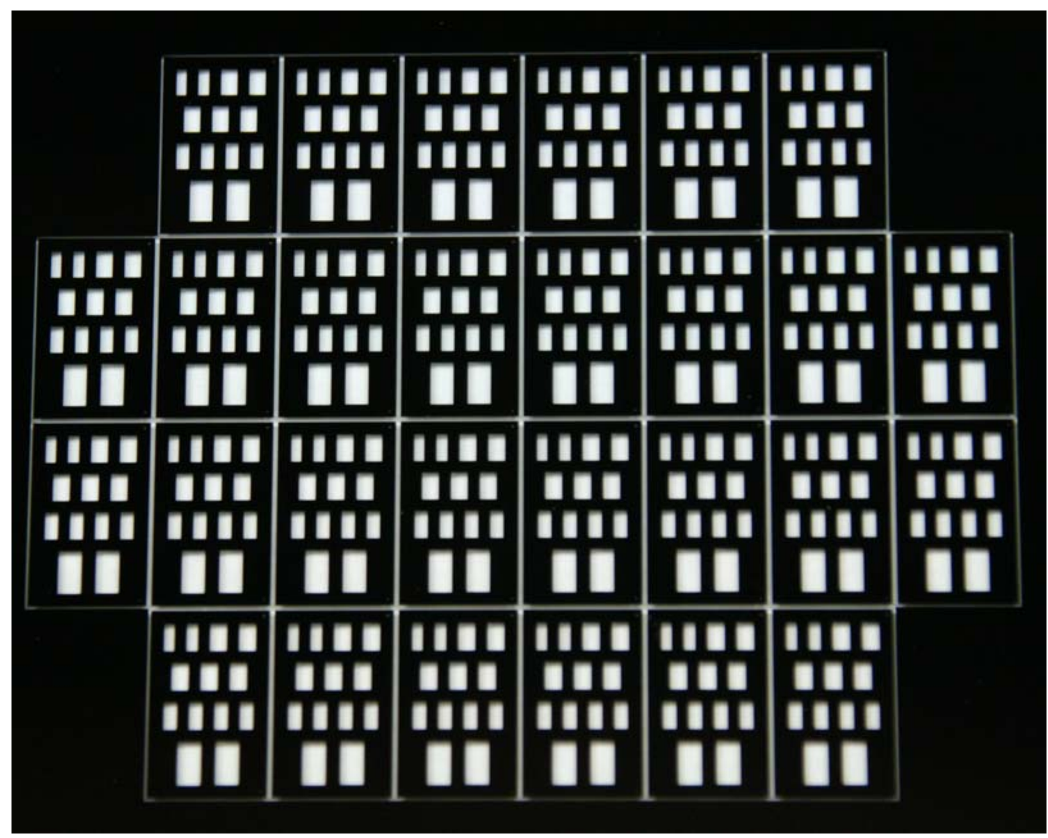

Figure 3.4 Image of the bottom window mask

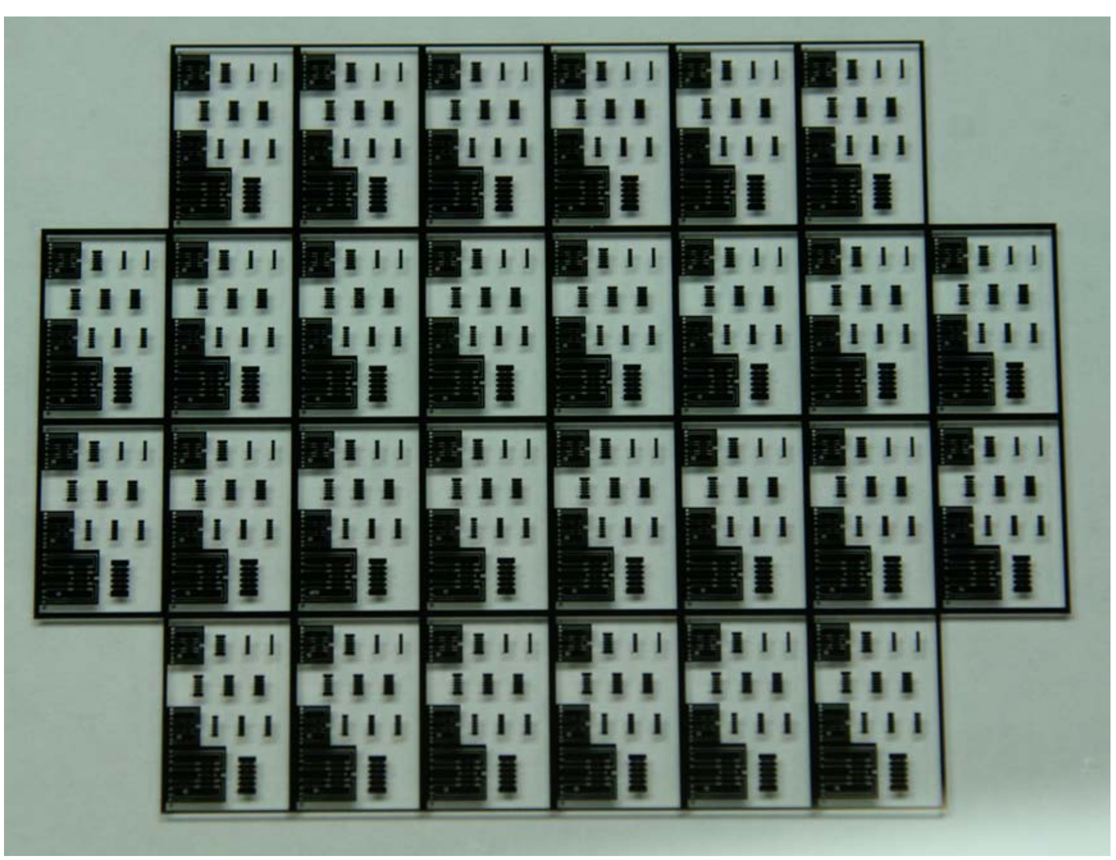

Figure 3.5 Image of the top membrane mask

Figure 3.6 Image of the sputtering system

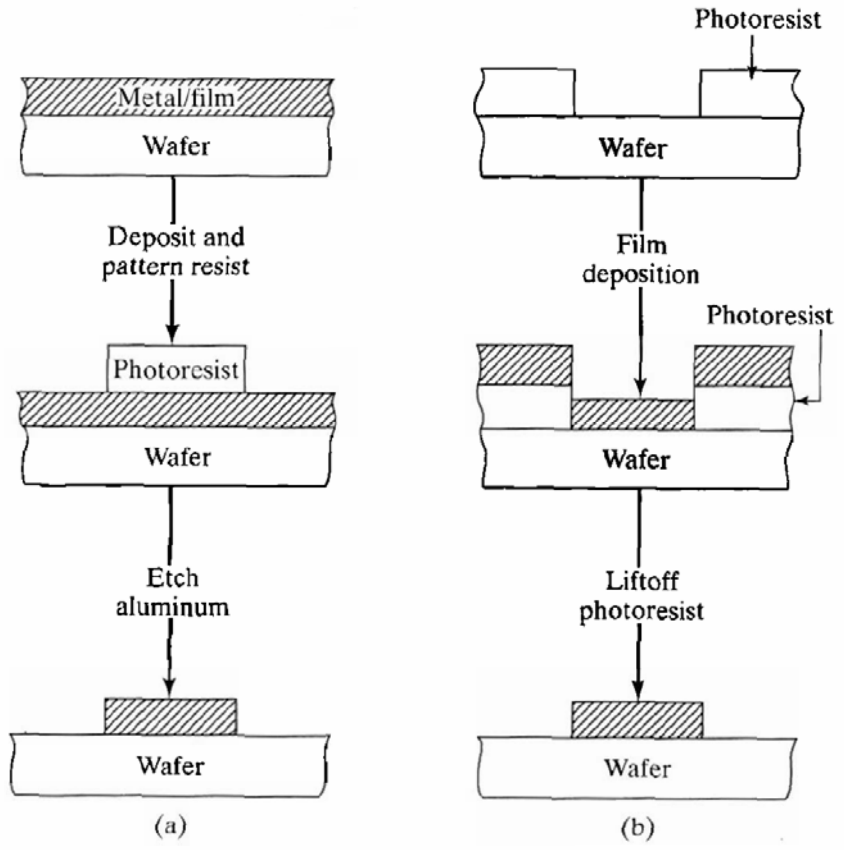

Figure 3.7a and 3.7b Subtractive and lift-off processes [40]

Figure 3.8 Image of the AOE system

Figure 3.9 Image of the KOH system

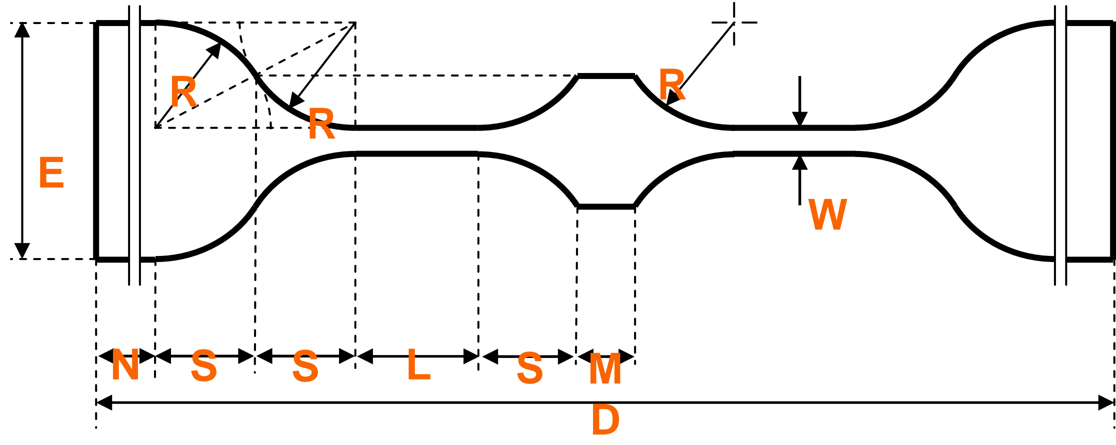

Sample	Dimensions (μm)						
	W	L	L/W	D	E	R	N
Group a	1.25	25	20	286.7	11.25	5	100
Group b	2.5	50	20	361.9	22.5	10	100
Group c	5	100	20	513.8	45	20	100
Group d	10	200	20	817.9	90	40	100
Group e	20	400	20	1424	180	80	100
Group f	2.5	126	50	513.9	22.5	10	100
Group g	7.5	74	10	514	67.5	30	100
Group h	5	252	50	817.8	45	20	100
Group I	7.5	226	30	818	67.5	30	100
Group j	15	148	10	818	135	60	100
Group k	5	100	20	513.8	45	20	100
Group l	10	200	20	817.9	90	40	100
Group m	20	400	20	1424	180	80	100

Table 3.1 Membrane dimensions for different sized specimens

a-C:H film	Source Gases
NFC2	50% H_2, 50% CH_4
NFC6	75% H_2, 25% CH_4
NFC7	100% CH_4
NFC8	25% H_2, 75% CH_4

Table 3.2 Argonne NFC films and their source gases

Sputtering Power	DC
Target	Chromium
Substrate	a-C:H with photoresist
Base Pressure	5×10^{-6} torr
Pre-sputtering Time	120 sec
Pre-sputtering power	150 watts
Sputtering Time	600 sec
Sputtering Power	150 w
Gas 1 flow (Argon)	25 sccm
Deposition Temperature	Room Temperature
Substrate Holder Rotate	50%
Ignition Pressure	70 mtorr
Deposition Pressure	5.2 mtorr

Table 3.3 Sputtering Parameters

CHAPTER 4

RESULTS AND DISCUSSIONS

4.1 Key issues in micromachining NFC freestanding films

4.1.1 Robust mask for NFC etching

At the beginning of the project, copper was selected as the mask material for NFC etching due to its inexpensive price and easiness to sputter. However, after the residual copper was removed by the copper etchant, the NFC film was found seriously damaged. Figure 4.1a shows the membrane feature after copper was etched. A typical copper etchant was a (16:3:4) solution of DI H_2O-H_2SO_4-H_2O_2. It turned out that the sulfuric acid (H_2SO_4) also etched the NFC film during the Cu etching process. Chromium, as another good material for sputtering, was then selected as the mask material. Figure 4.1b shows a good and clean membrane feature after the residual Cr was removed. The Cr etchant consisted of (16:3:4) DI H_2O, CH_3COOH, and H_2O_2. The organic acetic acid (CH_3COOH) is a much weaker acid than the sulfuric acid. It had little reaction with the NFC film during the Cr etching. Figure 4.2 shows the image of the top side of the wafer after Cr etching.

4.1.2 Oxygen RIE etching of NFC films

The method used to etch the NFC films was oxygen reactive ion etching (RIE). The SEM image in figure 4.3a indicates there was a notching underneath the film after the plasma etching. This phenomenon was caused by the surface charging during

RIE etching. As the NFC film was etched through, the positive ions from the plasma would accumulate on the substrate surface due to the poor charge relaxation and a lack of neutralization by electrons [57]. This would build a positive potential that distorted the coming ions to the end of the sidewall and finally caused localized etching underneath the film (Figure 4.3b [57]). To avoid serious notching, the NFC etching time was strictly controlled. The whole process was splited into 9-12 rounds of etching, each of which lasted 5 seconds to reduce the surface charging effect.

4.1.3 KOH bulk micromachining of Si substrate

As mentioned earlier, potassium hydroxide (KOH) performed an anisotropic etching on silicon substrate. It opened a cavity on <100> direction wafer, which had an angle of 54.74° of the sidewall. In our project, the silicon was etched from the wafer backside windows. The final widths of the windows were exactly the length of membrane. Figure 4.4 shows the schematic of the final window size (width) compared to the membrane. Although the KOH etching rate of Si_3N_4 was about 1000 times slower than that of Si, the KOH might still attack the silicon nitride in some local area. Figure 4.5 shows the backside silicon nitride condition of the two dies etched with different KOH concentration and temperature. The left die was etched at 60 °C with a 28% KOH solution, while the right one was etched at 80 °C with a 33% KOH solution. It was found that a solution with higher temperature and KOH concentration would do more damage to our silicon nitride layer.

4.1.4 Top Si_3N_4 layer etching

The top side silicon nitride could be etched with either dry or wet method, but both of them had pros and cons. Hot phosphoric acid (H_3PO_4) was often used for wet silicon nitride etching. The etching temperature ranged from 154 °C to 180°C (154°C is the boiling temperature of H_3PO_4). The etching solution consisted of 85% class 10 H_3PO_4 and some content of DI water. Water vaporized at 100°C, which was lower than the operation temperature. So during the process, DI water should be kept adding to the solution (or use the water reflow system mentioned in KOH etching). As the water vaporized, it brought out the heat and kept the solution temperature. If the water was depleted, the temperature of the pure hot phosphoric acid would increase dramatically in a short time, which was not good for the samples. The beaker was always put in an oil bath which was heated and stabilized at 154°C. The NFC film had a very clean surface after H_3PO_4 etching shown in Figure 4.6a. However, during the etching process, many bubbles were created. These bubbles kept the samples (usually small dies) flowing up and down in the solution and caused some of the membranes twisting (figure 4.6b). Also DLC materials would start to crystallize as temperature was above 150°C, which would slightly change the mechanical properties of NFC6 films. These two disadvantages forced us to use plasma etching for the top side silicon nitride.

Dry Plasma etching was also a method to etch the silicon nitride. The whole etching process was slow and "mild" to reduce the damage of the NFC films from O ions. The disadvantage was that the die surface would not be as clean as that from wet

etching (Figure 4.7a). The residual silicon nitride on back side of the membrane was difficult to be removed, which might affect the mechanical properties obtained from MDE tests. Figure 4.7b shows the freestanding NFC membranes obtained from plasma etching.

4.2 Profilometer and Raman characterization

The profilometer was used before top silicon nitride etching to determine the exact thickness of the DLC films. From the profilometer, the thicknesses of NFC6 films are measured as 0.15μm, 0.46μm, 0.9 μm.

The Raman spectra of NFC6 films with different thickness are shown in Figure 4.8. The spectra indicated uniform positions of D and G peaks, which meant the NFC films had similar bonding structures. The G mode was at 1594 cm^{-1}, while the D mode was around 1366 cm^{-1}. The extra peaks in the figures were laser plasma peaks, which were caused by laser beam going directly into the detector.

4.3 AFM characterization

Atomic Force Microscope (AFM) was applied to measure the topography of the NFC sample. Figure 4.9, 4.10, and 4.11 indicate the surface situation of three different thicknesses of NFC films. The RMS roughness values of NFC films ranged from 5.36 nm to 7.86 nm. The NFC roughness largely depended on the surface conditions of Si_3N_4/substrate. Due to the different Si_3N_4 roughness, the NFC films topographies might vary a little. The 3D AFM image showed that all the film were

uniform and smooth. Also the size of the clusters (10nm) strongly indicated the amorphous properties of the NFC6 films.

4.4 SEM characterization and MDE results

Due to the different coefficient of thermal expansion (CTE) between Si_3N_4 and NFC, the NFC membranes bent down in some content after the topside Si_3N_4 etching. It was necessary to characterize each membrane's shape with SEM before the MDE tests. Figure 4.12 indicates the bending shapes of the group G membranes from the 460nm NFC6 film.

The interferometer images of the bending membranes were taken to show the original fringes. The image pixel length (such as 2μm per pixel) obtained from SEM figures could help determine the exact distances between two adjacent dark fringes. Those distances were used to calculate the original length of the membrane. The membrane profile could help determine the touching point (Δc beneath the wafer surface) of the MDE tests when a nanoindenter started to touch the membrane. Also, the membrane length would suggest the starting point of the stress-strain curve where pure tension was applied (Δs beneath the wafer surface). Schematic of Δc and Δs is shown in figure 4.13a.

All the testing membranes are profiled before MDE test. Figure 4.14 shows the original fringes and the profile of one group J membrane from the 900nm NFC6 film. As the vertical distance between two dark fringes gave half of the green light wave length, Δc was calculated from:

$$\Delta c = \frac{\lambda}{2} * (\frac{fringe\#}{2} - 1) \quad (15)$$

Here “fringe#” was the total dark fringe number over the membrane before MDE test. Membrane length (L_M’) was obtained using triangle simulation from the membrane X-Y profile. Therefore, Δs was given by:

$$\Delta s = \sqrt{(\frac{L_M^{'}}{2})^2 - (\frac{L_M}{2})^2} \quad (16)$$

Here, L_M was the horizontal width of the final window.

4.5 Data reduction

The MDE raw displacement-load plot of one group J membrane (150nm NFC) is shown in figure 4.15a. As the MDE test was load controlled, the raw load data was set as the x axis value. The straight line belonged to the air test result. The small triangle deviation belonged to the real MDE test. The real load should be the raw load minus the load from air effect. From the figure, the breaking point can be determined. In an ideal situation, as the nanoindenter touches the membrane, the real load (stress) applied on the membrane should start from zero. Based on our method, the breaking point (labeled as 4) was suggested from the real load datasheet where a sudden drop of the values was observed. Then the touching point (labeled as 2) was determined from the interferometer images (these fringes image can tell the total time from touching to break). From the touching point, Δc was applied to find the surface position of the NFC film (labeled as 1). At this point, the displacement was normalized and the stress and strain started to be calculated. The real

load-displacement plot of the same membrane starting from point 1 is shown in figure 4.15b. Finally, from the surface position, a point 3 with a displacement of Δs was found to start the stress-strain curve (where pure tension started). Due to the equation (12), the membrane should already have a positive strain as the nanoindenter tip touched the membrane. That meant the stress strain curve would cut the positive X axis and intersect Y axis with a negative value. The stress-strain curves of bending down NFC membranes are different from previous work of Prorok [50], in which the UNCD membrane was buckled up (Figure 4.13b) and the stress-strain curve intersected Y with a positive value.

4.6 Young's modulus of the NFC6 film

The Young's modulus of NFC films measured from 45 membranes ranged from 32 GPa to 38 GPa. The average (arithmetic mean) value was 35.13 GPa. The standard deviation was 2.292 GPa. Figure 4.16 (abc), 4.17 (abc), and 4.18 (abc) indicate the stress-strain curves of NFC membranes with different thicknesses and sizes. Each plot has 5 stress-strain curves for the membranes with same thickness and size. 15 membranes were tested for each NFC thickness. All the NFC films were also tested with the static and CSM nanoindentation methods. The Poisson's ratio was assumed as 0.3. Figure 4.19 shows a load-displacement plot of the 900nm NFC sample using the static method, from which the indent depth was controlled as 1/10 of the film thickness to avoid serious substrate effect. The Young's modulus obtained from static method was 48~53 GPa. Figure 4.20 shows a group of CSM tests run on the 150nm

NFC surface (each curve represented an indent position that was randomly selected.). The substrate effect could be observed from the trends of those CSM E-d curves that after 15nm the modulus started to increase. From CSM method the Young's modulus was obtained as 56~79 GPa. These values were larger than that from the MDE tests not only because the Si/Si_3N_4 substrate effect. On the surface of the tested NFC films, pile-up phenomena were also observed (Figure 4.21). This would enlarge the contact area and cause the real modulus smaller than the theoretical values mentioned in the literature review part. The NFC Young's modulus obtained from MDE tests was comparable to the data from Sung-Jin Cho's work (57.1 $\pm$ 7.5 GPa using RF PACVD with a bias of -250V) [58].

4.7 Size (Width) effect on fracture strength

Not like the Young's modulus which will not be change in micro-scale, the fracture stress of NFC films is largely affected by the size of the membrane. Figure 4.22 indicates the width effect on the fracture stress of the 900nm NFC film (Group G, J, and E). From the figures, one can tell that the fracture stress increases with decreasing membrane width (W) in table 3.1. The amorphous NFC6 films act like ceramic materials where little plastic deformation occurs during tension. For these materials, the flaws existing in the film dominate the fracture strength. A wider membrane might have more flaws in it, which raises the probability to be broken. In other words, more flaws lower the fracture strength. The fracture strength ranging from 0.12 GPa to 0.90 GPa was obtained from the data of 45 membranes. The fracture

strength might also be affected by the membrane edge shape shown in figure 4.3a. The "zigzag" edge causes stress concentration in local areas (at crack tips), which would lower the fracture strength.

4.8 Thickness effect on fracture strength and residual stress

Thickness effect was also obvious on fracture strength. Figure 4.23 indicates the fracture strength increases with decreasing thickness of the NFC films (Group E). Three membranes of the same groups were selected for each plot to give an average view. The mechanism is same to the width effect on fracture strength. The thicker the film, the more flaws existed in the material, which lower the fracture stress.

The residual stress was a more uncertain value compared to elastic modulus and fracture stress. It was affected by many factors like the deposition condition, silicon nitride surface condition, topside Si_3N_4 etching parameters, and membrane bending shape. In this project, the residual stresses were found comparable for each wafer (same thickness). But they were affected by the thickness change. The stiffness is proportional to the cube of thickness (d^3, so the thicker the film is, the stiffer the membrane is. A stiffer film is more difficult to bend, which brings a lower residual stress and smaller bending degree Δc (the membranes with same sizes but different thickness). Thus, the residual stress will increase with decreasing thickness. Figure 4.24 indicates this trend on group E membranes of difference thicknesses. The residual stress ranging from 79 MPa to 310 MPa was obtained from the data of 45 membranes.

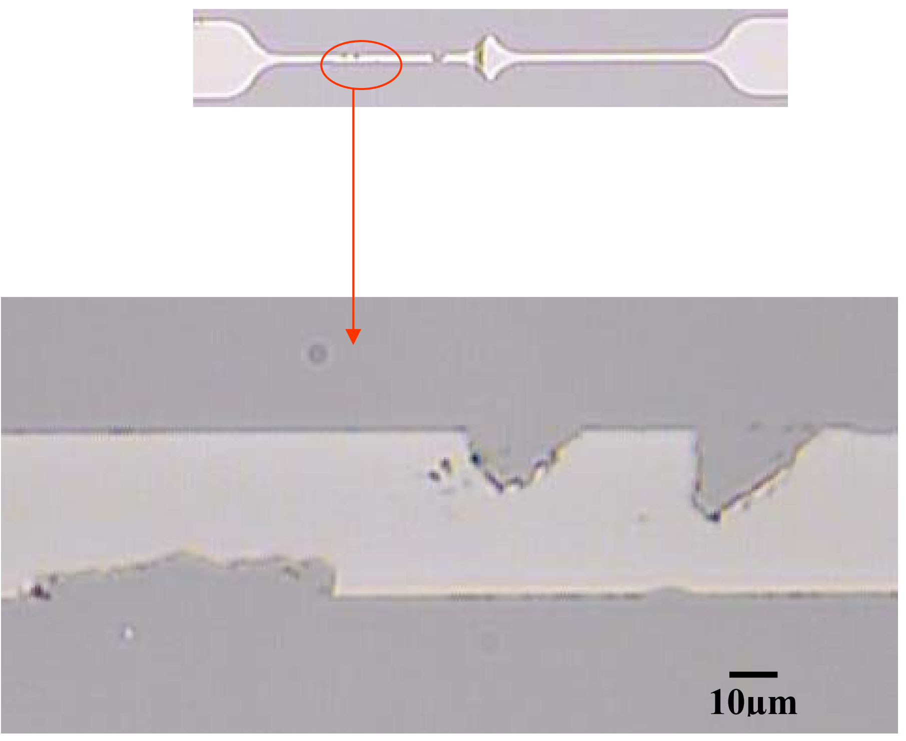

Figure 4.1a NFC membrane feature after Cu was etched

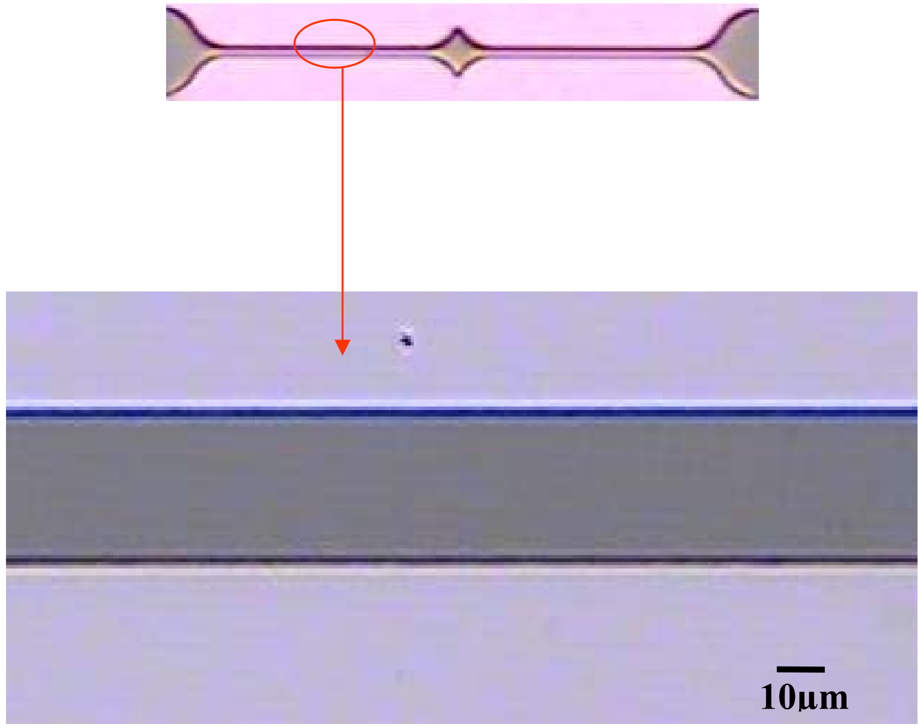

Figure 4.1b NFC membrane feature after Cr was etched

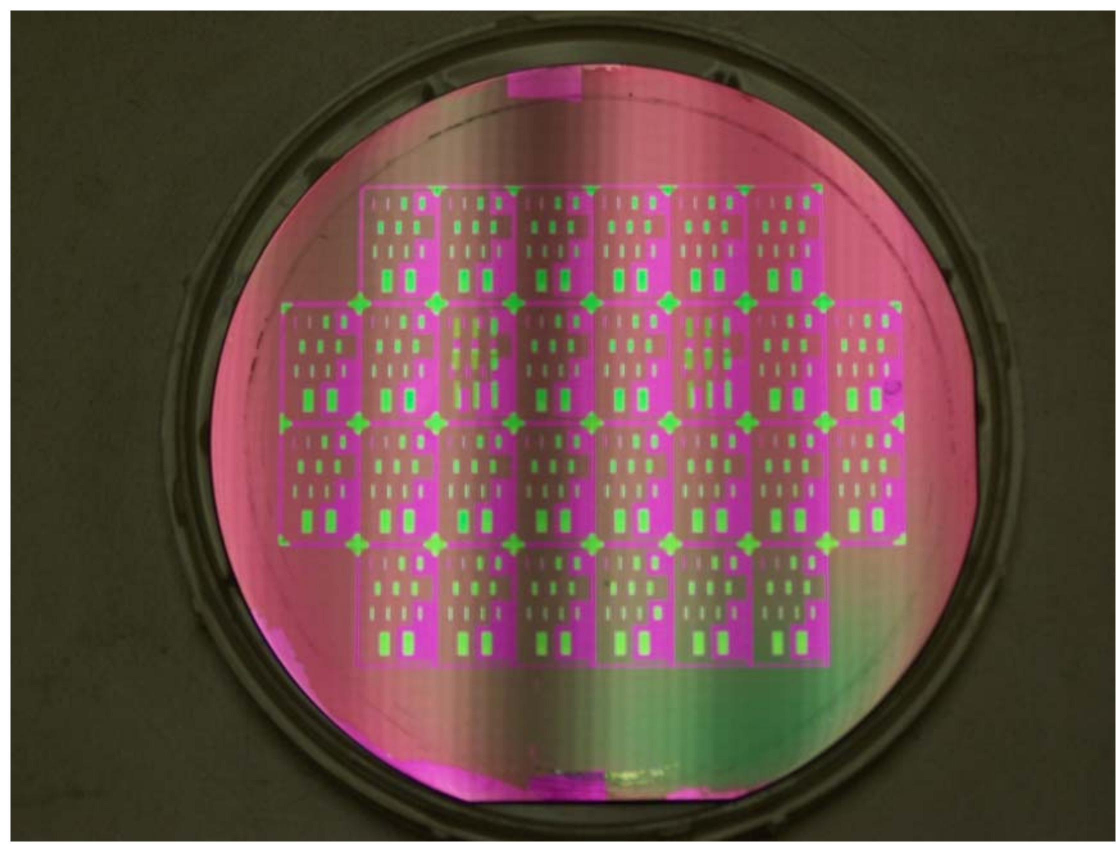

Figure 4.2 Wafer surface after Cr etching. The pink and green colored materials were both silicon nitride but with and without substrate underneath.

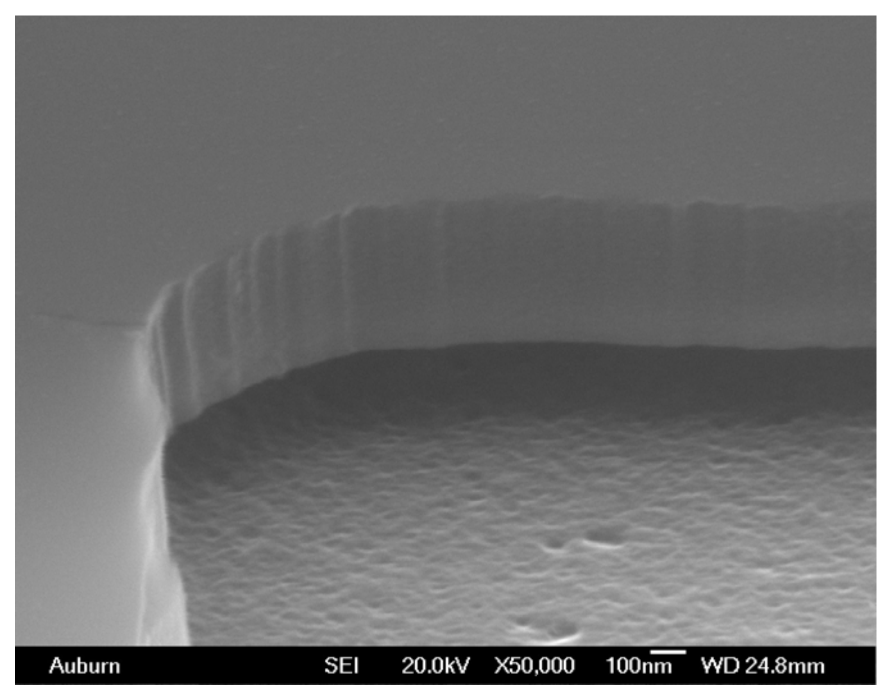

Figure 4.3a SEM image of the notching underneath the NFC film

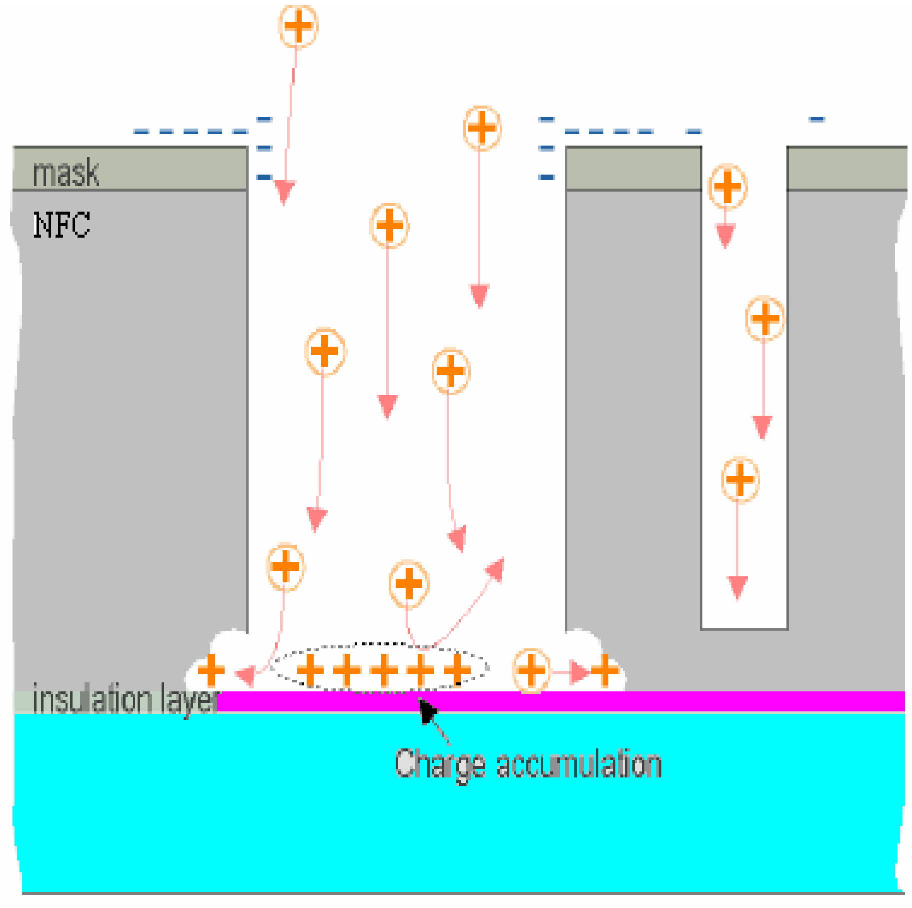

Figure 4.3b Schematic of surface charging during RIE etching [57]

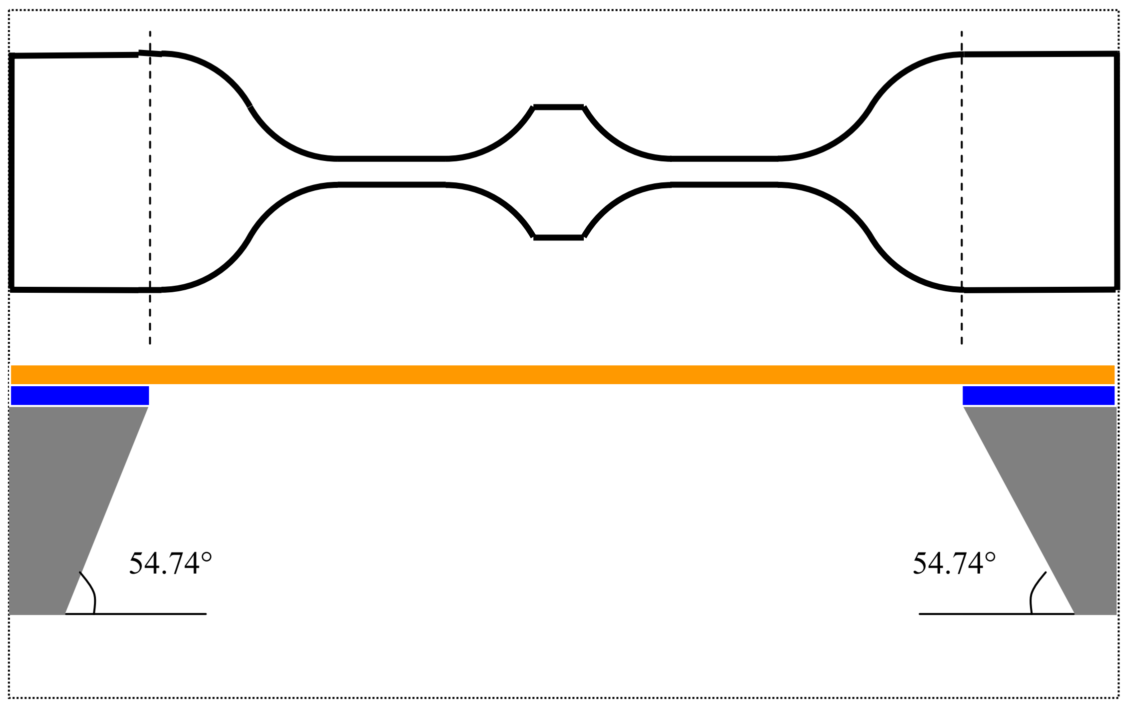

Figure 4.4 Schematic of final window size after KOH etching

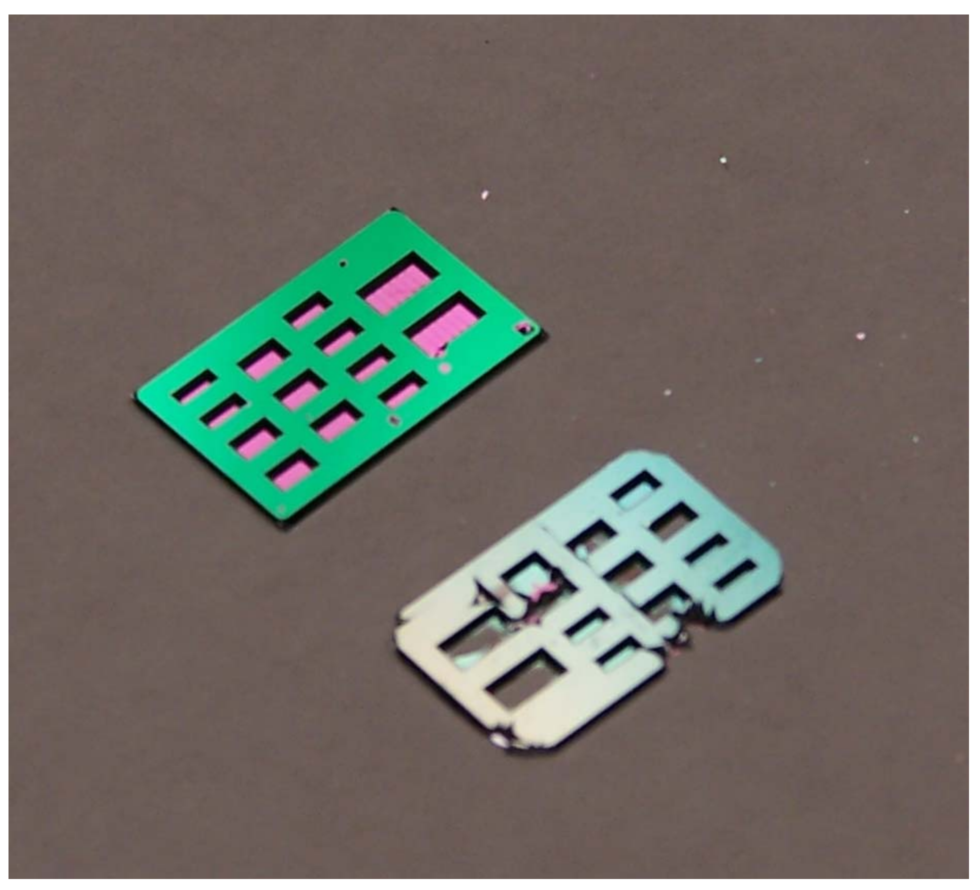

Figure 4.5 Backside views of two dies after KOH etching with different parameters

The left die was etched at 60°C (KOH concentration 28%) and the right die was

etched with KOH at 80°C (KOH concentration 33%).

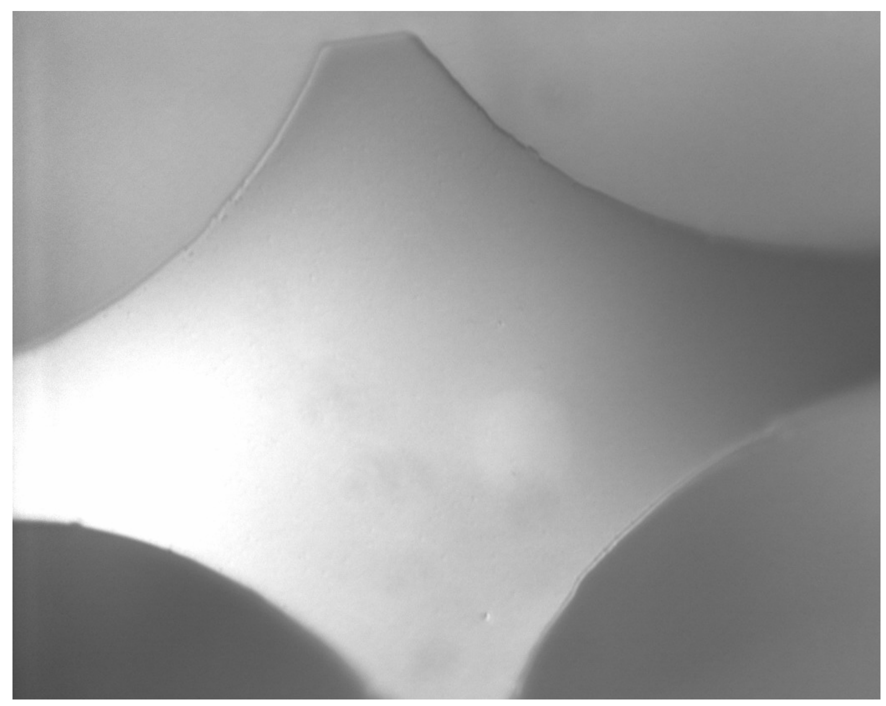

Figure 4.6a Image of the NFC film bottom surface after H_3PO_4 etching

(Nikon Microscope 100x)

Figure 4.6b Image of the membrane twisting during H_3PO_4 etching

(Nikon Microscope 50x)

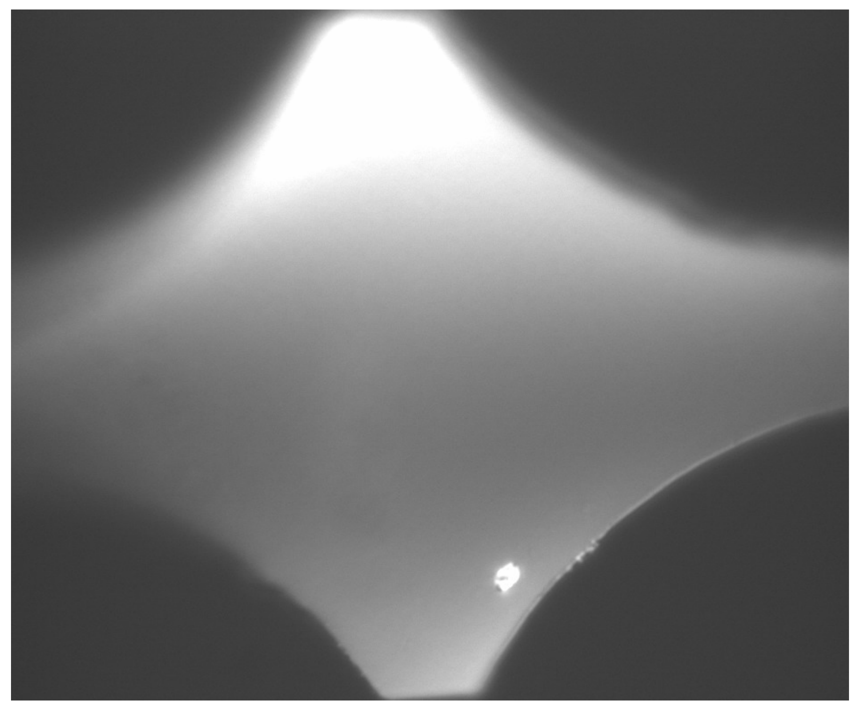

Figure 4.7a Image of the NFC film bottom surface after plasma etching

(Nikon Microscope 100x)

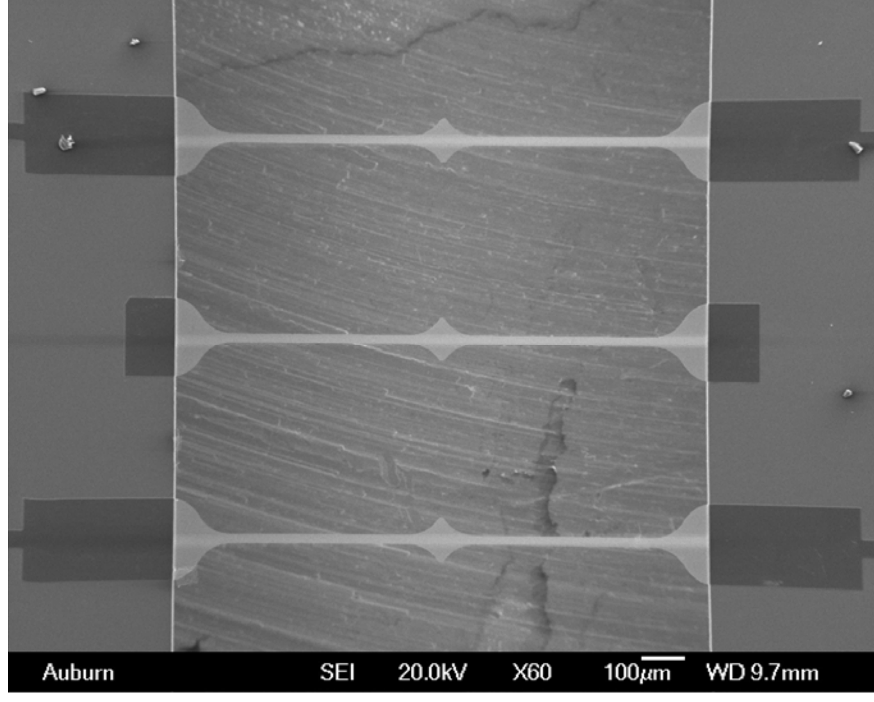

Figure 4.7b SEM image of the freestanding membrane after plasma etching

(460nm NFC6, group E)

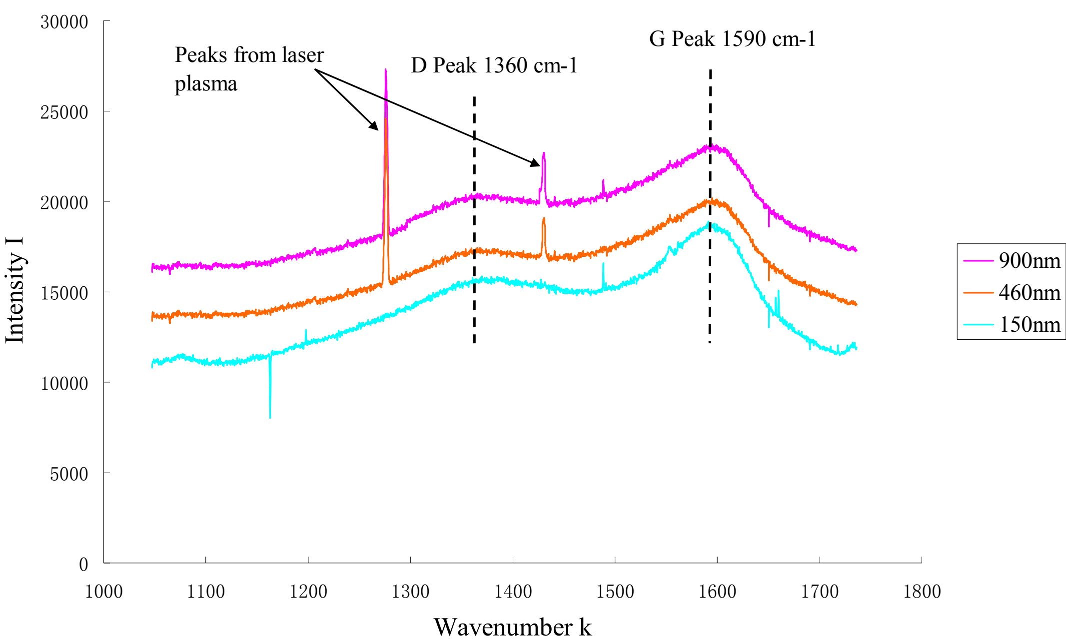

Figure 4.8 Raman spectra of NFC films

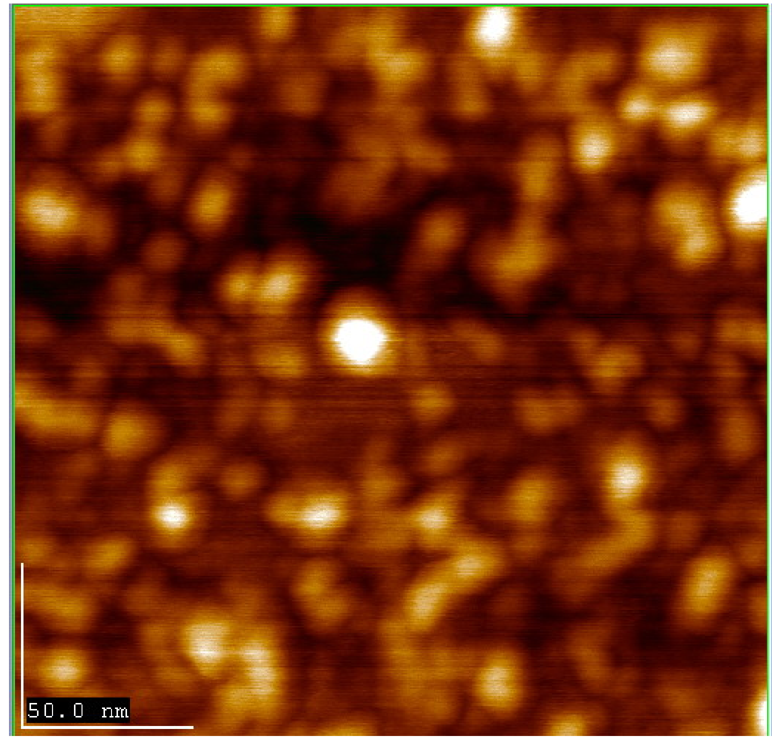

Figure 4.9a 2D AFM image of the 150nm NFC

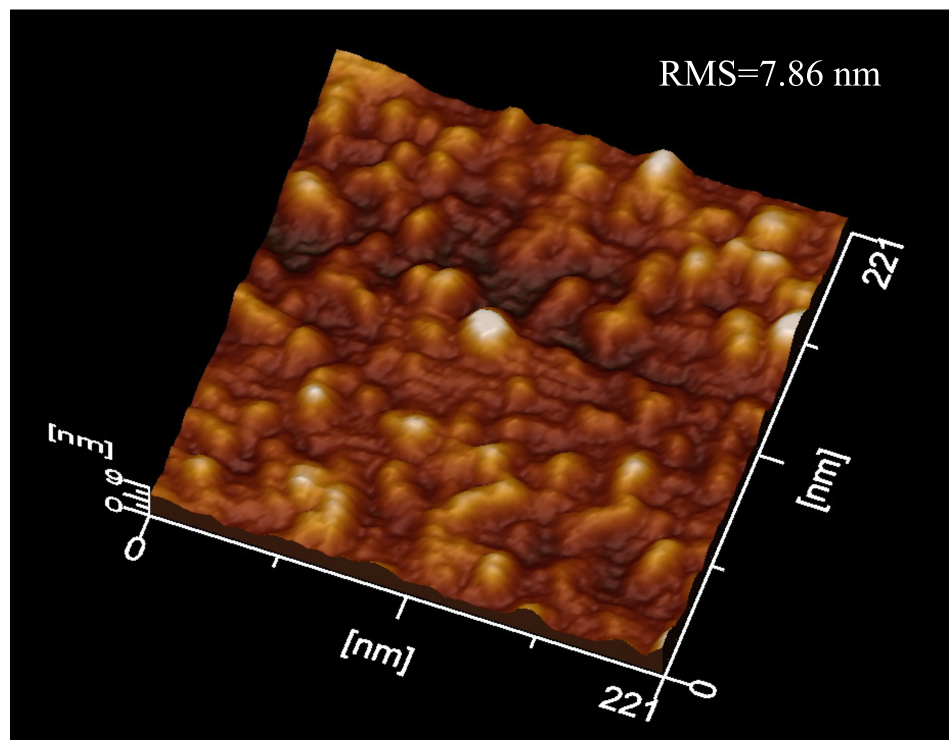

Figure 4.9b 3D AFM image of the 150nm NFC

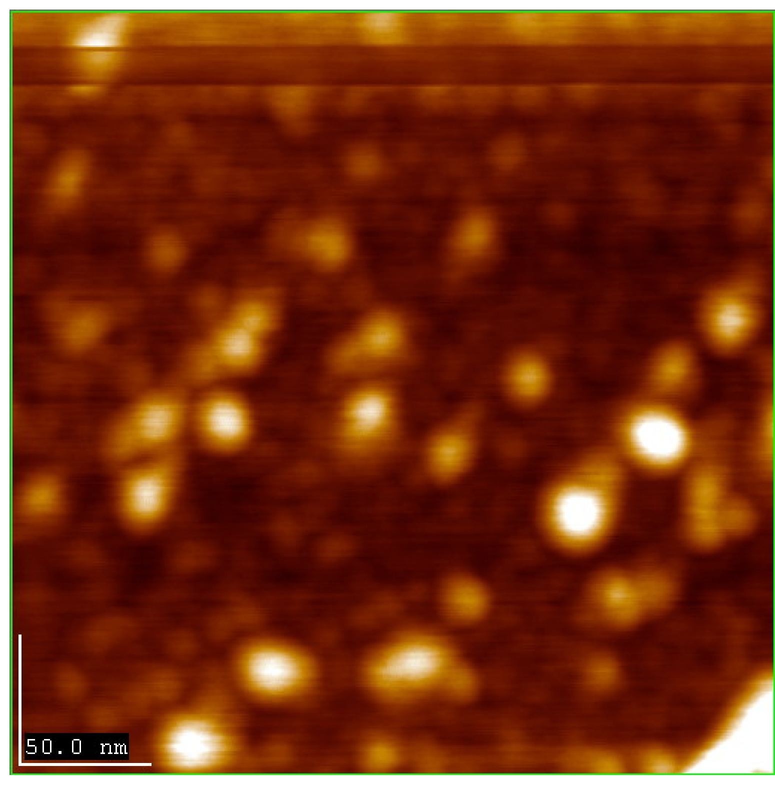

Figure 4.10a 2D AFM image of the 460nm NFC

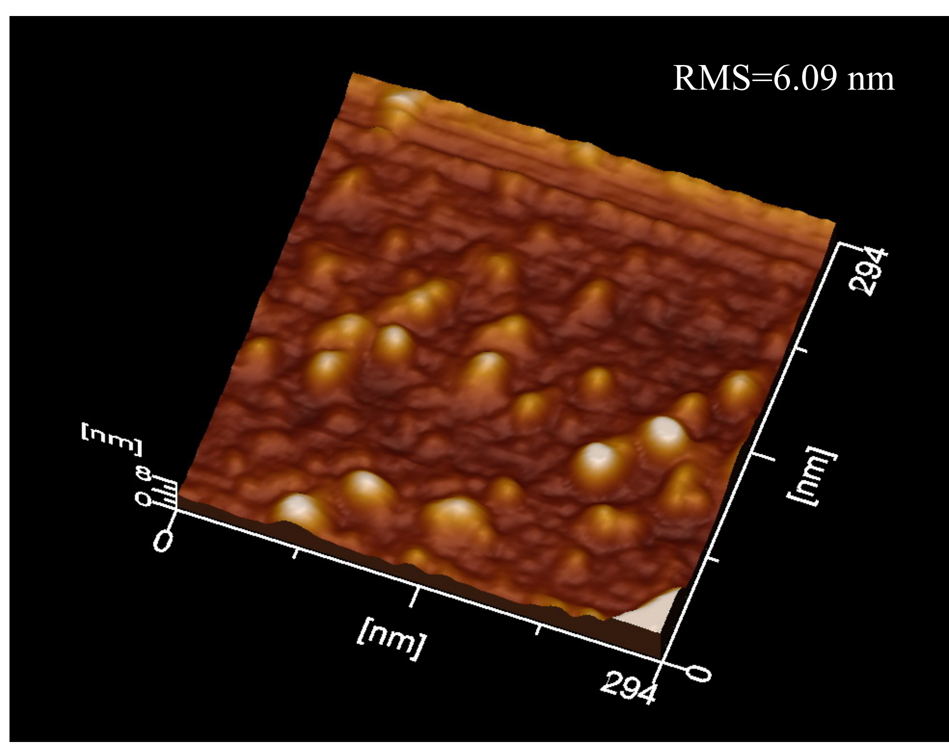

Figure 4.10b 3D AFM image of the 460nm NFC

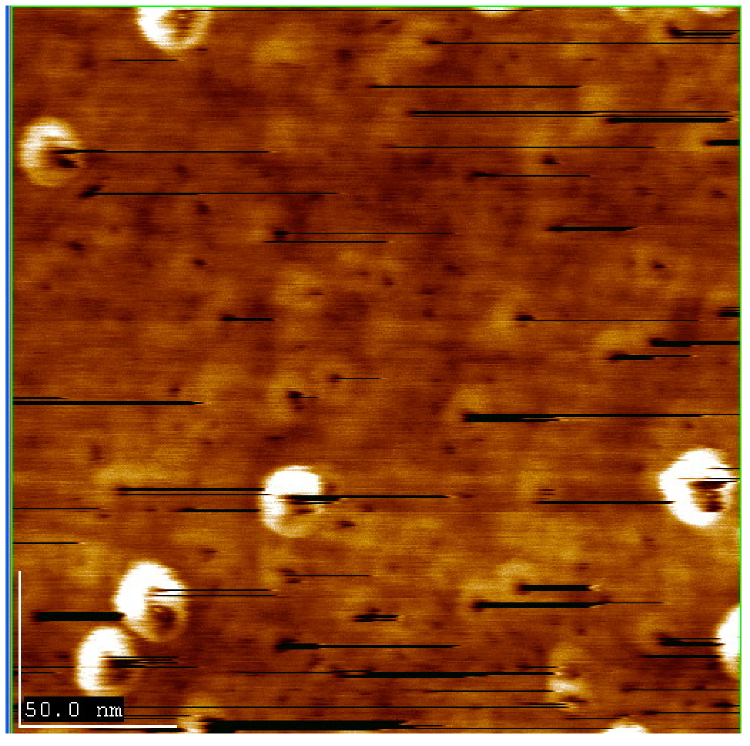

Figure 4.11a 2D AFM image of the 900nm NFC

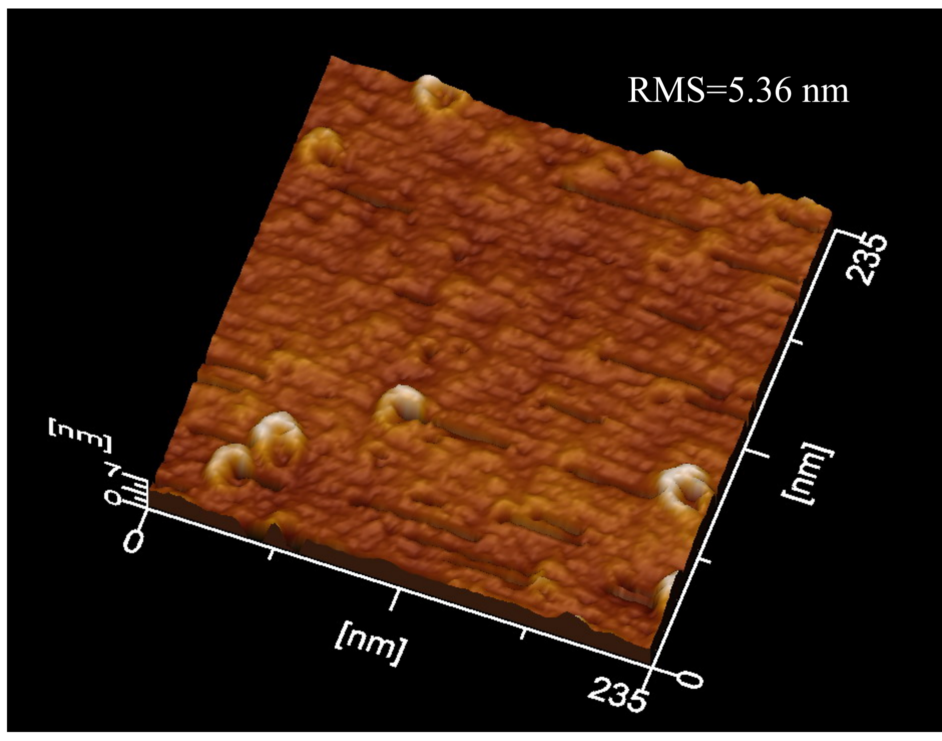

Figure 4.11b 3D AFM image of the 900nm NFC

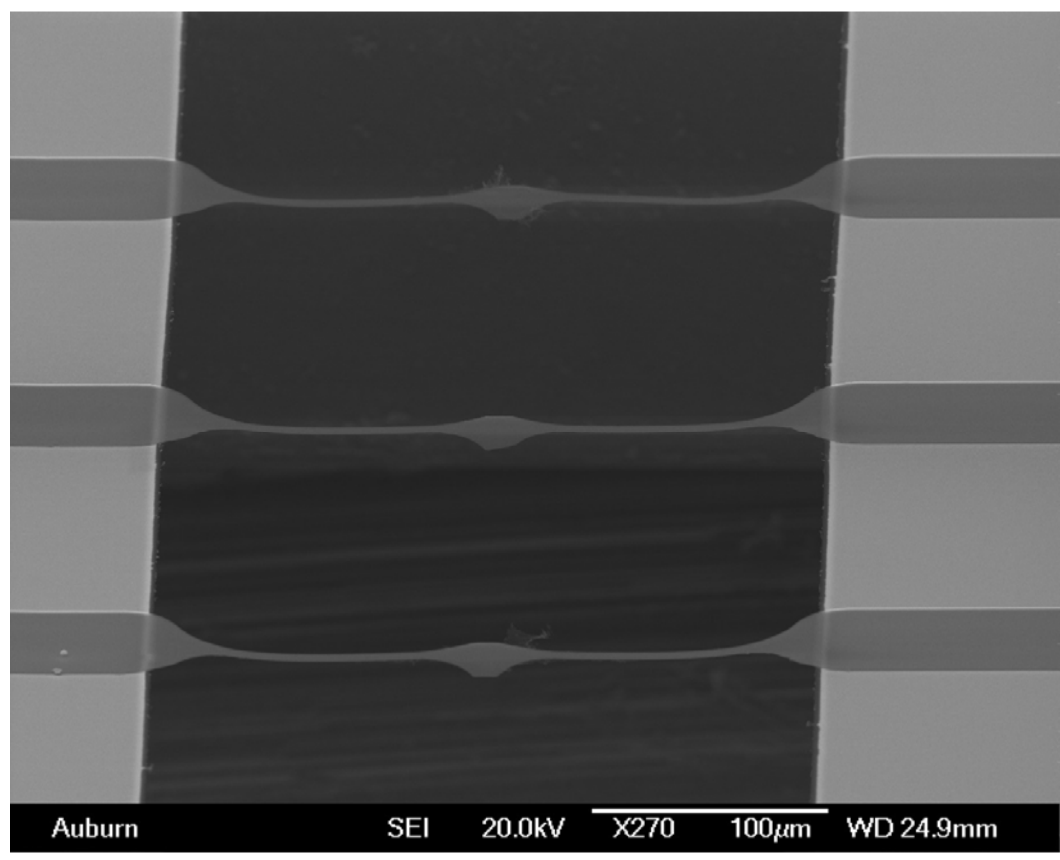

Figure 4.12 SEM image of the group G membranes from the 460nm NFC film

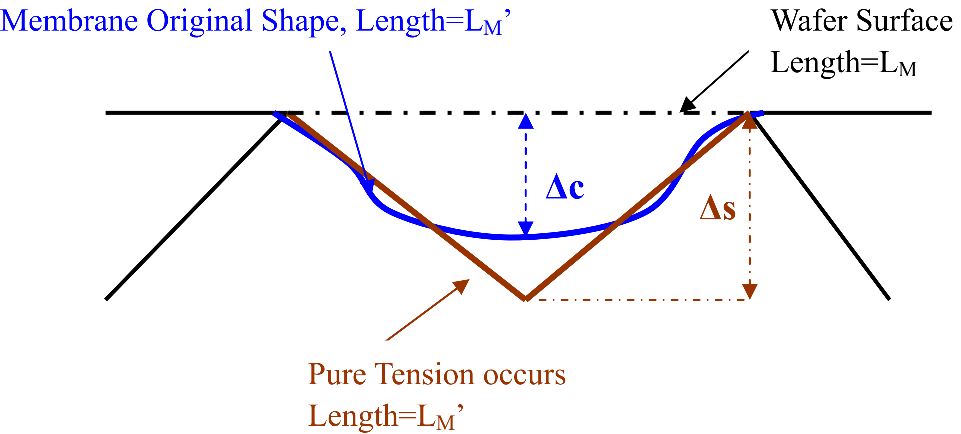

Figure 4.13a NFC membrane bending down situation

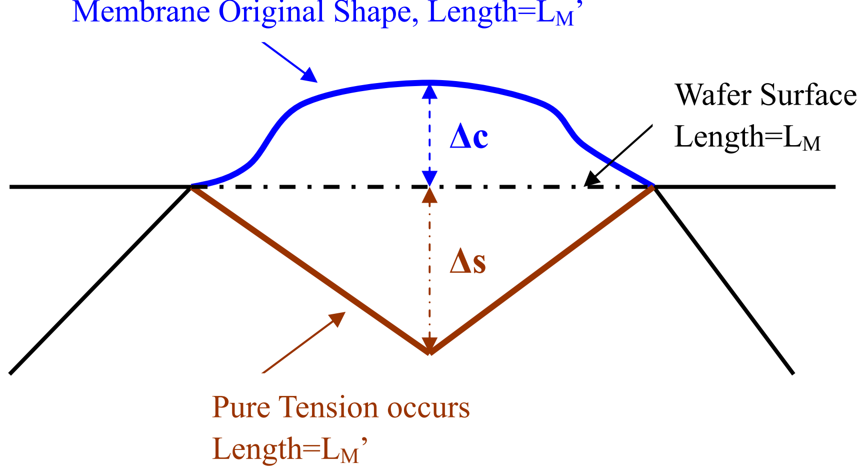

Figure 4.13b UNCD buckling up situation [50]

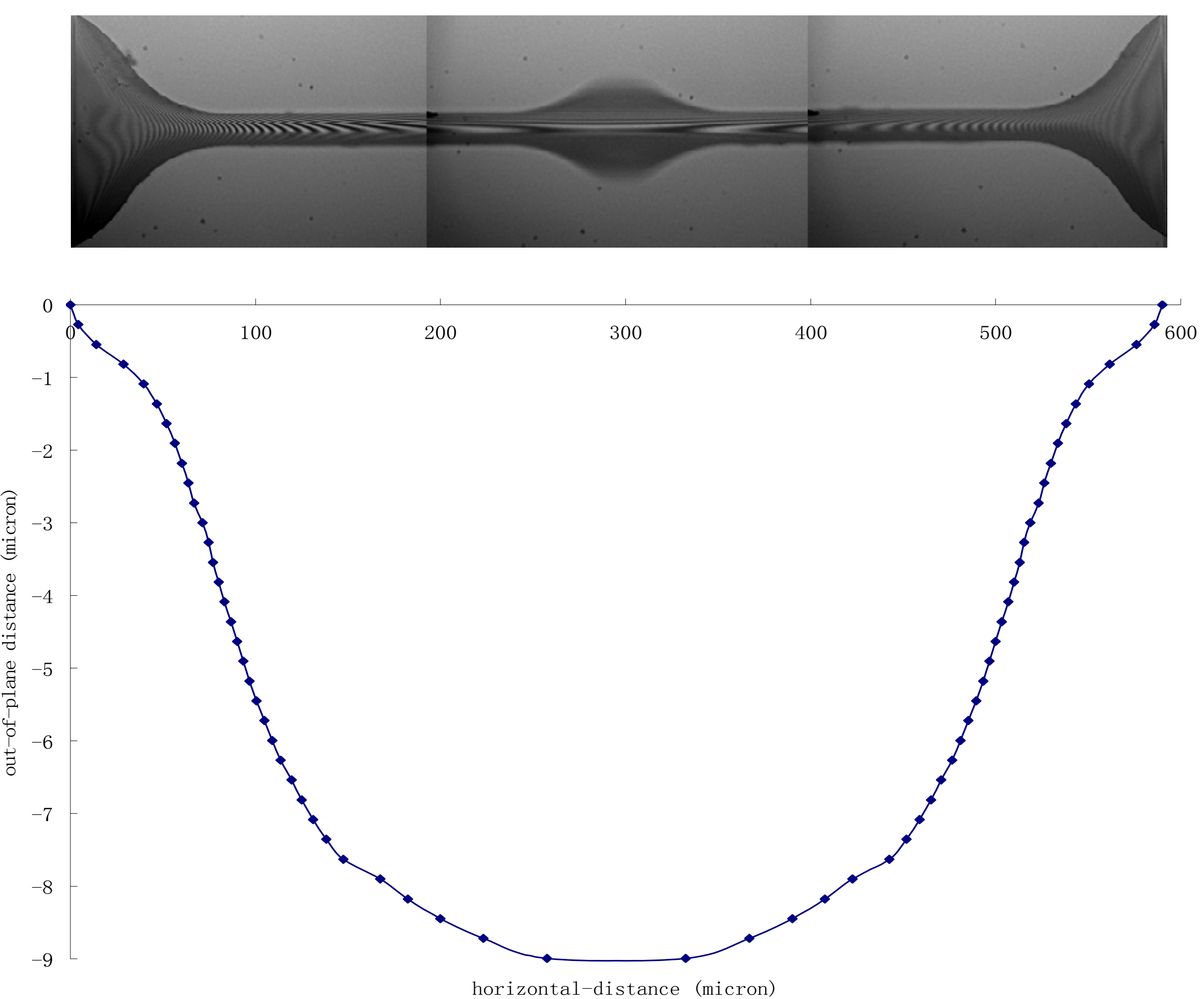

Figure 4.14 Original fringes and profile of the group J membrane (900nm NFC)

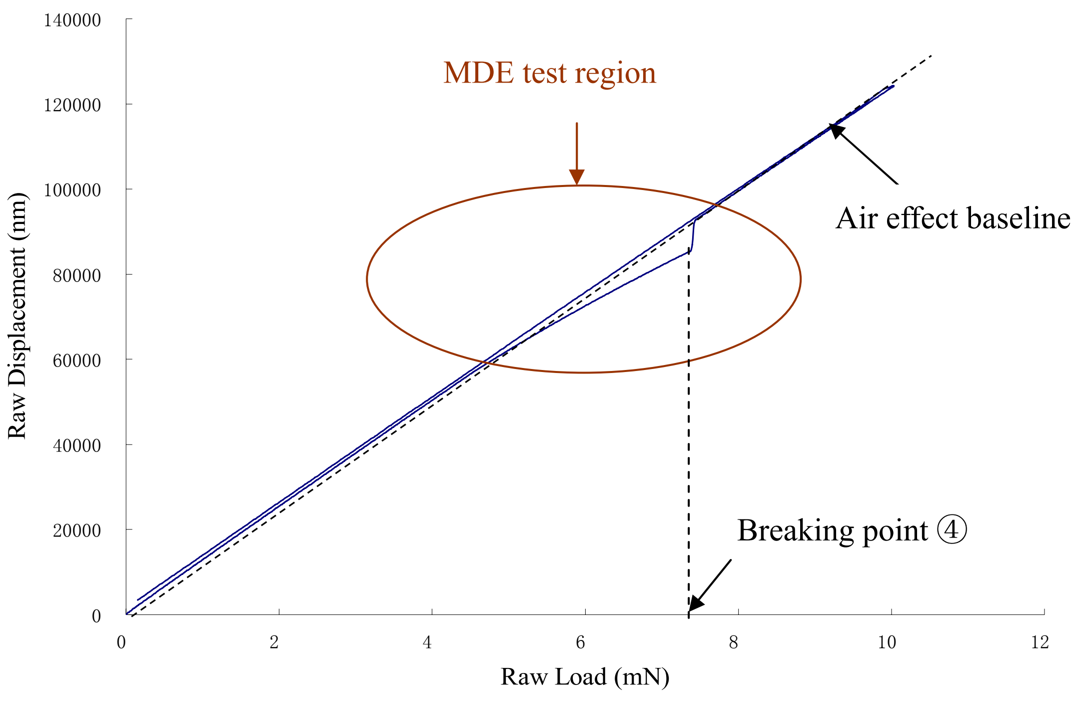

Figure 4.15a Raw displacement-load plot of the group J membrane (150nm NFC)

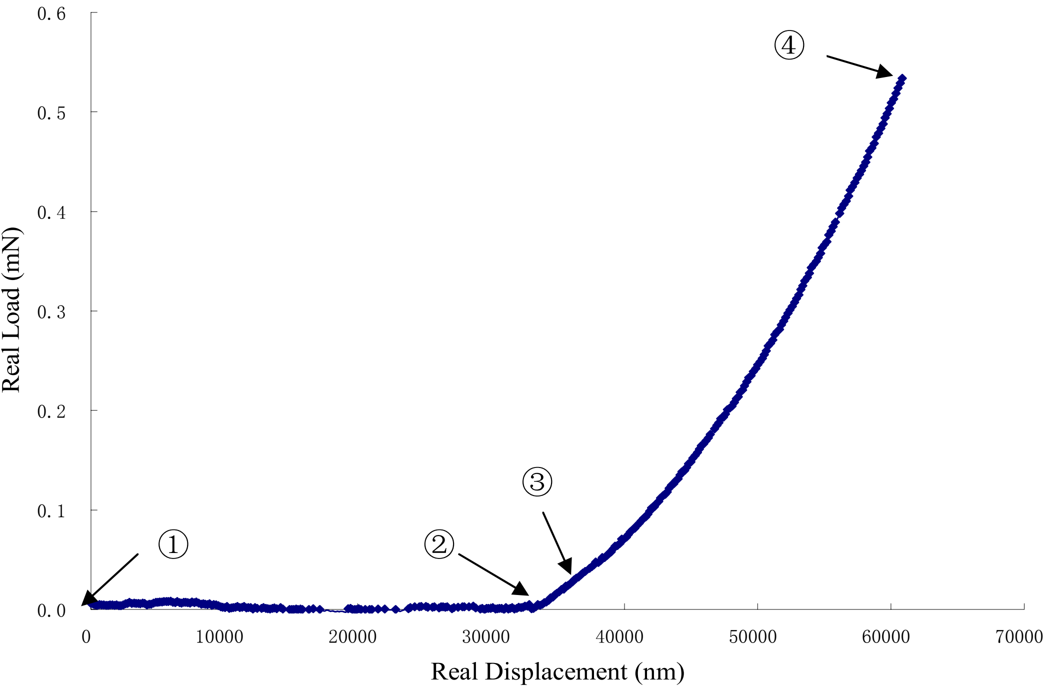

Figure 4.15b Real load-displacement plot of the same J membrane (150nm NFC)

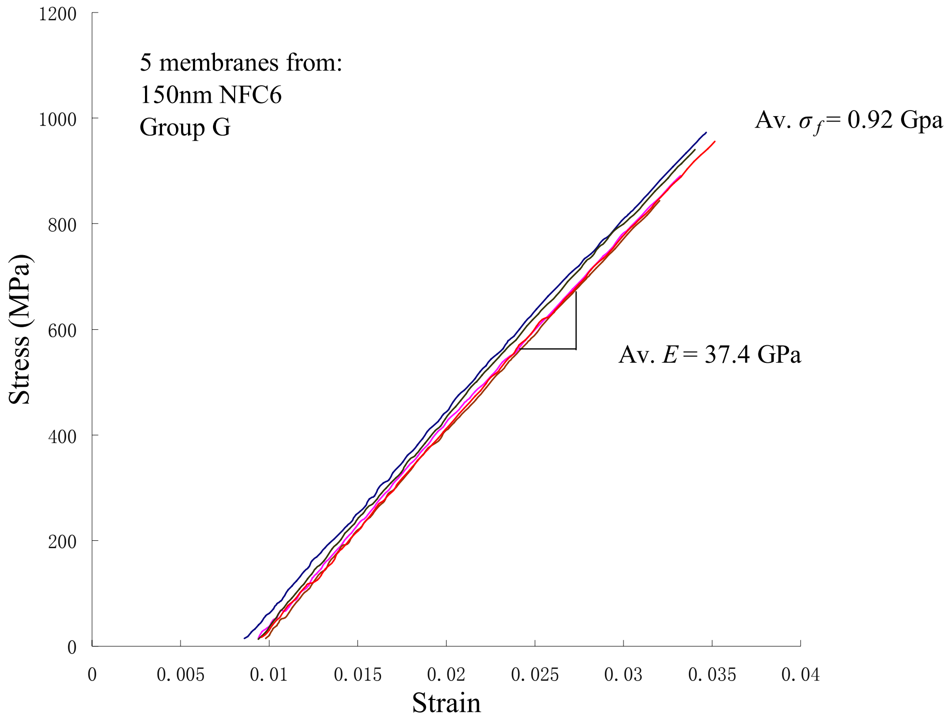

Figure 4.16a Stress-strain curves of 150nm NFC group G

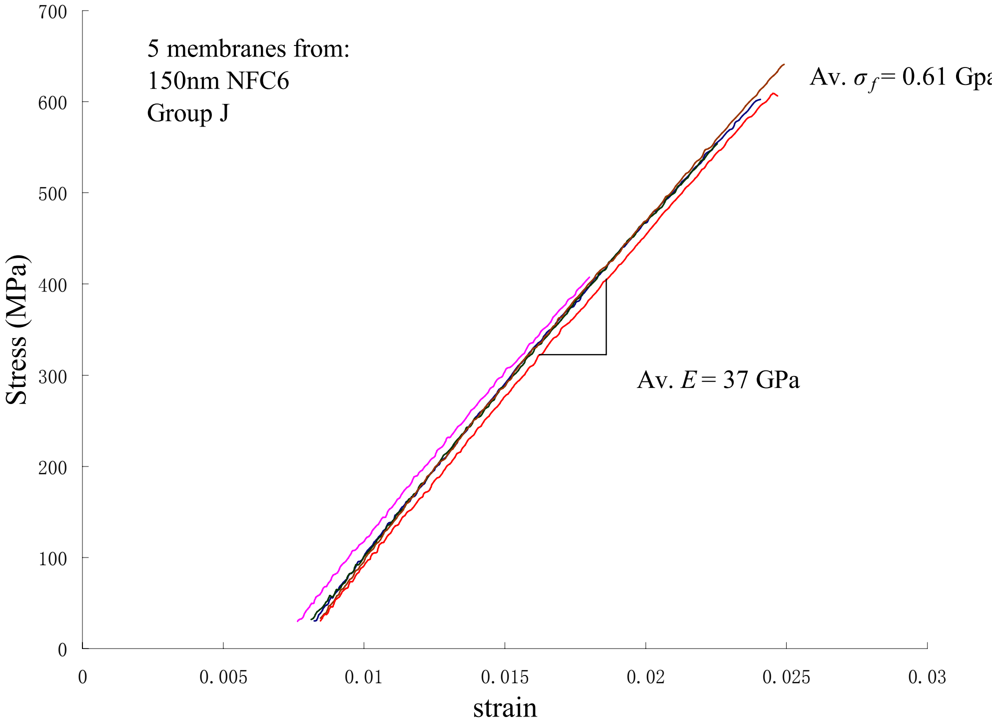

Figure 4.16b Stress-strain curves of 150nm NFC group J

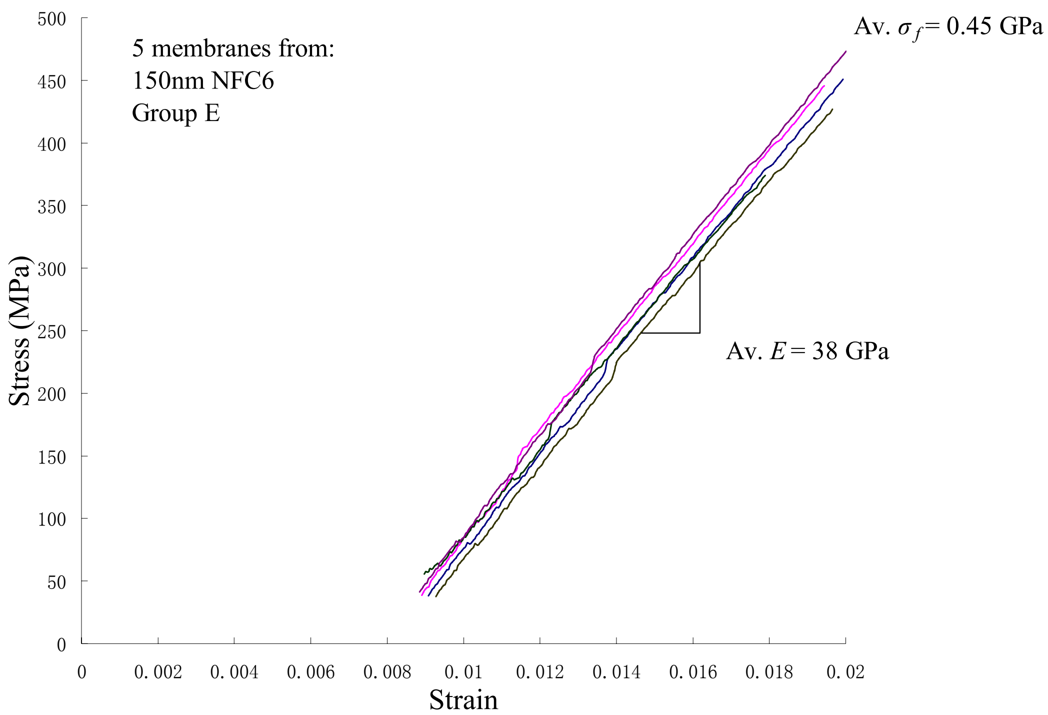

Figure 4.16c Stress-strain curves of 150nm NFC group E

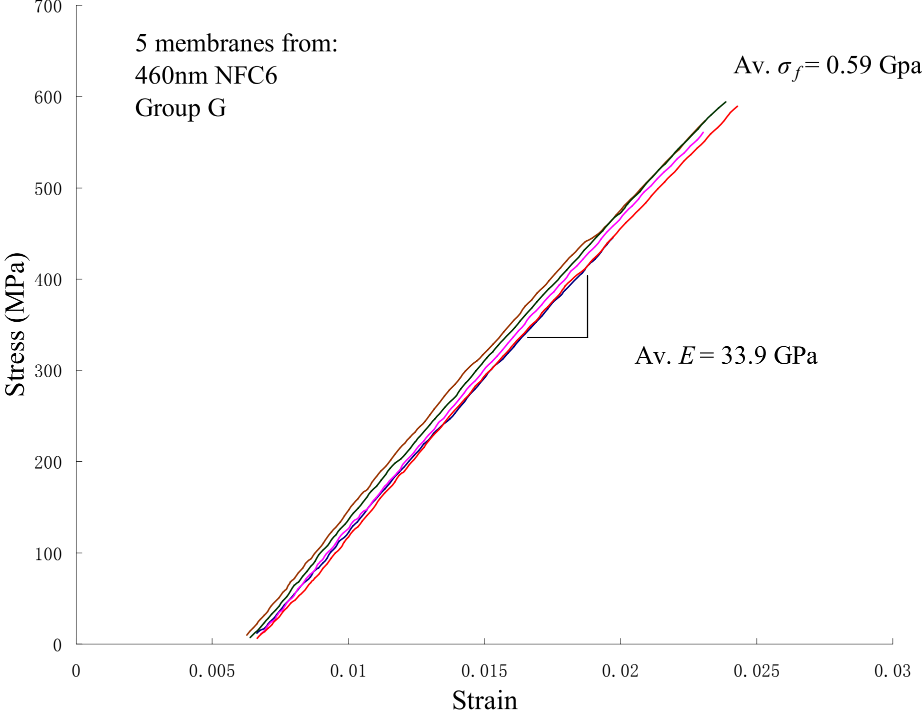

Figure 4.17a Stress-strain curves of 460nm NFC group G

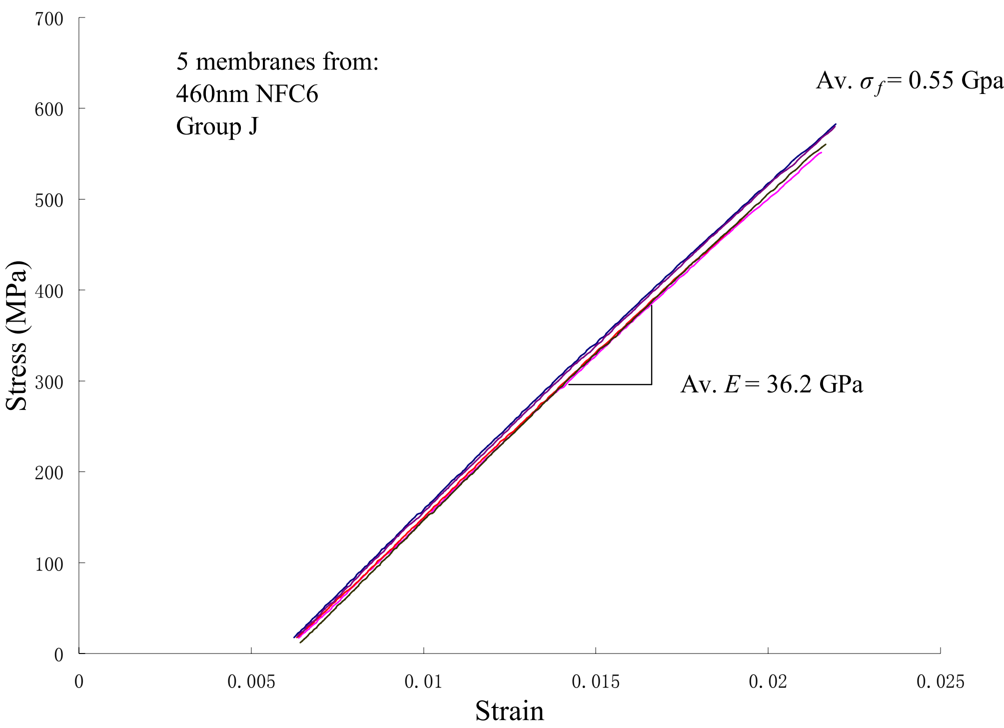

Figure 4.17b Stress-strain curves of 460nm NFC group J

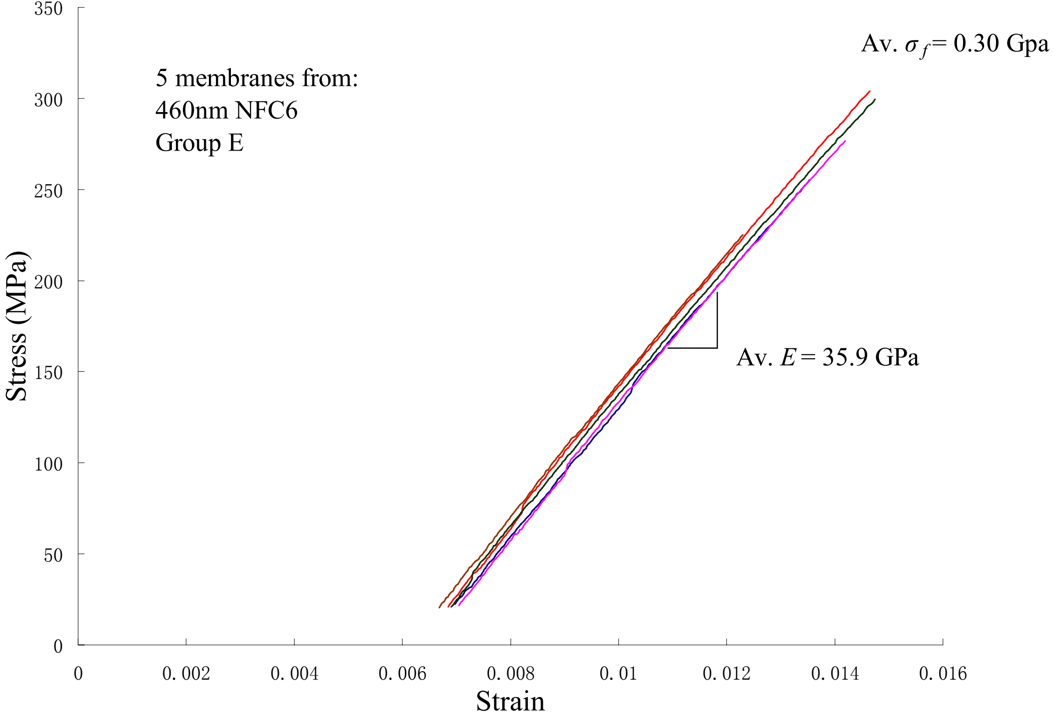

Figure 4.17c Stress-strain curves of 460nm NFC group E

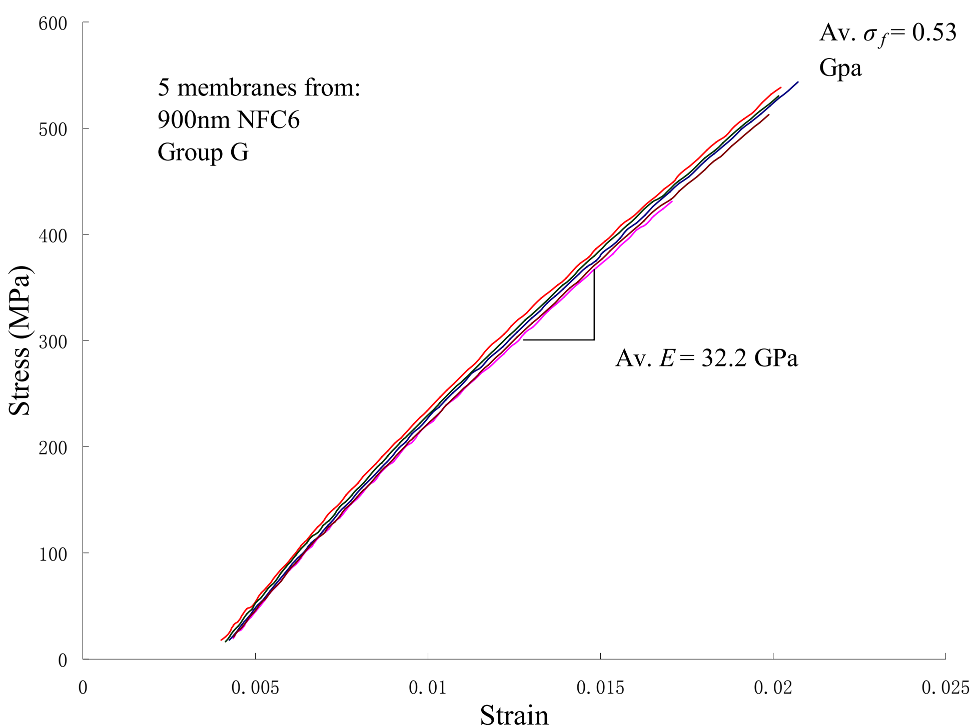

Figure 4.18a Stress-strain curves of 900nm NFC group G

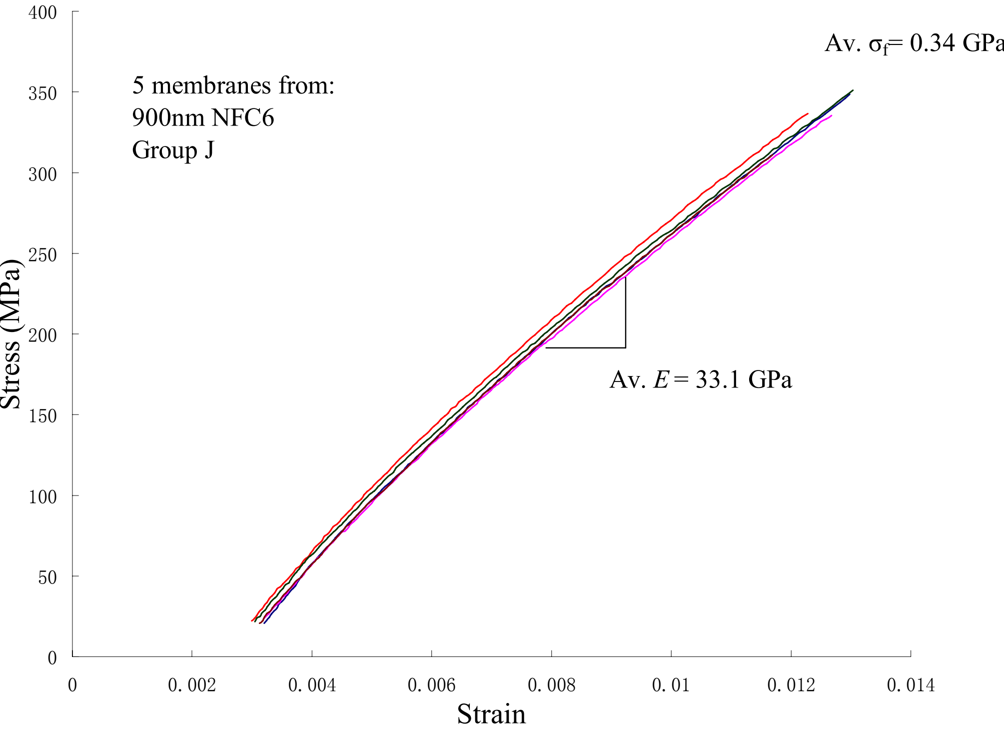

Figure 4.18b Stress-strain curves of 900nm NFC group J

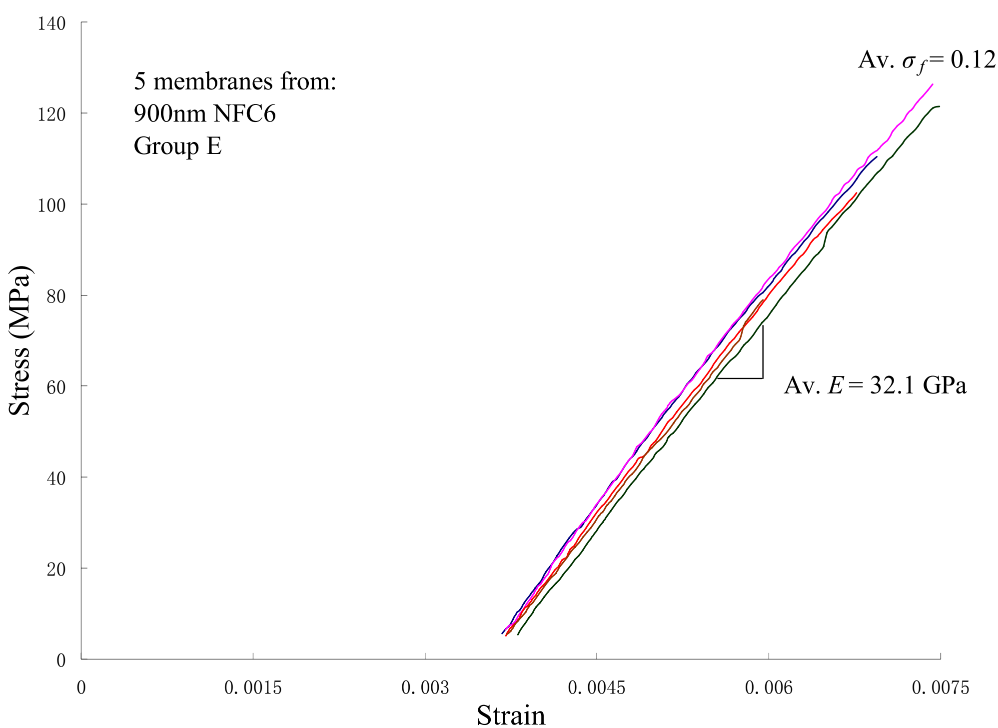

Figure 4.18c Stress-strain curves of 900nm NFC group E

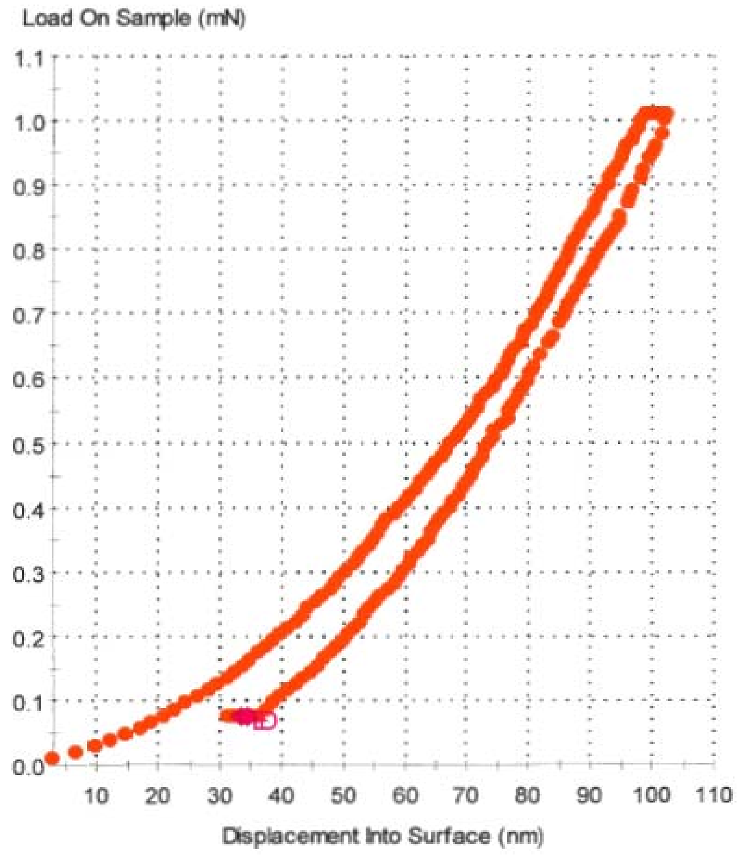

Figure 4.19 Nanoindentation Load-Displacement plot; static method on 900nm NFC

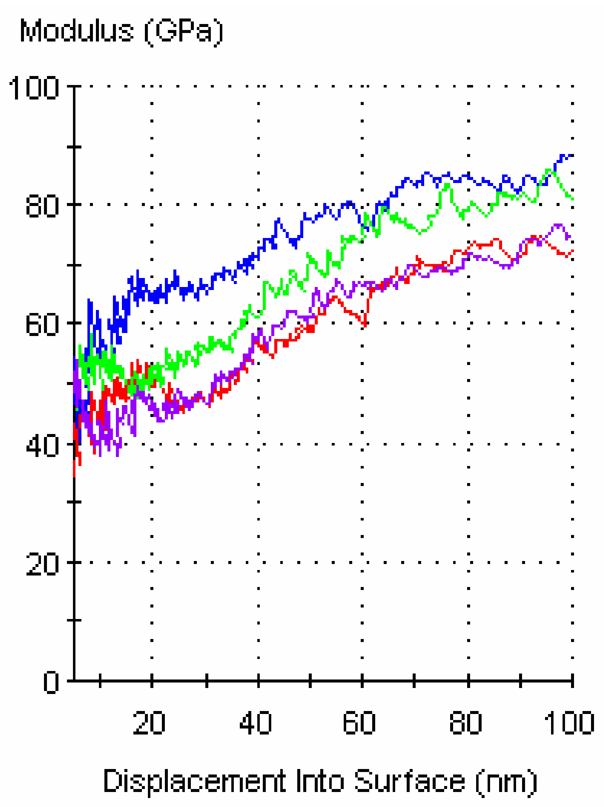

Figure 4.20 A group of CSM tests results run on the 150nm NFC surface. Each E-d curve represented an indent position that was randomly selected.

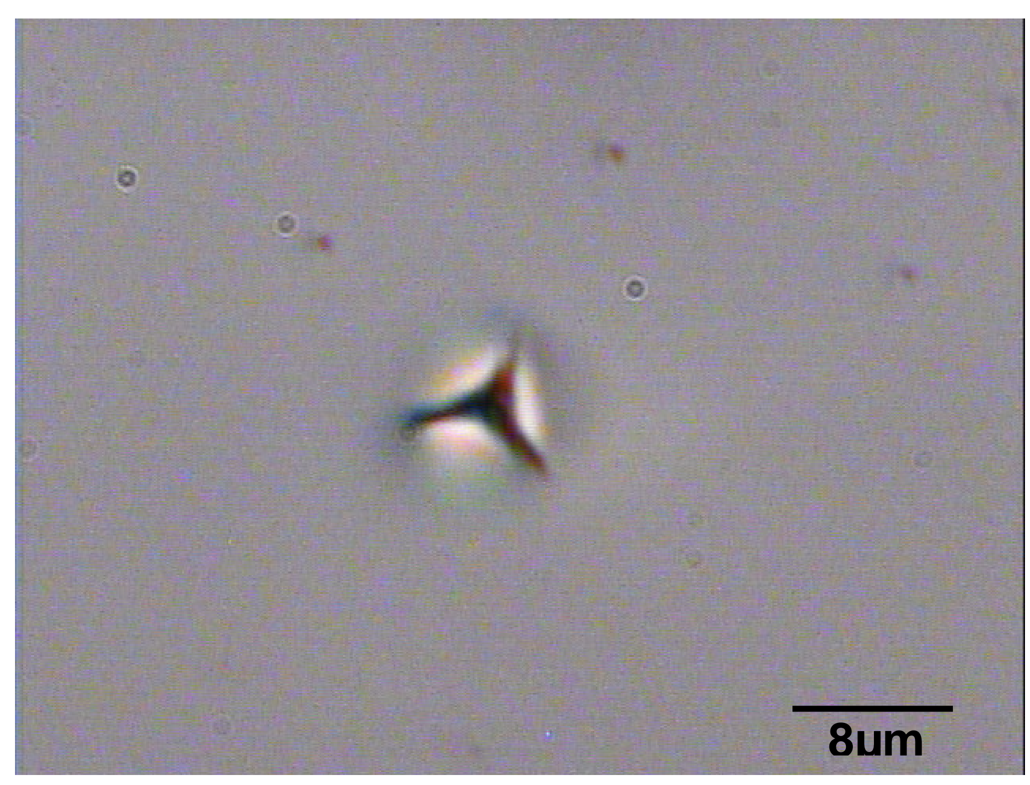

Figure 4.21 NFC film pile-up after nanoindentation test

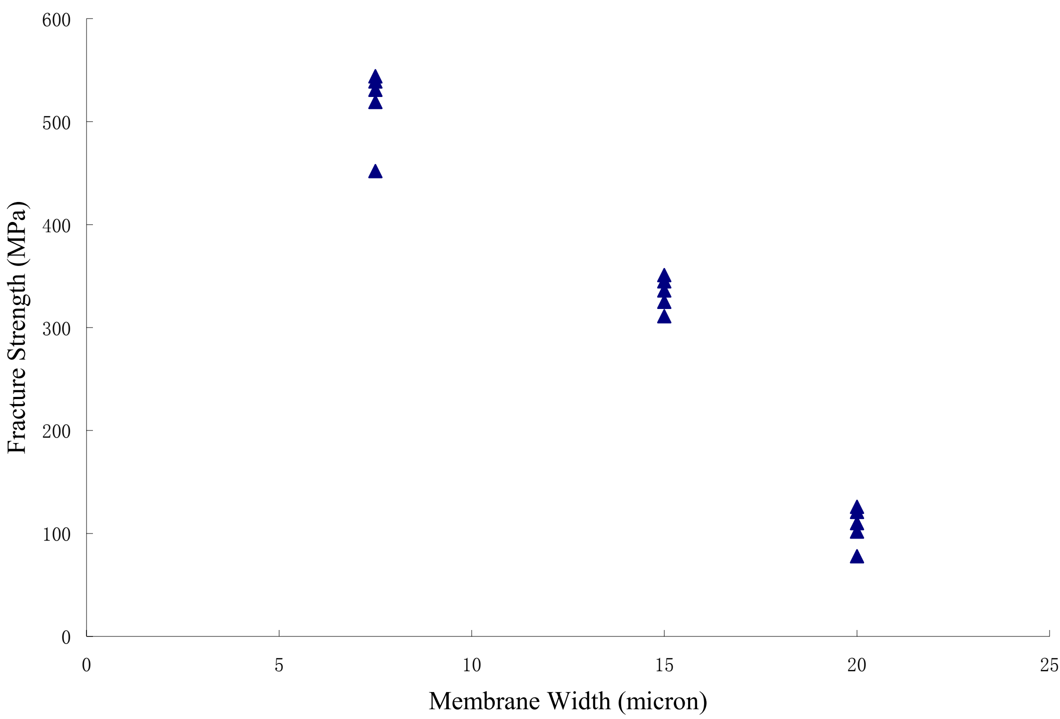

Figure 4.22 Width effect on fracture strength (900nm NFC)

Group G width: 7.5µm; Group J width: 15µm; Group E width: 20µm

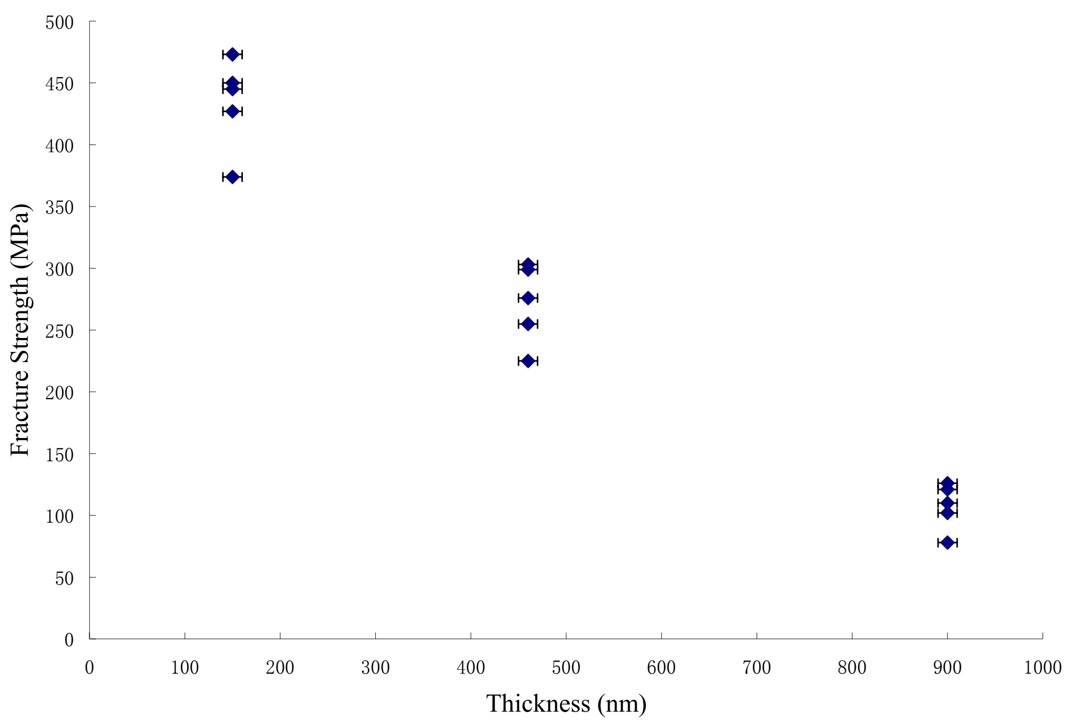

Figure 4.23 Thickness effect on fracture strength (group E)

NFC thicknesses: 150nm, 460nm, and 900nm

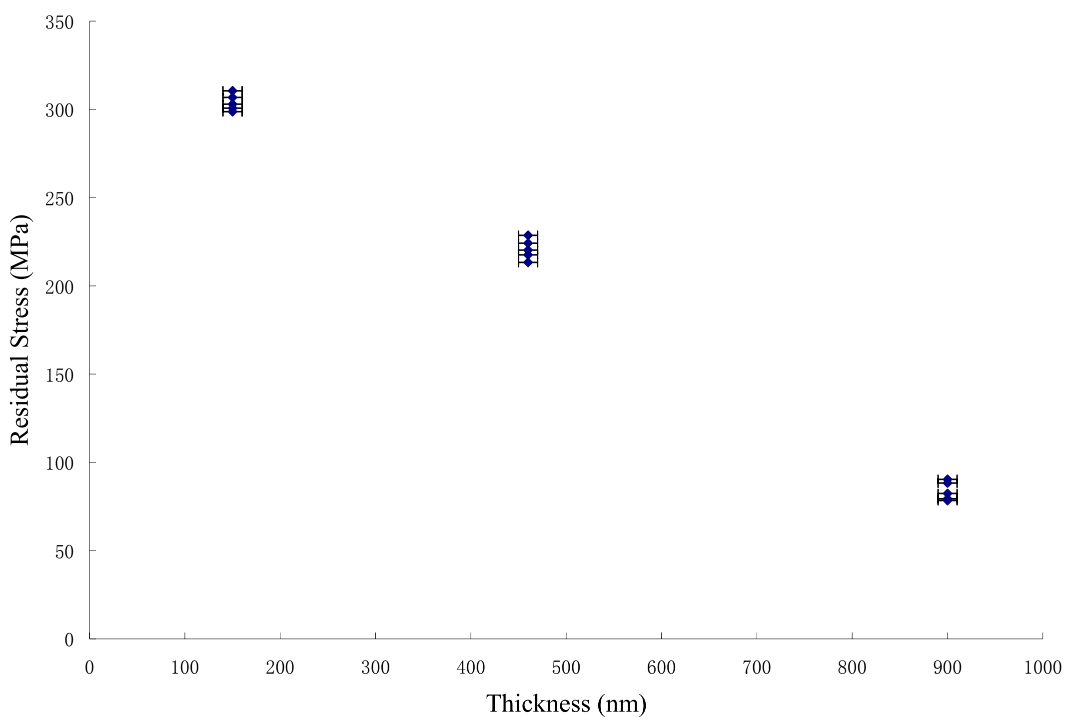

Figure 4.24 Thickness effect on residual stress (group E)

NFC thicknesses: 150nm, 460nm, and 900nm

CHAPTER 5

OVERALL CONCLUSIONS

In this thesis work, one of the near-frictionless hydrogenated amorphous carbon (a-C:H), NFC6 DLC thin films grown at Argonne National Lab was tested with membrane deflection experiment (MDE). This kind film has acceptable mechanical properties and excellent tribological properties, which is very suitable for MEMS as protective coatings. The NFC6 films were successfully fabricated and the mechanical properties of NFC films were obtained from a unique way (MDE) that no similar work has ever been done before in this field.

The NFC6 films were deposited at Argonne lab using the modified Perkin-Elmer 2400 RF PECVD. The source gases for deposition were 25% methane (CH_4) and 75% hydrogen (H_2). The self bias voltage applied was -375V~-425V. The process was running at Room Temperature. The deposition rate was 1.85nm/min. The NFC6 films with three thicknesses (150nm, 460nm, and 900nm) were deposited.

The NFC films were processed by the micromachining procedure to obtain the freestanding structure. The bottom side Si_3N_4 was first patterned and etched to obtain open windows. The top side was then patterned and chromium was sputtered on the surface as a mask layer for DLC etching. A lift-off process was used to give the shape of the membranes followed by DLC plasma etching. After silicon KOH etching and top Si_3N_4 plasma etching, the freestanding structure was obtained. The fabrication

parameters have been improved through the project, which are useful for future research work.

The freestanding NFC membranes were tested with the membrane deflection experiments (MDE) developed by Prorok and Espinosa to precisely measure the mechanical properties of freestanding thin films. In this method, free standing NFC membranes were fabricated and stretched by a nanoindenter while deflection was monitored with an interferometer. Combining these two independent measurements, the NFC6 film mechanical properties like Young's modulus, fracture strength, and residual stress were characterized. Moreover, this method effectively eliminated the substrate effect of the nanoindentation test due to the freestanding structure.

The NFC6 films were characterized with Raman spectroscopy, SEM, and AFM, etc. From the Raman spectra, the D peak and G peak were found at 1366 cm^{-1} and 1594 cm^{-1}. The G peak position and I_D/I_G ratio indicated that the film has a 30~40% sp3 content. SEM helped determine the shape of the freestanding membranes. Due to the different coefficient of thermal expansion (CTE) between Si_3N_4 and NFC, the DLC membranes would bend down in some content during the topside Si_3N_4 etching. Each testing membrane was characterized with SEM before MDE tests to avoid any unnecessary faults. AFM was applied to measure the topography of the NFC films. The RMS roughness ranged from 5.36 nm to 7.86 nm. The film looked uniform and smooth from the AFM images.

During the MDE tests, the interferometer images of the bending membranes were taken to show the original fringes. The image pixel length obtained from SEM figures

helped determine the exact distances between two adjacent dark fringes. Those distances were used to calculate the original length of the membrane. The profile could determine the touching point of the MDE tests as well as the starting point of the stress-strain curve where pure tension was applied. Four air tests were done before the real MDE in order to obtain a stable and accurate air effect baseline. Based on our methods, the bending membrane had a positive strain as the nanoindenter tip touched the membrane. The final stress strain curve intersected Y axis with a negative value, which indicated a tensile residual stress.

The Young's modulus of NFC films was determined as 32~38 GPa. The average (arithmetic mean) value was 35.13 GPa. The standard deviation was 2.292 GPa. Totally, 45 membranes were counted to obtain an average value of the elastic modulus. All the NFC films were also tested with the static and CSM nanoindentation methods. The Poisson's ratio was assumed as 0.3. The Young's modulus obtained from static method was 48~53 GPa and was 56~79 GPa from CSM method. Substrate effect could be observed. The NFC films also had pile-up phenomenon during nanoindentation tests. This would enlarge the contact area and cause the real modulus smaller than the theoretical values. The NFC Young's modulus obtained from MDE tests was comparable to those from other authors.

The fracture strength ranges from 0.12 GPa to 0.90 GPa. From the MDE data, it was found the fracture stress to increase with decreasing membrane width (W). The NFC6 film was amorphous, in which the flaws existed in the film dominated the fracture strength. A wider membrane might have more flaws in it, which raises the

probability to be broken. In other words, more flaws lower the fracture strength.

Thickness effects were observed on both fracture strength and residual stress. The mechanism for fracture strength was same to the width effect. The residual stresses were found comparable for each wafer (same thickness). But they were affected by the thickness change. Since the stiffness was proportional to the cube of thickness (d^3), a thicker film was more difficult to bend, which brought a lower residual stress. The residual stress ranged from 79 MPa to 310 MPa through the 45 testing membranes.

BIBLIOGRAPHY

[1] J.B. Pethica, R. Hutchings, W.C. Oliver, Philos. Mag. A 48 (1983) 593

[2] G. Pharr, W.C. Oliver Mater. Res. Soc. Bull. 17 (1992) 28

[3] X. Jiang, J. W. Zou, K. Reichelt, P. Grunberg, J. Appl. Phys. 66 (1989) 4729

[4] X. Jiang, K. Reichelt, B. Stritzker, J. Appl. Phys. 66 (1990)5805

[5] E.H.A. Dekempeneer, R. Jacobs, J. Smeets, J. Meneve, L. Eersels, B. Blanplaiin, J. Roos, D.J. Oostra, Thin Soild Films 217 (1992) 56

[6] G.M. Pharr, D.L. Callahan, J. Robertson, et al., Appl. Phys. Lett. 68 (1996) 779

[7] H.D. Espinosa, B.C. Prorok, M. Fischer, J. Mech. and Phys. of Solids 51 (2003) 47-67

[8] B.C. Prorok, Micro- and Nanomechanics, Encyclopedia Nanonsci. & Nanotech. V5 Pg 555-600

[9] W. Jacob, W. Moller, Appl. Phys. Lett. 63 (1993) 1771

[10] A. Erdemir, O.L. Eryilmaz, et al, Diamond and Related Materials 9 (2000) 632-637

[11] J. Robertson, DLC reports, Materials Science and Engineering R 37 (2002) 129-281

[12] J.C. Angus, C.C. Hayman, Science 241 (1998) 913

[13] D.R. McJenzie, Rep. Prog. Phys. 59 (1996) 1611

[14] M. Weiler, S. Sattel, K. Jung, et al. Appl. Phys. Lett. 64 (1994) 2797

[15] J. Robertson, Prog. Solid State Chem. 21 (1991) 199

[16] N. Savvides, J. Appl. Phys. 59 (1989) 4133

[17] J. S.chwan, S.ulrich, H. Roth, et al, J. Appl. Phys. 79 (1996) 1416

[18] Koidl, C. Wagner, et al. Materi. Sci. Forum 52 (1990) 41

[19] N.M.J Conway, AC. Ferrari, et al. Diamond Rel. Mater. 9 (2000) 765

[20] M.A. Lieberman and A. J. Lichetenberg, Principle of Plasma Dscharge and Materials Processes. New York: john Wiley & sons, Inc. 1994

[21] E. G. Spencer, et al. Appl. Phys. Lett. 29 (1976) 118

[22] Y. Liftshitz, et al. Phys. Rev. B 41 (1990) 10468

[23] W. Moller, Appl. Phys. Lett. 59 (1991) 2391

[24] D.R. McKenzie, J. Vac. Sci. Technol. B 11 (1993) 1928

[25] J. Robertson, Pure Appl. Chem. 66 (1994) 1789

[26] J. Robertson, Diamond Rel. Mater. 3 (1994) 361

[27] J. Robertson, Radiat. Effect 142 (1997) 63

[28] H.P. kaukonen, R.M. Nieminen, Phys. Rev. B 61 (2000) 2806

[29] S. Uhlmann, T. Frauenheim, et al, Phys. Rev. Lett. 81 (1998) 641

[30] C.A. Davis, Thin Solid Films 226 (1993) 30

[31] J. Robertson, Diamond Rel. Mater. 2 (1993) 984

[32] I. Koponen, M. Hakovirta, and R. Lapplalinen, J. Appl. Phys, vol. 78, pp. 5837-5839, 1995

[33] J.F. Ziegler, J.P. Biersack, et al. The stopping and range of ions in solides, pergamon press, oxford, 1985

[34] W. Jacob*, Thin Solid Films 326 (1998) 1-42

[35]A. von Keudell, T. Schwarz-Sellinger, W. Jacob, J. Vac. Sci. Technol. A 19 (2001) 101

[36] M.A. Tamor, et al, App. Phys. Lett. 58 (1991) 592

[37] A. Von Keudell, W. Jacob, J. Appl. Phys. 79 (1996) 1092

[38] W.M.M Kessel, et al. Surf. Coatings Technol. 98 (1998) 1584

[39] Tai-Ran Hsu, MEMS and Microsystems: Design and Manufacture, McGraw-Hill, ISBN: 0072393912, 2002

[40] Richard C. Jaeger, "Introduction to microelectronic fabrication", Prentice Hall, 2nd edition, 2002

[41] D.B. Tuckerman and R.F.W. Pease, "high performance heat sinking for VLSI" , IEEE electron device letters, Bol. EDL-2, no. %, pp. 126-129, May 1981.

[42] Sungwoo Cho, et al, J. Micromech. Microeng. 15 (2005) 728-735

[43] Te-Hua Fang, et al, Thin solid films 396 (2001) 166-172

[44] X.T. Zhou, et al, Surf. Coat. Tech. 123 (2000) 273-277

[45] N. Mehta, Master's thesis, Materials Engineering, Auburn, Spring 2005

[46] J.L. Hay, Instrumented indentation testing, MTS Systems Corporation, 2001

[47] W.C. Oliver and G.M. Pharr, J. Mater. Res. Vol. 7 (No.6), 1992, p 1564-1583

[48] MTS, CSM review paper, MTS system Corporation, 2001

[49] Standard Test for Microhardness of materials, ASTM standard test method E 384, Annual book of standards 3.01, American society for testing and materials, 1989, p469

[50] H.D. Espinosa, B.C. Prorok, et al, Experimental Mechanics, Vol. 43, No. 3, 256-

268 (2003)

[51] P.Y Yu, et al, Fundamentals of Semiconductors, Springer, Berlin, 1996

[52] S.R. Salis, et al, Diamond Rel. Mater. 5 (1996) 589

[53] R.E. Schroder, et al, Phys. Rev. B 41 (1990) 3738

[54] A.C. Ferrari, et al, Phys. Rev. B 61 (2000) 14095

[55] M.A. Tamor, W.C. Vassel, J. Appl. Phys 76 (1994) 3823

[56] N. Mehta, et al, M.R.S., Materials Research Society Symposium Proceedings, vol.843, pp. T2.7.1-T2.7.6, 2005

[57] Che-Heung Kim, et al, J. Micromech. Microeng. 15 (2005) 358-361

[58] Sung-jin Cho, et al, Diamond Rel. Matter. 14 (2005) 1270-1276